dortmund university

Dissertation

submitted for the academic degree
Doctor rerum naturalium (Dr. rer. nat.)

The electronic and magnetic properties of α-MnTe, an antiferromagnetic semiconductor

by
Kira Deltenre

2024

Department of Physics
TU Dortmund University

Dissertation
Department of Physics
TU Dortmund University
Dortmund, Germany

First Reviewer:	Prof. Dr. Frithjof B. Anders
Second Reviewer:	Prof. Dr. Götz S. Uhrig

Zusammenfassung

Die elektronischen und magnetischen Freiheitsgrad von α-MnTe, einem antiferromagnetischen Halbleiter, wurden betrachtet, um die Kopplung zwischen den elektronischen und magnetischen Eigenschaften zu untersuchen.

Magnonische Anregungen im magnetischen System wurden mithilfe eines Heisenbergmodells berechnet. Verwendet wurde die lineare Spinwellentheorie und die Holstein-Primakoff-Darstellung. Die zugrunde liegende Annahme ist, dass Laserpulse eine zeitliche Änderung der Heisenbergkopplungsparameter bewirken, sodass Magnonen angeregt werden. Der Einfluss der Stärke, der Frequenz und der Dauer des treibenden Terms wurden untersucht. Relaxation wurde durch einen phänomenologischen Zerfallsterm modelliert. Indem realistische Parameter verwendet wurden, konnte das Modell auf das Experiment angewendet werden.

Die elektronische Bandstruktur und Zustandsdichte wurden mit einem Tight-Binding-Modell untersucht. Die entsprechenden Hüpfparameter wurden mit der Dichtefunktionaltheorie bestimmt. Eine Aufspaltung der Mn $3d$-Bänder durch Korrelationen führt zu einer Bandlücke. Mithilfe von Projektionen auf die ursprünglichen Orbitale wird deutlich, dass das Valenzband Te $5p$-Charakter hat, während das Leitungsband Mn $3d$- und Mn $4s$-Anteile aufweist.

Ein Ein-Band-Kondo-Hubbard-Modell des Mn $3d$-Systems kombiniert die elektronischen und magnetischen Freiheitsgrade. Gelöst wurde es mit der Dynamical Mean Field-Theorie und der Numerischen Renormierungsgruppenmethode. Gemessen wurde die Mottlücke in der paramagntischen und magnetisch geordnetetn Phase, um die Blauverschiebung der Lücke zu quantifizieren, welche durch die schmaler werdenden Bänder entsteht. Indem die berechnete Selbstenergie in das Multiorbital-Tight-Binding-Modell miteinbezogen wird, wird die Halbleiter-Bandlücke berechnet. Im Gegensatz zum Experiment wird die Bandlücke in der vorliegenden Modellierung kleiner für tiefere Temperaturen. Eine mögliche Erklärung wird diskutiert.

Die Charakterisierung von elektronischen und magnetischen Eigenschaften von α-MnTe sowie die vorgeschlagenen Modelle können ein Ausgangspunkt für weitere Analysen des Materials darstellen. Des Weiteren können die vorgestellten Methoden auf andere antiferromagnetische Halbleitersysteme angewendet werden.

Abstract

We calculated the electronic and magnetic degrees of freedom of α-MnTe, an antiferromagnetic semiconductor, to investigate the coupling between the electronic and magnetic properties.

To calculate magnonic excitations, we described the magnetic system as a Heisenberg model and solved it within the linear spin wave theory with the Holstein-Primakoff representation. We assumed that laser pulses change Heisenberg couplings in time, which induces magnons. We determined the effect of the driving strength, frequency, and duration. To capture relaxation, we included a phenomenological decay. We applied our model to experiments by using realistic parameters.

We studied the electronic properties by calculating the band structure and the density of states with a tight-binding model. To determine the hopping parameters, we used the density functional theory. By introducing a splitting between the Mn $3d$ bands induced by correlations, we obtained a band gap. The projections to the atomic orbitals revealed that the valence band is formed by Te $5p$ bands while the conduction band consists of Mn $3d$ and Mn $4s$ contributions.

To combine electronic and magnetic degrees of freedom, we calculated the Green's function and the spin expection values for a one-band Kondo-Hubbard model describing the Mn $3d$ electrons with the dynamical mean field theory and the numerical renormalization group method. We measured the Mott gap in the paramagnetic and antiferromagnetic phase to quantify the magnetic blue shift. The narrowing of the bands causes mainly the increase of the Mott gap. By including the resulting self-energy into a multi-orbital tight-binding model, we calculated the semiconductor band gap. The band gap becomes smaller for lower temperatures in our modeling in contrast to the experimental finding, with the possible explaination discussed.

The concrete characterization of electronic and magnetic properties of α-MnTe and the proposed models might be a starting point for further analyses of the material. The presented methods can be also applied to other antiferromagnetic semiconductor systems.

List of publications

Major parts of Chap. 2 of this thesis reuse or are adapted from the author's contributions to the following publications:

- K. Deltenre, D. Bossini, F. B. Anders, and G. S. Uhrig
  Lattice-driven femtosecond magnon dynamics in $\alpha-MnTe$
  Phys. Rev. B **104**, 184419 (2021)
- D. Bossini, S. Dal Conte, M. Terschanski, G. Springholz, A. Bonanni, K. Deltenre, F. Anders, G. S. Uhrig, G. Cerullo, and M. Cinchetti
  Femtosecond phononic coupling to both spins and charges in a room-temperature antiferromagnetic semiconductor
  Phys. Rev. B **104**, 224424 (2021)

In addition, the following article was published, which will not be discussed in this thesis:

- F. Vonhoff, A. Fischer, K. Deltenre, and F. B. Anders
  Microscopic origin of the effective spin-spin interaction in a semiconductor quantum dot ensemble
  Phys. Rev. Lett. **129**, 167701 (2022)

Contents

1 Introduction **1**
- 1.1 Experimental findings . . . 2
  - 1.1.1 Phononic coupling to spins and charges . . . 2
  - 1.1.2 Magnetic blue shift of the band gap . . . 3
- 1.2 Research objective . . . 4
- 1.3 Properties of hexagonal manganese telluride . . . 5

2 Lattice-driven magnon dynamics **7**
- 2.1 Model . . . 7
- 2.2 Methods . . . 8
- 2.3 Equilibrium properties . . . 10
- 2.4 Dynamics out of equilibrium . . . 12
  - 2.4.1 Magnon dynamics of a single mode . . . 13
  - 2.4.2 Dynamics of the sublattice magnetization . . . 23
  - 2.4.3 Making contact to experiments . . . 33
- 2.5 Summary . . . 37

3 Electronic structure of α-MnTe **39**
- 3.1 Tight-binding Hamiltonian . . . 40
  - 3.1.1 Multi-orbital tight-binding Hamiltonian . . . 40
  - 3.1.2 Calculating the band structure . . . 43
  - 3.1.3 Calculating the density of states . . . 43
- 3.2 Density functional theory . . . 44
  - 3.2.1 Wannier functions . . . 47
  - 3.2.2 Hopping between different types of orbitals . . . 48
  - 3.2.3 Dispersion and density of states . . . 50
- 3.3 Summary . . . 55

4 The magnetic shift of the band gap **57**
- 4.1 Dynamical mean-field theory . . . 57
  - 4.1.1 The DMFT loop . . . 59
  - 4.1.2 Hubbard-Kondo lattice model . . . 60
  - 4.1.3 DMFT on a bipartite lattice . . . 61
  - 4.1.4 Dealing with five $3d$ bands . . . 63

4.2 Numerical renormalization group method 63
4.2.1 Logarithmic discretization 65
4.2.2 Mapping on a semi-infinite chain 67
4.2.3 Iterative diagonalization 69
4.2.4 Calculation of physical properties 71
4.2.5 Broadening of discrete spectra 74
4.2.6 Choice of parameters 74
4.3 Numerical results 75
4.3.1 Effective description with a Gaussian density of states . . . 76
4.3.2 Comparison to a Heisenberg model 78
4.3.3 Measuring the band gap via the spectral functions 81
4.3.4 Renormalized band structure 88
4.4 Summary 100

5 Conclusion **103**

Bibliography **107**

Chapter 1

Introduction

The interaction between light and matter is one of the key research fields in solid state physics today. Experiments using light offer a deeper understanding of properties of materials, and light may also be used to control the material properties. Especially, laser pulses manipulating the magnetic order of a system [1–6] would be a major part of building spintronic devices, which are electronic devices making use of the electron's spin in addition to its charge [7].

Spintronics is a research field which focuses on three main questions concerning the electron spin in systems [8]: First, how can a system be polarized effectively? Second, how long does the system remain in this state? And third, what kind of detection can be used to measure the polarization?

The potential applications of spintronics are vast. To classify them, a distintion in the Mott type, which focuses on the electron and the hole spin, and the Dirac type, which deals with spin and orbit moments, is made [9]. Both types evolved in the last decades and can be divided into different generations: the first generation uses spin transport; the second generation focuses on spin–orbit effects, electric field, and electro-magnetic waves to induce spin dynamics, and the third generation explores three-dimensional structures and quantum engineering, including quantum computing [9]. An example of different stages of development can be found in data storage devices. While hard disk drives (HDD) belong to the first generation and are already widely used, the magnetoresistive random-access memory (MRAM) technology [10], which is also based on magnetizing a ferromagnetic material but with using magnetic tunnel junctions, is part of the second generation [9]. Spin diodes and spin transistors are examples of the third generation of Dirac type spintronic devices [9].

Spintronic devices could be more efficient concerning energy consumption [11] since the energy needed to control spins can be smaller than the energy needed to control the charge. Energy efficiency becomes more and more important since the need of data processing and storage grows rapidly and some applications, such as video

streaming, cannot be regulated easily, while work could be done to reduce the energy consumption of data centers [12].

Before building spintronic devices, the properties of potential materials and the possibilities to control them have to be investigated. Ultrafast optical switching of the magnetization in many different materials has been already demonstrated [1, 3], as well as magnetic phase transitions on the femtosecond time scale [13–15]. The light-induced coherent generation of magnons was also realized in experiments [2, 16–18].

One potential candidate for spintronic devices is hexagonal manganese telluride (α-MnTe). The material has strong correlations yielding the nonlinear phononics [19, 20] and the Kittel mode [21] induced by phonon-magnon coupling. The lifetime and the frequency of the Raman-active phonon modes change if the material is magnetically ordered [22]. The material contains a magnetic and an electronic subsystem: the Mn $3d$ electrons align to a spin of $5/2$ at the Mn sites, while the Te $5p$ and Mn $3d$,$4s, p$ orbitals form bands with a band gap, the typical property of a semiconductor.

1.1 Experimental findings

The key questions is how the charge subsystem and spin subsystem couple. Two experiments were performed to address this question. The phononic coupling to spins and charges was investigated [23], and the magnetic blue shift of the band gap was measured [24]. As a basis for our work, we will briefly summarize both experiments.

1.1.1 Phononic coupling to spins and charges

Bossini et al. [23] investigated α-MnTe via pump-probe experiments. The general idea of pump-probe experiments is to apply a first laser pulse, which excites the system and pushes it out of equilibrium, and a second one, which probes the system. By performing the measurement with different temporal distances between the pulses, the time development of the considered value is accessible.

In a first step, the transient reflectivity of α-MnTe was measured at a temperature of $T = 77\,\mathrm{K}$. The linearly polarized pump pulse had $2.4\,\mathrm{eV}$ energy, while the linearly polarized continuum probe pulse covered energies in the spectral range $(1.65 - 2.76)\,\mathrm{eV}$. The measurement allows to detect the photodriven transient evolution of E_g. While the reflectivity is positive well below $1.71\,\mathrm{eV}$, it is negative

well above this energy. For energies near to 1.71 eV, the sign changes with time. The oscillations have a frequency of $\omega_0 = 5.3\,\mathrm{THz}$.

In a second step, the energy of the probe pulse was fixed to 1.72 eV, and the transient transmissivity was measured. The probe pulse is transmitted through the sample and changes in general the direction of its polarization. This angle is measured by splitting the orthogonal parts via a Wollaston prism and performing a balanced detection. The setup is shown schematically in Fig. 1.1.

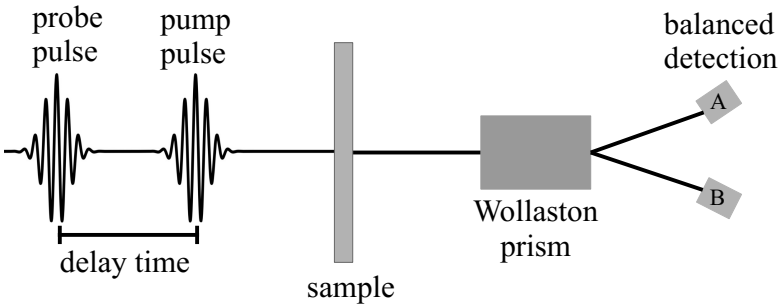

Figure 1.1: The scematic setup of a pump-probe experiments measuring the transmitted light with balanced detection.

It turns out that the applied laser pulse excites optical phonons in α-MnTe. Due to these coherent lattice vibrations, the Mn and Te ions oscillate with a phase shift to each other. This oscillation leads to a periodical change of the distances between these ions.

The measured angle oscillates with the frequency ω_0, which can be identified as the frequency of phonons excited by the laser pulses. In addition, the decreasing amplitude can be fitted by a combination of exponential decays. The inverse decay rates describe the lifetime of the excitations.

1.1.2 Magnetic blue shift of the band gap

In another experiment, Bossini et al. [24] determined the band gap E_g of α-MnTe for the temperature range 25 K to 400 K by analyzing the phonon assisted absorption and emission. The band gap is temperature dependent and smaller for higher temperatures. Its absolute value is $E_g = (1.27 - 1.46)\,\mathrm{eV}$ [24].

The leading order contribution of the temperature dependency of E_g is captured by the Varshni function [25]. The Varshni functions includes electron-phonon coupling and fits well the temperature dependence of E_g above the Néel temperature. Below T_N, thus in the magnetically ordered phase, there are significant deviations from this fit. Here the band gap is larger than expected. This effect is called magnetic blue shift of the band gap. Since the effect sets in at the Néel temperature, the shift is a hint that there is an additional magnetic contribution.

Reference [24] shows that this is a mean-field effect, and Refs. [26, 27] confirm this finding with real-space dynamical mean-field theory (DMFT) calculations with exact diagonalization (ED) as impurity solver.

1.2 Research objective

The question is how the magnetic and the electronic degrees of freedom in α-MnTe couple. To approach this problem, we analyze the magnetic excitations, the band structure, and the band gap in calculations including magnetic and electronic properties.

We focus on the magnetic excitations in Chap. 2. We model the interactions between the spins of Mn $3d$ orbitals with a Heisenberg Hamiltonian. Assuming that the laser pulses indirectly induce a change in the Heisenberg coupling via the displacements of the ions, we investigate the resulting magnon excitations with linear spin wave theory. We use the Holstein-Primakoff representation and the Bogoliubov transformation to treat the problem. We solve the set of differential equations numerically to calculate the non-equilibrium magnon dynamics.

We concentrate on the single-particle electronic properties of α-MnTe in Chap. 3. We calculate its band structure and density of states by using tight-binding Hamiltonians. To obtain hopping parameters, we use the density functional theory.

In Chap. 4, we combine magnetic and electronic degrees of freedom in an effective one-band Kondo-Hubbard model for the Mn $3d$ electrons. We adapt the approach of Ref. [26, 27] to consider a dynamical mean field theory approach in reciprocal space and to solve the impurity problem with the numerical renormalization group method. We calculate the magnetic blue shift of the Mott gap. Furthermore, we included the resulting self-energy into a multi-orbital tight-binding model to determine the semiconductor band gap.

Finally, we discuss the different approaches and summarize how our research contributes to the key question in Chap. 5. We also point out how our approach could be extended in future research.

1.3 Properties of hexagonal manganese telluride

Since we will need the basic properties of α-MnTe in different parts of this thesis, we will summarize them in this section.

Hexagonal MnTe has an NiAs crystal structure [28] as depicted in Fig. 1.2. The Mn ions are arranged in triangular layers with lattice constant a, which are stacked on each other with a distance of half of the lattice constant c. Several measurements to obtain the lattice constants were performed leading to similar results [29]. We will use $a = 4.1497\,\text{Å}$ and $c = 6.76\,\text{Å}$ [30, 31] in the following chapters.

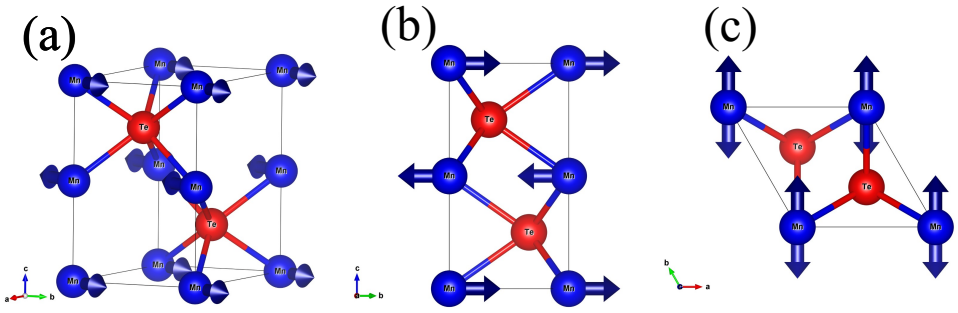

Figure 1.2: Scetch of the unitcell. While panel (a) displays the whole structure, panel (b) focuses on the antiparallel alignment of the spins of neighboring Mn layers, and panel (c) shows the triangular lattice structure of the Mn layers. Made with VESTA [32].

The material is an antiferromagnetic semiconductor with a band gap of $E_g = (1.27 - 1.46)\,\text{eV}$ [24]. The antiferromagnetic order is realized below the Néel temperature of $T_\text{N} \approx 310\,\text{K}$ [33].

The electrons in the $3d$ Mn orbitals form a total spin of $5/2$ following the Hund's rule. Within the Mn layers, these total spins are oriented parallelly. The spins of different but neighboring layers are antiparallelly aligned. Experimental measurements have shown that the spins point in the Mn layer plane [34, 35].

When we want to describe the magnetic phase, we need a unit cell with four atoms: two Te atoms and two Mn atoms with magnetic moments pointing in opposite directions. The lattice vectors are:

$$\vec{a} = a \begin{pmatrix} 1/2 \\ \sqrt{3}/2 \\ 0 \end{pmatrix}, \vec{b} = a \begin{pmatrix} 1/2 \\ -\sqrt{3}/2 \\ 0 \end{pmatrix}, \vec{c} = c \begin{pmatrix} 0 \\ 0 \\ 1 \end{pmatrix}. \tag{1.1}$$

The atoms are located at

$$\vec{r}_{\mathrm{Mn},1} = \vec{0}, \quad \vec{r}_{\mathrm{Mn},2} = \frac{1}{2}\vec{c}, \quad \vec{r}_{\mathrm{Te},1} = \frac{1}{3}\vec{a} + \frac{2}{3}\vec{b} + \frac{1}{4}\vec{c}, \quad \vec{r}_{\mathrm{Te},2} = \frac{2}{3}\vec{a} + \frac{1}{3}\vec{b} + \frac{3}{4}\vec{c}. \quad (1.2)$$

Since we aim descriptions in $\vec{k}$ space in the following chapters, we determine also the reciprocal vectors defining the Brillouin zone:

$$\vec{k}_x = \frac{4\pi}{a}\begin{pmatrix} 1 \\ -1/\sqrt{3} \\ 0 \end{pmatrix}, \vec{k}_y = \frac{4\pi}{a}\begin{pmatrix} 1 \\ 1/\sqrt{3} \\ 0 \end{pmatrix}, \vec{k}_z = \frac{2\pi}{c}\begin{pmatrix} 0 \\ 0 \\ 1 \end{pmatrix}. \quad (1.3)$$

Chapter 2

Lattice-driven magnon dynamics

Our aim is to calculate magnetic excitations in α-MnTe. Therefore, we focus on the spins of the Mn $3d$ orbitals, which form a total spin of $5/2$ at each Mn site. We model the interaction between these spins with a Heisenberg Hamiltonian. Since we consider excitations at very low temperatures, we treat the model according the linear spin wave theory.

The results presented in this chapter were also published in Ref. [36]. Most of the figures are reprinted with permission from [36], copyright (2021) by the American Physical Society.

First, we introduce the model in Sec. 2.1 and the methods in Sec. 2.2. In Sec. 2.3, we examine the porperties in equilibrium. Next, we calculate the dynamics out of equilibrium in Sec. 2.4.

2.1 Model

The hybridization between Mn-Mn and Mn-Te orbitals leads to hopping between the orbitals. Due to a large Coulomb repulsion U and the semicondcutor properties of the material, this hopping can be interpreted as a Heisenberg coupling $J = 4t^2/U$. We obtain an effective Heisenberg Hamiltonian:

$$H = J \sum_{\langle i,j \rangle} \vec{S}_i \vec{S}_j, \tag{2.1}$$

which describes the interaction between two neighboring spins $\vec{S}_i$ and $\vec{S}_j$.

As depicted in Fig. 2.1, we consider three different types, which leads to the Hamiltonian:

$$H = J_1 \sum_{\langle i,j \rangle_c} \vec{S}_i \vec{S}_j + J_2 \sum_{\langle i,j \rangle_{ab}} \vec{S}_i \vec{S}_j + J_3 \sum_{\langle\langle i,j \rangle\rangle} \vec{S}_i \vec{S}_j. \tag{2.2}$$

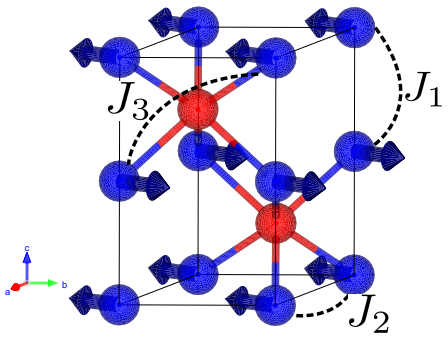

Figure 2.1: A sketch of the unit cell of MnTe including the considered Heisenberg couplings J_1, J_2, and J_3. Figure taken from Ref. [36].

Neighboring spins of different layer couple with J_1, while J_2 is the coulpling between neighboring spins of the same layer. The interaction corresponding to J_3 couples spins that are not direct neighbors. There is always a Te ion between the correspondig Mn sites.

The laser pulses applied in experiments act on the dipoles formed by the Mn and Te ions and induce optical phonons. These lattice vibrations imply a change between the distance of the ions. Since the coupling J_3 is mediated via a Te ion, we assume that the distance change leads to a change of the Heisenberg coupling J_3:

$$J_3 \to J_3(t) = J_3^{(0)} + \delta J_3(t). \tag{2.3}$$

In addition to the equilibrium value $J_3^{(0)}$ which is given by the parameter set, we consider a time-dependent change $\delta J_3(t)$ that should include all changes induced by the laser field. The effect of a time-dependent coupling is investigated further in Sec. 2.4. In general, also other Heisenberg couplings could be time-dependent due to phonon excitations. This specific aspect is explored in Sec. 2.4.3.

2.2 Methods

We target the description of low lying magnon excitations using the linear spin wave theory. We represent the spins by the Holstein-Primakoff representation [37]:

$$S_i^z = -S + \tilde{b}_i^\dagger \tilde{b}_i \tag{2.4a}$$

$$S_i^+ = \tilde{b}_i^\dagger \sqrt{2S - \tilde{b}_i^\dagger \tilde{b}_i} \approx \sqrt{2S}\tilde{b}_i^\dagger \tag{2.4b}$$

$$S_i^- = \sqrt{2S - \tilde{b}_i^\dagger \tilde{b}_i}\tilde{b}_i \approx \sqrt{2S}\tilde{b}_i, \tag{2.4c}$$

where $\tilde{b}_i$ ($\tilde{b}_i^\dagger$) is the bosonic annihilation (creation) operator. We approximate $\sqrt{2S - \tilde{b}_i^\dagger \tilde{b}_i} \approx \sqrt{2S}$ by keeping only the first order term of a $1/S$ expansion, which is the key property of the linear spin wave theory [38, 39]. This approach is justified in the antiferromagnetic phase since the spin of $S = 5/2$ and the number of nearest neighbors are large. However, we should restrict this modeling to small magnon occupations $\langle \tilde{b}_i^\dagger \tilde{b}_i \rangle$. Next, we apply a Fourier transform

$$\tilde{b}_i = \frac{1}{\sqrt{N}} \sum_{\vec{k}} \exp\left(i\vec{k} \cdot \vec{l}_i\right) \tilde{b}_{\vec{k}} \tag{2.5}$$

to switch from real space into momentum space. We obtain the Hamiltonian

$$\frac{H_0}{J_1 S} = E_d + \sum_{\vec{k}} \left[A_{\vec{k}} \tilde{b}_{\vec{k}}^\dagger \tilde{b}_{\vec{k}} + \frac{1}{2} B_{\vec{k}} \left(\tilde{b}_{\vec{k}}^\dagger \tilde{b}_{-\vec{k}}^\dagger + \text{h.c.} \right) \right] \tag{2.6}$$

with the parameters

$$A_{\vec{k}} := \frac{1}{J_1} \Big(2J_1 - 6J_2 + 12J_3 + J_2 \gamma_\Delta(\vec{k}) \Big) \tag{2.7a}$$

$$B_{\vec{k}} := 2\cos(ck_z) \Big(1 + 2\frac{J_3}{J_1} \gamma_\Delta\left(\vec{k}\right) \Big) \tag{2.7b}$$

$$\gamma_\Delta\left(\vec{k}\right) := \cos(ak_x) + \cos\left(\frac{a}{2}k_x + \frac{\sqrt{3}a}{2}k_y\right) + \cos\left(-\frac{a}{2}k_x + \frac{\sqrt{3}a}{2}k_y\right)$$

The Hamiltonian (2.6) is almost diagonal in $\vec{k}$, except of the coupling between $\vec{k}$ and $-\vec{k}$ which corresponds to the creation and annihilition of magnon pairs. Because of the new representation, the Hamiltonian has a momentum-independent energy offset

$$E_d = -NS \left(1 - 3\frac{J_2}{J_1} + 6\frac{J_2}{J_1} \right). \tag{2.8}$$

The Bogoliubov transformation

$$\tilde{b}_{\vec{k}} = b_{\vec{k}} \cosh\theta_{\vec{k}} + b_{-\vec{k}}^\dagger \sinh\theta_{\vec{k}} \tag{2.9}$$

is suitable to obtain the diagonal Hamiltonian

$$\frac{H_0}{J_1 S} = \sum_{\vec{k}} \omega_{\vec{k}} b_{\vec{k}}^\dagger b_{\vec{k}} + E_d + \Delta E. \tag{2.10}$$

The Bogoliubov angle θ needs to fulfill the condition

$$\frac{B_{\vec{k}}}{A_{\vec{k}}} = -\tanh(\theta_{\vec{k}}). \tag{2.11}$$

The transformation generates an additional contributation to the ground state energy:

$$\Delta E = \frac{1}{2N} \sum_{\vec{k}} \left(\omega_{\vec{k}} - A_{\vec{k}}\right). \tag{2.12}$$

Both energy offsets (2.8) and (2.12) do not affect the magnon excitations. The magnon dispersion in units of J_1 is finally given by

$$\omega_{\vec{k}} = \sqrt{A_{\vec{k}}^2 - B_{\vec{k}}^2} \geq 0. \tag{2.13}$$

This equation can be evaluated for any given set of coupling parameters J_i.

2.3 Equilibrium properties

While Ref. [40] suggests to include three types of nearest neighbors to model our material, Ref. [41] offers a model with four types of nearest neighbors. The fitted coupling constants differ within different approaches, but all approaches lead to similar dispersions, which is the most important for our calculations. We choose the parameter set suggested by Ref. [40]: $J_1 = 21.5\,\mathrm{K}, J_2 = -0.67\,\mathrm{K}$, and $J_3 = 2.87\,\mathrm{K}$[1]. The chosen parameter set produces no competing interactions since all spin-spin interactions favor the actual magnetic order.

We evaluate the magnon dispersion of Eq. (2.13) for given paths through the Brillouin zone as well as the magnon density of states.

The dispersion is shown as blue lines in Fig. 2.2(a). Near the Γ point, only small energies are needed to excite magnons, and the dispersion is linear. Near to the edges of the Brillouin zone maxima are reached. The parameters we use were obtained by fitting neutron scattering experiments. This experimental data [40] added as black dots shows a good agreement with our curves. However, subtle details, such as the dip at the end of path $\Gamma \to M$, are not capured by our nearest-neighbor description. Probably this is due to neglecting spin-spin interactions at larger distances. In addition, we see small but systematic deviations concerning the absolute value of the energy in the paths $\Gamma \to K$ and $\Gamma \to H$. But a global factor could not fix that

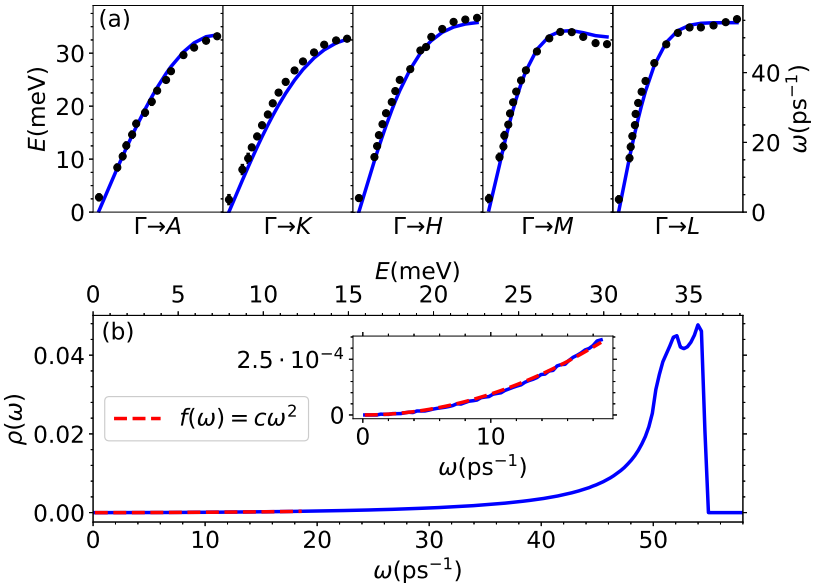

Figure 2.2: The magnon dispersion (a) and the magnon density of states (b). The DOS shows a quadratic increase for small energies as indicated by the red dashed curve, which is especially visible in the inset. For energies near to the maximium energy, two van Hove singularities emerge. Figure taken from Ref. [36].

problem since the deviations in theses paths are in opposite directions, and the other paths do not show these systematic deviations.

The magnon density of states

$$\rho(\omega) = \frac{1}{N} \sum_{\vec{k}} \delta(\omega - \omega_{\vec{k}}) \tag{2.14}$$

with N $\vec{k}$ points is depicted as blue line in panel (b) of Fig. 2.2. We use the analytic results for a triangluar lattice derived in Ref. [42] for the Mn layers to simplify the problem. For small frequencies, the DOS grows quadratically

$$f(\omega) = c\omega^2 \tag{2.15}$$

with $c = (9.40 \pm 0.04) \times 10^{-7}$ ps illustrated as red dashed line, which is typical for a linear dispersion in three dimensions. The maximum of the magnon dispersion

[1] Due to a different notation of the Hamiltonian in this thesis compared to Ref. [40], the Heisenberg couplings have opposite signs and a factor 2 is included.

determines the maximum energy $\hbar\omega_{\max} \approx 35.9\,\mathrm{meV}$ for the support of the DOS. The peaks near to this maximum energy correspond to van Hove singularities. Most of the spectral weight lies close to the maximum energy.

2.4 Dynamics out of equilibrium

Considering the time-dependent change of the Heisenberg couplings

$$J_i(t) = J_i^{(0)} + \delta J_i(t) \tag{2.16}$$

due to phonon osciallations induced by the laser pulses, we expect magnon excitations. Consequently, we have to extend the Hamiltonian defined in Eq. (2.10) by a time-dependent pertubation $X(t)$:

$$H(t) = H_0 + X(t). \tag{2.17}$$

We assume that the pulses change the Heisenberg couplings such that a periodic change appears with the phonon frequency ω_0. Since the phonon excitation decays, the change of the coupling should also decrease, which we model by an exponential envelope with decay rate γ. The parameter $a_{0,i}$ governs the strength of the change. Finally, the change of a Heisenberg coupling is given by

$$\frac{\delta J_i(t)}{S J_1^{(0)}} = a_i(t) = a_{0,i} \exp(-\gamma t) \cos(\omega_0 t). \tag{2.18}$$

For several comparisons, $a_{0,i}$ is expressed as relative change:

$$a_{0,i} = \delta J_i(0)/J_1^{(0)} = (J_i/J_1^{(0)})\kappa_i. \tag{2.19}$$

As discussed above, a time-dependent $J_3(t)$ is most likely in the system since it decribes interactions between spins localized on Mn ions between which is a Te ion. The pertubation $X(t)$ has then the form

$$X(t) = S\delta J_3(t) \sum_{\vec{k}} \left[\alpha_{\vec{k}} b_{\vec{k}}^\dagger b_{\vec{k}} + \frac{1}{2}\beta_{\vec{k}} \left(b_{\vec{k}}^\dagger b_{\vec{k}}^\dagger + \mathrm{h.c.} \right) + C_{\vec{k}} \right] \tag{2.20}$$

after the Bogoliubov transformation. The coefficients are

$$\alpha_{\vec{k}} = \frac{A_{\vec{k}}}{\omega_{\vec{k}}} \left(12 - 4\frac{B_{\vec{k}}}{A_{\vec{k}}} \cos(k_c)\gamma_\triangle(\vec{k}) \right), \tag{2.21a}$$

$$\beta_{\vec{k}} = \frac{A_{\vec{k}}}{\omega_{\vec{k}}} \left(-12\frac{B_{\vec{k}}}{A_{\vec{k}}} + 4\cos(k_c)\gamma_\triangle(\vec{k}) \right). \tag{2.21b}$$

We abbreviate the appearing expectation values

$$u_{\vec{k}} := \langle n_{\vec{k}} \rangle = \langle b^\dagger_{\vec{k}} b_{\vec{k}} \rangle \tag{2.22a}$$

$$v_{\vec{k}} := \mathrm{Re}\, \langle b^\dagger_{\vec{k}} b^\dagger_{-\vec{k}} \rangle \tag{2.22b}$$

$$w_{\vec{k}} := \mathrm{Im}\, \langle b^\dagger_{\vec{k}} b^\dagger_{-\vec{k}} \rangle. \tag{2.22c}$$

Via the Heisenberg's equation, we calculate the resulting closed set of differential equations

$$\frac{du_{\vec{k}}}{dt} = 2a(t)\beta_{\vec{k}} w_{\vec{k}} - \gamma_r u_{\vec{k}} \tag{2.23a}$$

$$\frac{dv_{\vec{k}}}{dt} = -2(\omega_{\vec{k}} + a(t)\alpha_{\vec{k}}) w_{\vec{k}} - \gamma_r v_{\vec{k}} \tag{2.23b}$$

$$\frac{dw_{\vec{k}}}{dt} = 2(\omega_{\vec{k}} + a(t)\alpha_{\vec{k}}) v_{\vec{k}} + 2a(t)\beta_{\vec{k}}(u_{\vec{k}} + 1/2) - \gamma_r w_{\vec{k}}. \tag{2.23c}$$

Note that these equations do not couple different $\vec{k}$ modes since we consider only the linear contributions in the frame of the linear spin wave theory. However, in a real material, there should be a relaxation mechanism for the magnons. To describe this relaxation phenomenologically in our model, we introduce γ_r as decay rate for the magnons.

2.4.1 Magnon dynamics of a single mode

Analyzing the dynamics of a single mode enables us to understand the effect of the driving term $a(t)$ before considering the sum of all $\vec{k}$ modes. Let us begin with the simplest case when the driving term has vanished ($a(t) = 0$) and the relaxation is neglected ($\gamma_r = 0$). The magnon occupation just stays constant in this case

$$\frac{du_{\vec{k}}(t)}{dt} = 0 \Rightarrow u_{\vec{k}}(t) = \text{const.}, \tag{2.24}$$

while the Bogoliubov terms describe coherent oscillations

$$v_{\vec{k}}(t) = c_0 \cos(2\omega_{\vec{k}} t + \varphi) \tag{2.25a}$$

$$w_{\vec{k}}(t) = c_0 \sin(2\omega_{\vec{k}} t + \varphi) \tag{2.25b}$$

with the frequency $2\omega_k$ originated from the magnon pair creation and annihilation. The initial conditions determine the values of the amplitude c_0 and the phase φ. Introducing the damping ($\gamma_r > 0$) yields a decrease by the factor of $\exp(-\gamma_r t)$ of the magnon occupation u_k as well as of the amplitude of $v_{\vec{k}}$ and $w_{\vec{k}}$.

Analytic approximations of Bogoluibov term dynamics

We aim also a more general approximated analytic solutions of the differential equations by considering $\omega_{\vec{k}} \gg a(t)\alpha_{\vec{k}}$, which holds for small driving terms. We neglect any relaxation, which leads us to the simplified set of differential equations

$$\frac{du_{\vec{k}}}{dt} = 2a(t)\beta_{\vec{k}} w_{\vec{k}} \tag{2.26a}$$

$$\frac{dv_{\vec{k}}}{dt} = -2(\omega_{\vec{k}} + a(t)\alpha_{\vec{k}}) w_{\vec{k}} \tag{2.26b}$$

$$\frac{dw_{\vec{k}}}{dt} = 2(\omega_{\vec{k}} + a(t)\alpha_{\vec{k}}) v_{\vec{k}} + f_{\vec{k}}(t) \tag{2.26c}$$

$$\text{with} \qquad f_{\vec{k}}(t) := 2a(t)\beta_{\vec{k}}(u_{\vec{k}} + 1/2). \tag{2.26d}$$

By introducing $z_{\vec{k}}(t) = \langle b^\dagger_{\vec{k}} b^\dagger_{-\vec{k}} \rangle = v_{\vec{k}}(t) + i w_{\vec{k}}(t)$, we combine the differential equations for the Boguliubov terms of Eqs. (2.23b), and (2.23c) in the following way

$$\frac{dz_{\vec{k}}}{dt} = 2i(\omega_{\vec{k}} + a(t)\alpha_{\vec{k}}) z - \gamma_r z + i f_{\vec{k}}(t) \tag{2.27}$$

with

$$f_{\vec{k}}(t) = 2a(t)\beta\vec{k}(u_{\vec{k}}(t) + 1/2) \tag{2.28a}$$

$$a(t) = a_0 \cos(\omega_0 t) \exp(-\gamma t). \tag{2.28b}$$

After neglecting $a(t)\alpha_{\vec{k}}$, we obtain the simpler equation

$$\frac{dz_{\vec{k}}}{dt} = (2i\omega_{\vec{k}} - \gamma_r) z + i f_{\vec{k}}(t), \tag{2.29}$$

which is solved by

$$z_{\vec{k}}(t) = i e^{(2i\omega_{\vec{k}} - \gamma_r)t} \int_0^t a(t')\beta_{\vec{k}}(2u_{\vec{k}}(t') + 1) e^{-(2i\omega_{\vec{k}} - \gamma_r)t'} dt'. \tag{2.30}$$

Considering small magnon occupations $2u_{\vec{k}}(t') \ll 1$ allows us to neclect $u_{\vec{k}}(t')$ in the integral, which yields the approximate solution

$$\begin{aligned} z_{\vec{k}}(t) = i a_0 \beta_{\vec{k}} \Bigg[& \frac{e^{-\gamma t}(\omega_0 \sin(\omega_0 t) - (2i\omega_{\vec{k}} + \gamma - \gamma_r)\cos(\omega_0 t))}{\omega_0^2 - (2\omega_{\vec{k}} - i(\gamma - \gamma_r))^2} \\ & + \frac{(2i\omega_{\vec{k}} + \gamma - \gamma_r) e^{2i\omega_{\vec{k}} t} e^{-\gamma_r t}}{\omega_0^2 - (2\omega_{\vec{k}} - i(\gamma - \gamma_r))^2} \Bigg]. \end{aligned} \tag{2.31}$$

This results offers us already a lot of insights. The coherent oscillations with $2\omega_{\vec{k}}$ damped by γ_r can be also found in this solution in the second term. Induced osciallations with ω_0, which are damped by γ, dominate the first term. The resonance condition $\omega_0 = 2\omega_{\vec{k}}$ in absence of any decay can be read in the denominator.

A more detailed analysis is required for the very special case $\omega_0 \to 2\omega_{\vec{k}}$ when $\gamma = \gamma_r$. We reformulate $2\omega_{\vec{k}}$ near to the resonance with the small detuning δ: $2\omega_{\vec{k}} = \omega_0 + \delta$. Next, we consider Eq. (2.31) in the limit $\delta \to 0$ and obtain a linearly increasing amplitude:

$$z_{\vec{k}}(t) = \frac{i a_0 \beta_{\vec{k}}}{2} e^{-\gamma t}\left(t e^{i\omega_0 t} + \frac{1}{\omega_0}\sin(\omega_0 t)\right). \tag{2.32}$$

However, the two decay rates in the experiments considered for this work differ significantly so that this case has no practical importance.

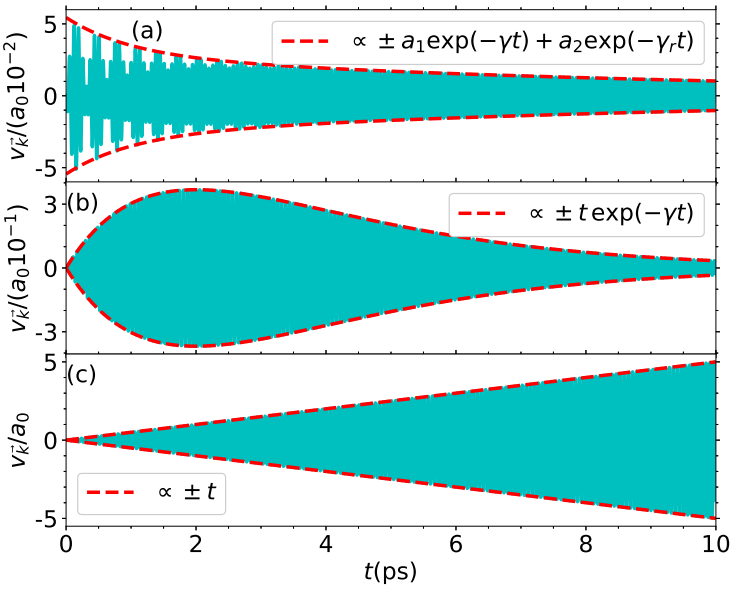

Figure 2.3: The dynamics of the Bogoliubov term $v_{\vec{k}}$ according Eqs. (2.31) and (2.32) for different representative cases: (a) Off-resonant driving with $\omega_0 = 100\,\mathrm{ps}^{-1}$, $\omega_{\vec{k}} = 80\,\mathrm{ps}^{-1}$, $\gamma = 1.0\,\mathrm{ps}^{-1}$, and $\gamma = 0.1\,\mathrm{ps}^{-1}$. Resonant driving for $2\omega_{\vec{k}} = \omega_0 = 100\,\mathrm{ps}^{-1}$ with (b) $\gamma = \gamma_r = 0.5\,\mathrm{ps}^{-1}$ and (c) $\gamma = \gamma_r = 0$ (Parameters: $\kappa = 0.01, \beta = 1$). Figure taken from Ref. [36].

Analytic approximations of magnon occupation dynamics

We find also analytic approximations for the magnon occupations. To simplify the calculations, we omit the relaxation ($\gamma_r = 0$) since we know that this only yields an exponentially decreasing factor in the result.

We start again with Eq. (2.27) and insert $a(t) = a_0 \cos(\omega_0 t)$:

$$\frac{dz_{\vec{k}}}{dt} = 2i(\omega_{\vec{k}} + a_0 \cos(\omega_0 t)\alpha_{\vec{k}})z_{\vec{k}} + if_{\vec{k}}(t).$$

The general solution is

$$z_{\vec{k}}(t) = ie^{ih_{\vec{k}}(t)} \int_0^t f_{\vec{k}}(t')e^{-ih_{\vec{k}}(t')}dt' \tag{2.33a}$$

$$\text{with } h_{\vec{k}}(t) := 2\int_0^t (\omega_{\vec{k}} + a_0\alpha_{\vec{k}} \cos(\omega_0 t'))dt' \tag{2.33b}$$

$$= 2\omega_{\vec{k}} t + 2\frac{a_0\alpha_{\vec{k}}}{\omega_0} \sin(\omega_0 t). \tag{2.33c}$$

The integration of Eq. (2.26a) with taking into account $w_{\vec{k}} = \mathrm{Im}(z_{\vec{k}})$ yields

$$u_{\vec{k}}(t) = 2a_0\beta_{\vec{k}} \int_0^t \cos(\omega_0 t')\mathrm{Im}z_{\vec{k}}dt'. \tag{2.34}$$

The solution $u_{\vec{k}}(t)$ will show fast oscillations with frequency $2\omega_0$ and a slow development. In order to focus on the evolution on a large time scale, we integrate over one period $T_0 = 2\pi/\omega_0$, which includes replacing $\cos(\omega_0 t)e^{-ih_{\vec{k}}(t)}$ in Eq. (2.33a) by its average.

In the resonant case $\omega_0 = 2\omega_{\vec{k}}$, we obtain

$$\phi^{-1}J_1(\phi) = \frac{1}{T_0}\int_0^{T_0} \cos(\omega_0 t')e^{-i\omega_0 t' - i\phi\sin(\omega_0 t')}dt' \tag{2.35}$$

with $\phi = 2a_0\alpha_{\vec{k}}/\omega_0$. The approximation (2.35) is applicable if the osciallations are much faster than the slow evolution. This depends strongly on the parameters ω_0, γ, and γ_r. If $\gamma \ll \omega_0$ and $\gamma_r \ll \omega_0$, our procedure is well justified. For the experimentally reasonable parameters, this is the case.

We obtain

$$z_{\vec{k}}(t) = i\frac{\beta_{\vec{k}}\omega_0}{\alpha_{\vec{k}}} J_1(\phi)e^{i_{\vec{k}}h_{\vec{k}}(t)} \int_0^t \left(u_{\vec{k}}(t') + 1/2\right) dt' \tag{2.36}$$

with the Bessel function of the first kind $J_1(x)$. Next, we insert Eq. (2.36) into Eq. (2.34), and we average according Eq. (2.35), which leads to

$$u_{\vec{k}}(t) = \Gamma^2 \mathrm{Re} \int_0^t \int_0^{t'} (u_{\vec{k}}(t'') + 1/2) dt'' dt' \tag{2.37a}$$

$$\Gamma := \left(\frac{\beta_{\vec{k}} \omega_0}{\alpha_{\vec{k}}} \right) J_1(\phi). \tag{2.37b}$$

The simple differential equation

$$u''_{\vec{k}}(t) = \Gamma^2 \left(u_{\vec{k}}(t) + 1/2 \right) \tag{2.38}$$

follows by differentiating twice. Solving this differential equations for the initial condition $u_{\vec{k}}(t=0) = 0$ yields

$$u_{\vec{k}}(t) \quad = \quad \frac{1}{2}(\cosh(\Gamma t) - 1) \tag{2.39a}$$

with

$$\Gamma \quad := \quad \frac{\beta_{\vec{k}} \omega_0}{\alpha_{\vec{k}}} J_1\Big(\frac{2 a_0 \alpha_{\vec{k}}}{\omega_0} \Big) \approx a_0 \beta_{\vec{k}}. \tag{2.39b}$$

We have to keep in mind that Eq. (2.39a) is only reliable for small $u_{\vec{k}}(t)$ since the linear spin wave theory is only valid for this case.

Next, we extend the approximation to detuned frequencies and define therefore the detuning $\delta := 2\omega_{\vec{k}} - \omega_0$. If we consider small detuning $|\delta| \ll \omega_0$, we are able to apply similar steps as for resonant driving. We start again with the same replacement (2.35) of the fast oscillations by the average over one period and obtain

$$z_{\vec{k}}(t) = i \frac{\beta_{\vec{k}} \omega_0}{\alpha_{\vec{k}}} J_1(\phi) e^{i \vec{k} h_{\vec{k}}(t)} \int_0^t \left(u_{\vec{k}}(t') + 1/2 \right) e^{-i\delta t'} dt'. \tag{2.40}$$

We put the expression into Eq. (2.36) and apply the averaging again, which yields

$$u_{\vec{k}}(t) = \Gamma^2 \mathrm{Re} \int_0^t e^{i\delta t'} \int_0^{t'} e^{-i\delta t''} (u_{\vec{k}}(t'') + 1/2) dt'' dt'. \tag{2.41}$$

Unforetunately, differentiating twice does not yield a closed differential equation as for the resonant case because of the factor $e^{i\delta t}$. But with a triple differentiation, we obtain

$$u'''_{\vec{k}}(t) = (\Gamma^2 - \delta^2) u'_{\vec{k}}(t). \tag{2.42}$$

Taking into account the initial conditions are $u_{\vec{k}}(t=0)=0$, $u'_{\vec{k}}(t=0)=0$, and $u''_{\vec{k}}(t=0)=\Gamma^2/2$ yields

(A) $\Gamma > |\delta|$

$$u_{\vec{k}}(t) = \frac{1}{2}\frac{\Gamma^2}{\Gamma'^2}(\cosh(\Gamma' t)-1) \tag{2.43a}$$

$$\text{with } \Gamma' := \sqrt{|\Gamma^2-\delta^2|} \tag{2.43b}$$

(B) $\Gamma < |\delta|$

$$u_{\vec{k}}(t) = \frac{1}{2}\frac{\Gamma^2}{\Gamma'^2}(1-\cos(\Gamma' t)). \tag{2.43c}$$

The solution depends on the sign of $\Gamma^2-\delta^2$. On the one hand, for $\Gamma^2-\delta^2>0$, the magnon occupation follows $\cosh(\Gamma' t)$ similar to the resonant case since the detuning is very small. On the other hand, for $\Gamma^2-\delta^2<0$, the magnon occupation oscillates with $\cos(\Gamma' t)$.

Figure 2.4 shows the analytic approximations (dashed lines) in comparison to the full numerical solution (solid lines) of Eqs. (2.23). While panel (a) focuses on the slow evolution, the fast osciallations of $u_{\vec{k}}$ of the full solution are visible in panel (b). Since we integrate these oscillations out in the analytic approach, the analytic curves show only the slow development, which agrees very well with the long-time evolution of the full solution.

Let us focus on the slow evolution. The resonant driving leads to a constantly increasing magnon occupation (blue curve). For very small detuning ($\Gamma > |\delta|$, case (A)), the curve would look very similar and is therefore not shown. This behavior is very important for our numerical calculations. Since a discrete grid can easily overlook the $\vec{k}$ points with perfect resonance, the finite sum over all $\vec{k}$ points needs to be also accurate by taking into account $\vec{k}$ points near to the resonance. However, for slightly larger detuning ($\Gamma < |\delta|$), case (B)), the magnon occupation oscillates with $\Gamma' := \sqrt{|\Gamma^2-\delta^2|}$ (red and orange curve). On a very short time scale the magnon occupation shows a similar development as for resonant driving, but it changes significantly for larger times. The smaller the frequency Γ' of the slow osciallations, the longer similar curve developments appear. However, when $\Gamma > |\delta|$, the evolution changes completely entering case (A).

In a second step, we want to include damping of the driving term ($\gamma > 0$). In consequence, the driving term is extended by an exponentional decay : $a(t) =$

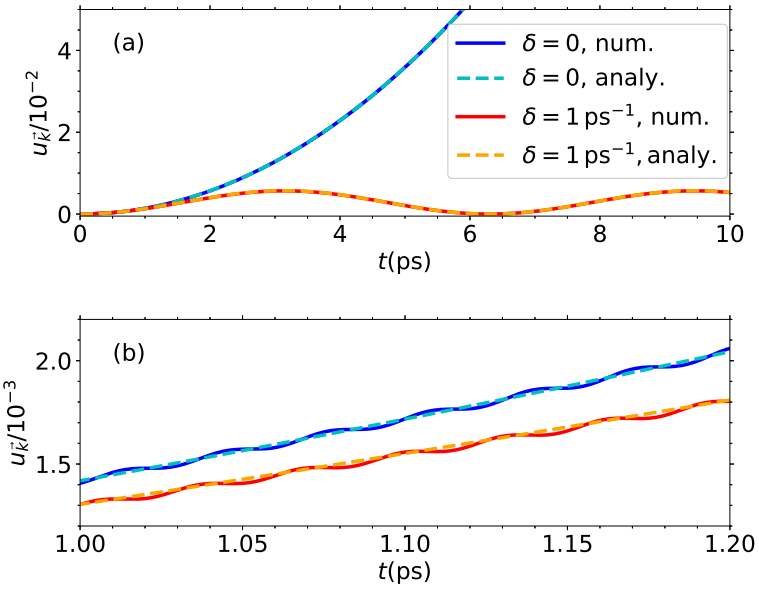

Figure 2.4: The magnon occupation $u_{\vec{k}}$ for a single mode with $\kappa = 0.01, \Gamma = 0.0753\,\mathrm{ps}^{-1}, \Gamma' = 0.9972\,\mathrm{ps}^{-1}$ for resonant driving ($\delta = 0$, dark and light blue) and the off-resonant driving ($\delta = 1\,\mathrm{ps}^{-1}$, red and orange). The solid line represents the numerical results obtained by solving the differential equations (2.23), while the dashed lines illustrates the approximate analytical solutions (2.39a) and (2.43c). Panel (a): full time interval; panel (b): zoom of panel (a) to show the fast oscillations. Figure taken from Ref. [36].

$a_0 \cos(\omega_0 t) \exp(-\gamma t)$. The solution (2.33a) derived for driving without damping is still valid if we consider an adapted definition of $h_{\vec{k}}$:

$$h_{\vec{k}}(t) := 2 \int_0^t (\omega_{\vec{k}} + a_0 \alpha_{\vec{k}} \cos(\omega_0 t') \exp(-\gamma t)) dt' \tag{2.44a}$$

$$= 2\omega_{\vec{k}} t + 2 \frac{a_0 \alpha_{\vec{k}}}{\omega_0^2 + \gamma^2} [e^{-\gamma t}(\omega_0 \sin(\omega_0 t) - \gamma \cos(\omega_0 t)) + \gamma] \tag{2.44b}$$

$$\approx 2\omega_{\vec{k}} t. \tag{2.44c}$$

However, we have to consider the limit of small driving strength $a_0 \to 0$. Only by neglecting the time dependence in ϕ, we are able to proceed analytically. Although this conditions excludes several sets of parameters, it is valid for an experimentally interesting range of parameters. In addition, the following analytical approximations allow us an insight into the magnon dynamics on a qualitative level. Therefore, we

stick to Eq. (2.44c) and the averaging

$$1/2 = \frac{1}{T_0}\int_0^{T_0} \cos(\omega_0 t')e^{-i\omega_0 t'}dt', \tag{2.45}$$

and we obtain

$$z_{\vec{k}}(t) = i\Gamma e^{i_{\vec{k}}h_{\vec{k}}(t)}\int_0^t e^{-\gamma t'}\left(u_{\vec{k}}(t') + 1/2\right)dt'. \tag{2.46}$$

Inserting this result in

$$u_{\vec{k}}(t) = 2\Gamma\int_0^t \cos(\omega_0 t')e^{-\gamma t}\mathrm{Im}z_{\vec{k}}dt' \tag{2.47}$$

and averaging over one period yield

$$u_{\vec{k}}(t) = \Gamma^2\int_0^t dt'e^{-\gamma t'}\int_0^{t'} dt''e^{-\gamma t''}(u_{\vec{k}}(t'') + 1/2). \tag{2.48}$$

We can neglect $u_{\vec{k}}$ in the integrand if the magnon occupation is very low ($2u_{\vec{k}} \ll 1$). By integrating twice, we obtain

$$u_{\vec{k}}(t) = \frac{\Gamma^2}{4\gamma^2}(1-\exp(-\gamma t))^2 \underset{t\to\infty}{\to} \frac{\Gamma^2}{4\gamma^2}. \tag{2.49}$$

A second approach is to derive the differential equation

$$u''_{\vec{k}} = \Gamma^2 e^{-2\gamma t}(u_{\vec{k}} + 1/2) - \gamma u'_{\vec{k}} \tag{2.50}$$

by differentiating twice Eq. (2.48). However, the resulting equation has to be solved numerically taking into account the initial conditions $u_{\vec{k}}(0) = 0 = u'_{\vec{k}}(0)$ since there is no closed expression solving it.

Considering the detuned driving ($\delta \neq 0$), we obtain

$$u_{\vec{k}}(t) = \Gamma^2\mathrm{Re}\int_0^t dt'e^{(i\delta-\gamma)t'}\int_0^{t'} dt''e^{-(i\delta+\gamma)t''}\left(u_{\vec{k}}(t'') + \frac{1}{2}\right). \tag{2.51}$$

Similar to the resonant case, we can choose between neglecting $u_{\vec{k}}$ in the integrand, which yields

$$u_{\vec{k}}(t) = \frac{\Gamma^2}{4(\gamma^2+\delta^2)}|\exp(i\delta t) - \exp(-\gamma t)|^2 \tag{2.52a}$$

$$\underset{t\to\infty}{\to} \frac{\Gamma^2}{4(\gamma^2+\delta^2)}, \tag{2.52b}$$

or to differentiate three times to obtain

$$u'''_{\vec{k}} = \left(\Gamma^2 e^{-2\gamma t} - \delta^2 - \gamma^2\right) u'_{\vec{k}} \\ - 2\gamma u''_{\vec{k}} - \gamma\Gamma^2 e^{-2\gamma t}(u_{\vec{k}}(t) + 1/2), \tag{2.53}$$

which can be solved numerically with the initial conditions $u_{\vec{k}}(0) = 0 = u'_{\vec{k}}(0)$ and $u''_{\vec{k}}(0) = \Gamma^2/2$.

Figure 2.5 depicts the analytic approximation (2.49) and (2.52) compared to the numerical solution. While Fig. 2.5(a) shows the full time evolution including the reaching the limit value, panel (b) focuses on a short time interval, such that the oscillations of the numeric solution can be seen.

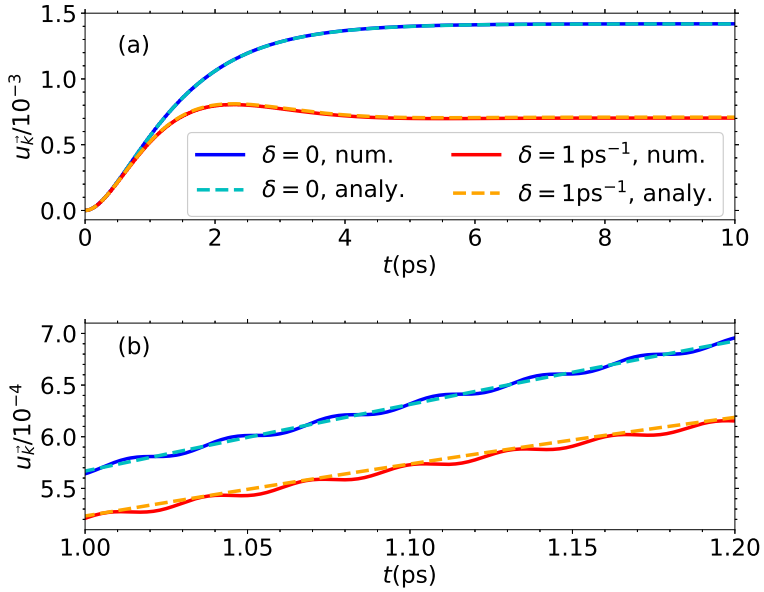

Figure 2.5: The magnon occupation $u_{\vec{k}}(t)$ of a single magnon mode with $\omega_{\vec{k}} = 50\,\mathrm{ps}^{-1}, \kappa = 0.01, \beta_{\vec{k}} = 1, \Gamma = 0.0753\,\mathrm{ps}^{-1}, \Gamma' = 0.9972\,\mathrm{ps}^{-1}$ for damped resonant ($\delta = 0$, dark and light blue) and damped off-resonant ($\delta = 1\,\mathrm{ps}^{-1}$, red and orange) driving. The solid curves show the full numerical solutions of the Eqs. (2.23), in contrast to the dashed curves representing the analytical approximations Eqs. (2.49) and (2.52). Panel (a): full time interval; panel (b): zoom of panel (a) to show the fast oscillations. Figure adapted from Ref. [36].

Finally, we want to include the phenomenological magnon relaxation ($\gamma_r > 0$). We already know that it induces an exponentially decreasing amplitude in $z_{\vec{k}}$, and we

will see that the effect on the magnon occupation is similar. The general Eqs. (2.23) and (2.27) serve as a starting point. We obtain

$$u_{\vec{k}}(t) = 2\Gamma e^{-\gamma_r t} \int_0^t \cos(\omega_0 t') e^{(\gamma_r-\gamma)t'} \mathrm{Im} z_{\vec{k}}(t') dt' \tag{2.54}$$

by integrating $u_{\vec{k}}$, while integrating Eq. (2.27) leads to

$$z_{\vec{k}}(t) = i e^{ih_{\vec{k}}-\gamma_r t} \int_0^t f_{\vec{k}}(t') e^{-ih_{\vec{k}}+\gamma_r t'} dt'. \tag{2.55}$$

The steps are equivalent to the procedure presented before: the fast oscillations in Eq. (2.55) are neglected by averaging over one period (cf. Eq. (2.45) and are inserted into Eq. (2.54)). After averaging once again, we obtain

$$u_{\vec{k}}(t) = \Gamma^2 e^{-\gamma_r t} \int_0^t dt' e^{-\gamma t'} \int_0^{t'} dt'' e^{-\gamma t''} (u_{\vec{k}} + e^{\gamma_r t''}/2) \tag{2.56}$$

for resonant driving ($\omega_0 = 2\omega_{\vec{k}}$). For convinence, we define

$$\tilde{u}_{\vec{k}}(t) := \exp(\gamma_r t) u_{\vec{k}}(t). \tag{2.57}$$

Next, we differentiate $\tilde{u}_{\vec{k}}(t)$ twice, which yields

$$\tilde{u}''_{\vec{k}}(t) = -\gamma \tilde{u}'_{\vec{k}} + \Gamma^2 e^{-2\gamma t} \left(e^{-\gamma_r t} \tilde{u}_{\vec{k}} + e^{\gamma_r t}/2 \right). \tag{2.58}$$

This equation could be solved numerically for the initial conditions $\tilde{u}_{\vec{k}}(t=0) = 0, = \tilde{u}'_{\vec{k}}(t=0) = 0$.

The second approach is to consider only small magnon occupations $u_{\vec{k}}$, which enables us to analytically integrate Eq. (2.56):

$$u_{\vec{k}}(t) = \frac{\Gamma^2}{2} \frac{(\gamma-\gamma_r)e^{-\gamma_r t} + \gamma e^{-2\gamma t} - (2\gamma-\gamma_r)e^{-(\gamma+\gamma_r)t}}{\gamma(\gamma-\gamma_r)(2\gamma-\gamma_r)}. \tag{2.59}$$

The magnon occupation firstly grows and decreases after reaching a maximum. Due to the damping and the relaxation, two exponential decays arise: $e^{-\gamma_r t}$ and $e^{-\gamma t}$. If γ and γ_r have clearly differing values, the decays are dominant on different timescales. Otherwise, they are only recognizable as a combined effect.

At the end, we consider also detuned driving and obtain

$$u_{\vec{k}}(t) = \Gamma^2 e^{-\gamma_r t} \Re \int_0^t dt' e^{(i\delta-\gamma)t'} \int_0^{t'} dt'' e^{-(i\delta+\gamma)t''} (u_{\vec{k}} + e^{\gamma_r t''}/2). \tag{2.60}$$

Differentiating three times yields

$$\tilde{u}'''_{\vec{k}}(t) = -2\gamma\tilde{u}''_{\vec{k}} - \left(\delta^2+\gamma^2-\Gamma^2 e^{-(2\gamma+\gamma_r)t}\right)\tilde{u}'_{\vec{k}} - (\gamma+\gamma_r)\Gamma^2 e^{-(2\gamma+\gamma_r)t}\tilde{u}_{\vec{k}} - (\gamma-\gamma_r)\Gamma^2 e^{(-2\gamma+\gamma_r)t}/2. \tag{2.61}$$

This equations can once again be solved numerically for the initial conditions $\tilde{u}_{\vec{k}}(0) = 0 = \tilde{u}'_{\vec{k}}(0)$ and $\tilde{u}''_{\vec{k}}(0) = \Gamma^2/2$, while for small values of $u_{\vec{k}}$, a direct integration of Eq. (2.60) is possible:

$$\begin{aligned} u_{\vec{k}}(t) \;=\; & \frac{\Gamma^2}{2}\Bigg(\frac{(\gamma-\gamma_r)e^{-2\gamma t}}{(2\gamma-\gamma_r)(\delta^2+(\gamma-\gamma_r)^2)} \\ & -\frac{[(\delta^2-\gamma\gamma_r+\gamma^2)\cos(\delta t)+\delta\gamma_r\sin(\delta t)]e^{-(\gamma+\gamma_r)t}}{(\delta^2+\gamma^2)(\delta^2+(\gamma-\gamma_r)^2)} \\ & +\frac{\gamma e^{-\gamma_r t}}{(2\gamma-\gamma_r)(\delta^2+\gamma^2)}\Bigg). \end{aligned} \tag{2.62}$$

2.4.2 Dynamics of the sublattice magnetization

The order parameter L of an antiferromagnet is the sublattice magnetization – also called staggered magnetization. It is defined as the difference between the magnetizations of the sublattices A and B:

$$L = M_A - M_B. \tag{2.63}$$

In contrast to the total magnetization $M = M_A + M_B$, L is finite for the ordered phase, respectively below the Néel temperature T_N. For our calculations, we define the sublattice magnetization per site considering only by the z componenent:

$$L = \frac{1}{N}\sum_i (-1)^{\delta_i}\langle\hat{S}_i^z\rangle \tag{2.64}$$

$$\delta_i = \begin{cases} 0 & \text{for sublattice A} \\ 1 & \text{for sublattice B.} \end{cases}$$

By applying the same calculations as for the Hamiltonian, we obtain the sublattice magnetization

$$L = L_0 - \delta L, \tag{2.65}$$

which consists of two parts. The first term L_0 contains the spin per site $S = 5/2$ reduced by quantum fluctuations ΔS

$$L_0 = S - \Delta S \tag{2.66a}$$

$$\Delta S = \frac{1}{2N} \sum_{\vec{k}} \left(\frac{A_{\vec{k}}}{\omega_{\vec{k}}} - 1 \right) . \tag{2.66b}$$

Deviations from L_0 induced for example by magnon excitations or finite temperature are described by

$$\delta L \quad = \quad \frac{1}{N} \sum_{\vec{k}} \left[\frac{A_{\vec{k}}}{\omega_{\vec{k}}} \langle n_{\vec{k}} \rangle - \frac{B_{\vec{k}}}{\omega_{\vec{k}}} \mathrm{Re} \langle b^\dagger_{\vec{k}} b^\dagger_{-\vec{k}} \rangle \right] . \tag{2.67}$$

In the following, we will mainly concentrate on the low temperature regime ($T = 0$), where magnon excitations induced by the laser pulses are the dominant effect, and neglect any temperature dependence.

Note that we obtain only reliable results for $|\delta L| < L$ since $L = S$ is the upper bound. The change of the sublattice magnetization has to be significantly smaller than the constant contribution L_0. In addition, the linear spin wave theory is also only applicable for small magnon occupations, which leads also to small δL.

The resulting sublattice magnetizations for two different driving frequencies $\omega_0 = 30\,\mathrm{ps}^{-1}$ (blue solid line) and $\omega_0 = 100\,\mathrm{ps}^{-1}$ (red curve) are shown in Fig. 2.6. Both curves show osciallations with ω_0. For $\omega_0 = 30\,\mathrm{ps}^{-1}$, we observe an exponentially decreasing amplitude illustrated as blue dashed line. The amplitude for $\omega_0 = 100\,\mathrm{ps}^{-1}$ firstly increases and then decreases. The limit value of δL is clearly finite for $\omega_0 = 100\,\mathrm{ps}^{-1}$, while this effect is not visible for $\omega_0 = 30\,\mathrm{ps}^{-1}$ because the limit value of this case is too small to be captured in this plot.

To understand the change of the sublattice magnetization, we split it into two contributions: $\delta L = u(t) + v(t)$ with the magnon occupation

$$u(t) = \sum_{\vec{k}} \frac{A_{\vec{k}}}{\omega_{\vec{k}}} \langle n_{\vec{k}} \rangle \tag{2.68}$$

and the Bogoliubov term

$$v(t) = -\sum_{\vec{k}} \frac{B_{\vec{k}}}{\omega_{\vec{k}}} \mathrm{Re} \langle b^\dagger_{\vec{k}} b^\dagger_{-\vec{k}} \rangle . \tag{2.69}$$

For $\omega_0 = 100\,\mathrm{ps}^{-1}$, we illustrate the magnon occupation $u(t)$ as green curve and the Bogoliubov contribution $v(t)$ as orange line in Fig. 2.6. The magnon occupation grows and reaches a finite value, which determines $L(t \to \infty)$, while the Bogoliubov term provides the oscillatory behavior.

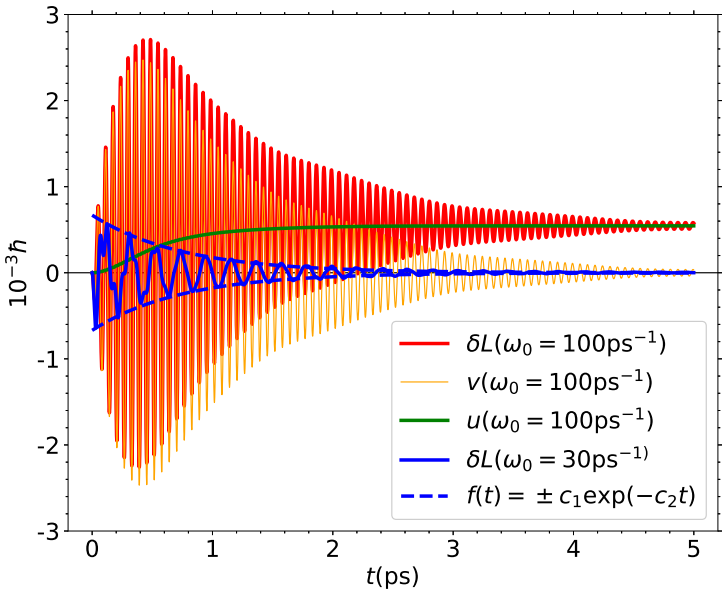

Figure 2.6: The change of the sublattice magnetization in dependence on the time for $\omega_0 = 30\,\text{ps}^{-1}$ and $\omega_0 = 100\,\text{ps}^{-1}$. For $\omega_0 = 30\,\text{ps}^{-1}$, an envelope $f(t) = \pm c_1 \exp(-c_2 t)$ of the amplitude is fitted with $c_1 = (6.7 \pm 0.1) \times 10^{-4}, c_2 = (1.34 \pm 0.05)\,\text{ps}^{-1}$. For $\omega_0 = 100\,\text{ps}^{-1}$, the magnon occupation $u(t)$ and the Bogoliubov term $v(t)$ are depicted. Parameters: $M = 100, \kappa = 0.01, \gamma = 1.0\,\text{ps}^{-1}, \gamma_r = 0$. Figure taken from Ref. [36].

Effect of the driving strength a_0

The driving strength should depend on the laser intensity applied in the experiment. However, since the exact relation is not known, we calculate the effect of different driving amplitudes a_0 in a reasonable range of $\max|\delta J_3(t)|/J_3^{(0)} \leq 0.1$ in this section.

Figure 2.7 shows the numerical results for different values of the relative driving strengths κ_3. As red dots the maximum value $\max|\delta L|$ is illustrated for $\omega = 50\,\text{ps}^{-1}$, as green dots for $\omega = 100\,\text{ps}^{-1}$. The data for $\omega = 50\,\text{ps}^{-1}$ follows a linear development

$$f(\kappa) = c\kappa \tag{2.70}$$

with $c = 0.0909 \pm 0.0004$ illustrated as blue line. In contrast, we can describe the

data points for $\omega = 100\,\mathrm{ps}^{-1}$ with a parabolic fit

$$f(\kappa) = c_1\kappa + c_2\kappa^2 \tag{2.71}$$

with $c_1 = 3.5 \pm 0.1, c_2 = 0.225 \pm 0.006$ shown as cyan line.

These different behaviors occur due to the different contributions in δL. The magnon occupation is quadratic in a_0 (respectively in κ, too), while the Bogoliubov terms depend linearly on a_0 as shown in Sec. 2.4.1. It is relevant if $u(t)$ or $v(t)$ dominates δL. Far away from a maximum of the magnon density of states (e.g. for $\omega = 50\,\mathrm{ps}^{-1}$), only a few modes are driven resonantly, and therefore, the Bogoliubov contribution is most important, which leads to the linear relation. In contrast, when a lot of modes fulfill (approximately) the resonance condition $\omega_0 = 2\omega_{\vec{k}}$, as for $\omega = 100\,\mathrm{ps}^{-1}$, the magnon occupation is large, and its contribution to the change of the sublattice magnetization is so significant that the a_0^2-relation is reflected in δL.

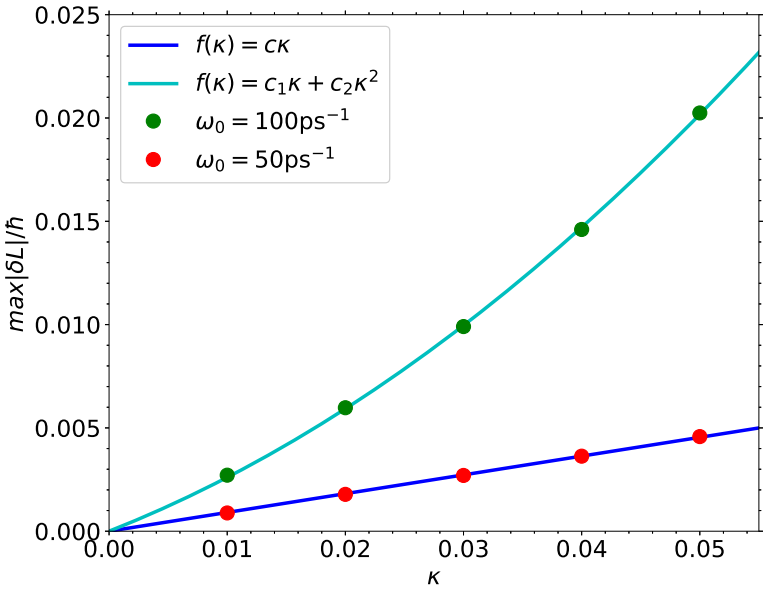

Figure 2.7: The maximum absolute value of the change of the sublattice magnetization $\max|\delta L|$ in dependence of the relative strength of driving κ. It follows a linear or quadratic development depending on how many $\vec{k}$ modes are driven (approximately) resonantly. Parameters: $\gamma = 1.0\,\mathrm{ps}^{-1}, M = 100, c = 0.0909 \pm 0.0004, c_1 = 3.5 \pm 0.1, c_2 = 0.225 \pm 0.006$. Figure taken from Ref. [36].

Effect of the damping γ

The damping γ of the driving term causes an exponential decrease of the amplitude of the sublattice magnetization δL, which is understood by our analytical calculations. This decrease is for example visible as blue dashed line in Fig. 2.6. We fit the maxima of δL for different γ with

$$e(t) = c\exp(-b(\gamma)t) \tag{2.72}$$

to extract a γ dependent decay rate $b(\gamma)$. Figure 2.8 shows the results as red dots. For small γ, we see the expected relation $b \approx \gamma$.

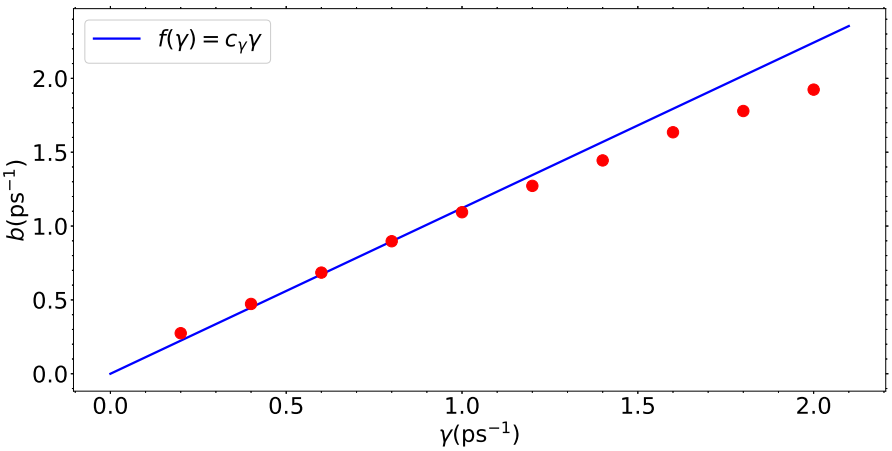

Figure 2.8: The decrease of the envelope of the sublattice magnetization depends on the damping γ of the driving. For small damping, the envelope fit parameter b matches the damping γ. For larger damping, b is smaller than γ. Parameters: $M = 100, \kappa = 0.005, \omega_0 = 30\,\mathrm{ps}^{-1}$. Figure taken from Ref. [36].

To understand the underlying mechanism, we should think of $1/\gamma$ as time scale on which the driving acts. Choosing a large damping γ means that the driving is effectively applied on a short timescale, and vice versa for small γ. The limit of $\gamma = 0$ describes the case when the driving is not damped at all, while $\gamma \to \infty$ is translated to $a(t) \to 0$ for all times t. While the driving acts on the system, the driving frequency determines the frequency of the magnon dynamics.

For larger values of γ, b is smaller than γ since we expect b to saturate for $\gamma \to \infty$. The limit value $b_\infty = \lim_{\gamma\to\infty}(b(\gamma))$ should be of the order of $2\omega_{\max}$.

Furthermore, we have to consider the case of vanished driving. The magnon occupation does not grow any more; the Bogoliubov terms $v_{\vec{k}}$ and $w_{\vec{k}}$ oscillate according their eigenfrequencies $\omega_{\vec{k}}$ as shown in Eqs. (2.24) and (2.25). As a result, the sum over all $\vec{k}$ modes dephases since each $\vec{k}$ mode has its own eigenfrequency according to the density of states.

All in all, the Bogoliubov contributions sum up to a larger value when they are coherently driven. When the driving vanishes, the dephasing effect becomes important.

To quantify the effect of γ, we introduce

$$L^2_{\text{quad}} := \int_0^\infty (\delta L(t) - \delta L_\infty)^2 dt. \tag{2.73}$$

It measures in particular the Bogoliubov part since the limit δL_∞ determined by the magnon occupation is substracted. Due to the integral, L^2_{quad} is also sensitive to the duration of the osillation.

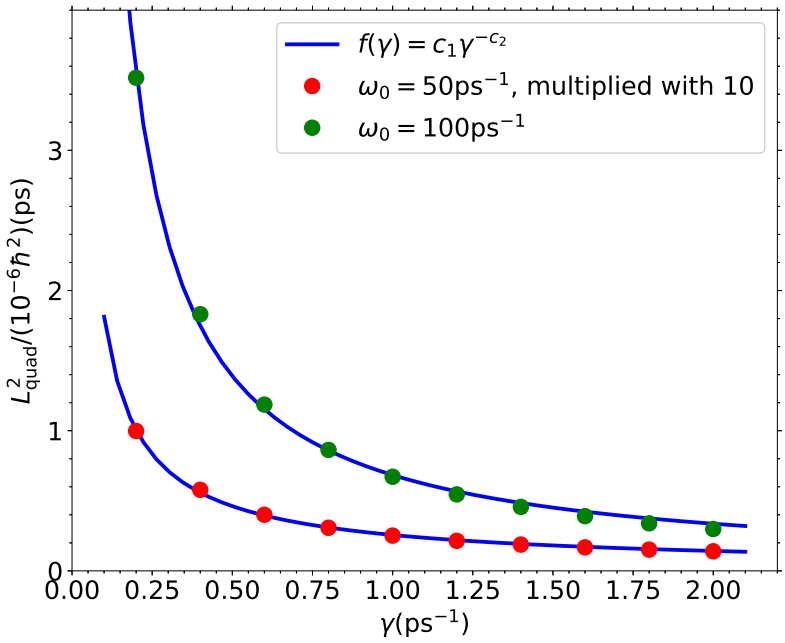

Figure 2.9: The integral L^2_{quad} of the square of the sublattice magnetization decreases approximately with $1/\gamma$. The exact fitting parameters are $c_2 = 0.850 \pm 0.009$ for $\omega_0 = 50\,\text{ps}^{-1}$ and $c_2 = 1.02 \pm 0.01$ for $\omega_0 = 100\,\text{ps}^{-1}$. Parameters: $M = 100, \kappa = 0.005$. Figure taken from Ref. [36].

Figure 2.9 shows L^2_{quad} in dependence of the damping γ for $\omega_0 = 50\,\text{ps}^{-1}$ (red dots) and $\omega_0 = 100\,\text{ps}^{-1}$ (green dots). For better visibility, L^2_{quad} for $\omega_0 = 50\,\text{ps}^{-1}$ is multiplied by 10. We fit the data with

$$f(\gamma) = c_1 \gamma^{c_2} \tag{2.74}$$

and illustrate these results as blue line. The fitting parameters are $c_2 = 0.850 \pm 0.009$ for $\omega_0 = 50\,\text{ps}^{-1}$ and $c_2 = 1.02 \pm 0.01$ for $\omega_0 = 100\,\text{ps}^{-1}$. The parameter $c_2 \approx 1$ reveals that the effective application time $1/\gamma$ has a significant effect on L^2_{quad}. Our fit shows that the energy brought into the system grows linearly with the time the driving is applied.

In contrast, the effect of γ on the maximum value $\max|\delta L|$ is rather small as depicted in Fig. 2.10. Again, we show the results for $\omega_0 = 50\,\text{ps}^{-1}$ (multiplied by 2 for better visibility, red dots) and $\omega_0 = 100\,\text{ps}^{-1}$ (green dots). For $\omega_0 = 50\,\text{ps}^{-1}$, the curve is almost horizontal, while it decreases for increasing γ for $\omega_0 = 100\,\text{ps}^{-1}$. In the consider

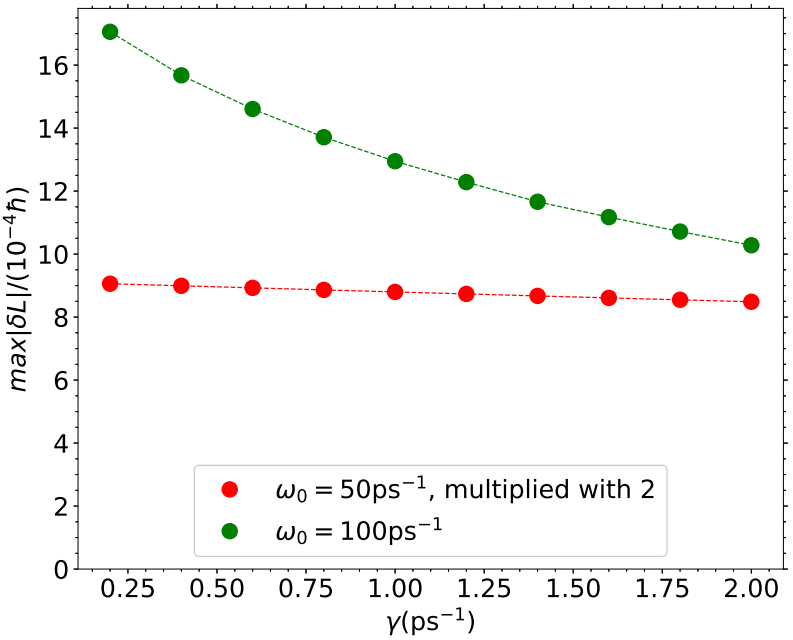

Figure 2.10: The maximum value of δL depends only barely on the damping γ. The effect is stronger for $\omega = 100\,\text{ps}^{-1}$. Here the maximum amplitude is reached after a build-up phase, while the maximum amplitude for smaller driving frequencies appears near to $t = 0$. Near to $t = 0$, the damping plays a smaller role than for larger times. Parameters: $M = 100, \kappa = 0.005$. Figure taken from Ref. [36].

The damping effects the time scale of decrease but not the prefactor of the envelope. The position of the maximum influences if this effect is clearly visible in $\max|\delta L|$. Since the maximum for $\omega_0 = 100\,\mathrm{ps}^{-1}$ is reached significantly later than for $\omega_0 = 50\,\mathrm{ps}^{-1}$ (c. f. Fig. 2.6), a dependence of γ on $\max|\delta L|$ is observable.

Effect of the driving frequency ω_0

To analyze the effect of the driving frequency, we fix the driving amplitude a_0 and the damping γ, and we calculate the maximum absolute value of the change of the sublattice magnetization $\max|\delta L|$ as well as the limit

$$\delta L(t \to \infty) = \lim_{t\to\infty} \delta L(t). \tag{2.75}$$

We neglect the relaxation ($\gamma_r = 0$) in these calculations. Figure 2.11 shows the results. The maximum value $\max|\delta L|$ (red curve) and the offset $\delta L(t \to \infty)$ (magenta curve) have a maximum near to $\omega_0 = 100\,\mathrm{ps}^{-1}$. For comparison, the rescaled magnon density of states $\rho(\omega_0/2)$ is plotted as blue curve. The maxima of $\max|\delta L|$ and $\delta L(t \to \infty)$ appear approximately at the maxima of $\rho(\omega_0/2)$.

When the resonance condition $\omega_0 = 2\omega$ is (approximately) fulfilled for a $\vec{k}$ point, the amplitude of $v_{\vec{k}}$ and the magnon occupation $u_{\vec{k}}$ become large. For large density of states, a lot of $\vec{k}$ points are driven resonantly, and therefore, $\max|\delta L|$ reaches a maximum due to the Bogoliubov term and $\delta L(t \to \infty)$ because of the magnon occupation.

Time evolution of the energy

By driving the system, we change the energy of the spin system. We calculate the amount of energy as temporal evolution and in dependence of the driving strength a_0.

We define the energy per spin as

$$E(t) \;=\; \frac{1}{N}\left(\langle H(t)\rangle - J_1 S(E_d + \Delta E)\right). \tag{2.76}$$

By substracting the equilibrium expection value $\langle H_0\rangle = J_1 S(E_d + \Delta E)$, we focus only on the non-equilibrium energy contributions induced by the driving.

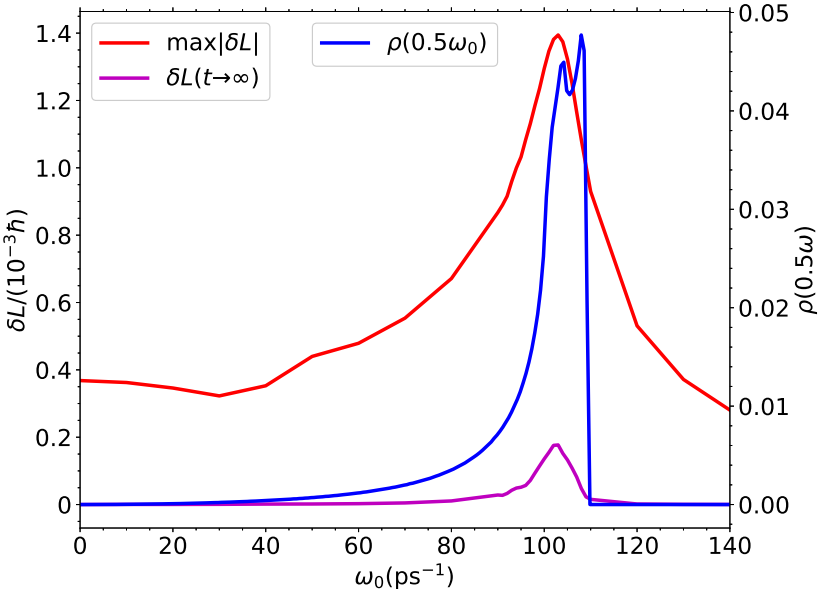

Figure 2.11: The maximum value $\max|\delta L|$ and the offset $\delta L(t \to \infty)$ compared to the rescaled density of states $\rho(\omega_0/2)$. Both show a similar behavior due to the resonance condition $\omega_0 = 2\omega$. Parameters: $M = 100, \kappa = 0.01, \gamma = 1\,\mathrm{ps}^{-1}$. Figure taken from Ref. [36].

Figure 2.12 shows the time evolution of the energy. The energy $E(t)$ oscillates, which is in this plot only visible for $\omega_0 = 30\,\mathrm{ps}^{-1}$ and short times. In average, the energy increases until it reaches a limit value

$$E(t \to \infty) = \lim_{t\to\infty} E(t), \tag{2.77}$$

when the driving has effectively vanished. Numerically, the saturation value $E(t \to \infty)$ can be determined by picking the energy for a large $t \ll 1/\gamma$. By calculating a so called "running average"

$$\bar{E}(t) = \frac{1}{T_0}\int_{t-T_0/2}^{t+T_0/2} E(t')dt' \tag{2.78}$$

with $T_0 = 2\pi/\omega_0$, we focus on the slow development, and we get more precise results for $E(t \to \infty)$. When we average over one period, the oscillations with ω_0 vanish and we obtain more accurate results for $\bar{E}(t)$.

For the same driving strength, the saturation value is larger for $\omega_0 = 100\,\mathrm{ps}^{-1}$ than for $\omega_0 = 30\,\mathrm{ps}^{-1}$ because more $\vec{k}$ modes are driven (approximately) resonantly for

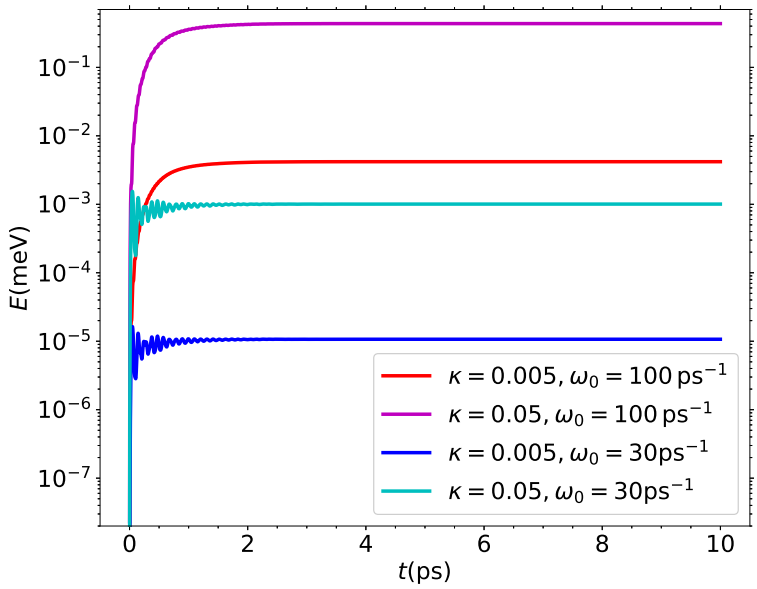

Figure 2.12: The energy of the system increases and reaches a finite value, when the driving has vanished. Oscillations with ω_0 appear, but due to their small amplitude, their effect is in this figure only visible for $\omega_0 = 30\,\mathrm{ps}^{-1}$. The amplitude is larger, when the driving is stronger (large κ) and when the driving frequency matches a lot of magnon eigenfrquencies ($\omega_0 = 100\,\mathrm{ps}^{-1}$ corresponds to large magnon DOS). Parameter: $M = 100, \gamma_r = 0$. Figure taken from Ref. [36].

$\omega_0 = 100\,\mathrm{ps}^{-1}$. If we compare the red and the cyan curve, we see that this effect compensates even a ten times larger driving strength.

For the same driving frequency, the saturation value is larger if the driving strength κ is larger, which can be seen for $\kappa = 0.005$ in comparison to $\kappa = 0.05$. To analyze this effect quantitatively, the saturation value is calculated for different κ, depicted in Fig. 2.13.

On a logarithmic scale, $E(t \to \infty)$ depends linearly on the driving strength κ. Via analyzing the gradient, we see that there is a quadratic relation:

$$f(\kappa) = c_{\omega_0}\kappa^2. \tag{2.79}$$

While the prefactor c_{ω_0} depends on the driving frequency and is larger for $\omega_0 = 100\,\mathrm{ps}^{-1}$ than for $\omega_0 = 30\,\mathrm{ps}^{-1}$ as already indicated in Fig. 2.12, the exponent is independent of ω_0.

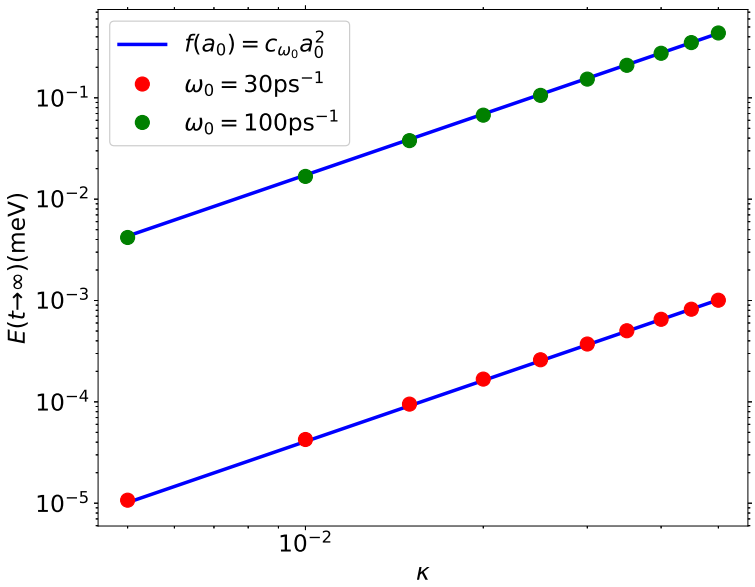

Figure 2.13: The energy depends quadratically on the strength of driving κ. The functional dependence holds for both shown driving frequencies, but the absolute values differs due to the magnon DOS. Parameters: $M = 100, \gamma = 1.0\,\text{ps}^{-1}$. Figure taken from Ref. [36].

This finding is consistent with an classical harmonic oscillator, which has an energy absorption proportional to the square of the driving amplitude. Another approach would be Fermi's Golden Rule, which predicts the same relation.

But we can explain this finding also with our analytical approximations. The limits for $t \to \infty$ are determined by the magnon occupations. Since we observe a quadratic relation between $u_{\vec{k}}$ and κ, we expect the same dependence between E and κ.

2.4.3 Making contact to experiments

In order to apply our modeling to experiments, we firstly use realistic parameters, and we secondly investigate the effect of considering another Heisenberg coupling time-dependent.

Calculations with experimental parameters

Several parameters defining our model can be determined experimentally. In this section, we refer always to the experiments performed by Bossini et al. [23]. The driving frequency is given by the phonon frequency: $\omega_0 = 33.6\,\mathrm{ps}^{-1}$. The decay rates can be estimated by fitting the envelope of the experimental data: $\gamma = 0.055\,\mathrm{ps}^{-1}$ and $\gamma_r = 3.9 \times 10^{-3}\,\mathrm{ps}^{-1}$. However, the relation between the experimental setup and the strength of driving in our model is unknown so far. We assume that the higher the laser intensity the larger the strength of driving. But the exact conversion remains unclear. In consequence, we assume that the couplings J_i should not change more than 10 %: $|\delta J_i/J_i| < 0.1$, and we calculate the change of the sublattice magnetization for different $a_{0,i}$ to cover the case of small and of larger driving.

Figure 2.14 shows the change of the sublattice magnetization for experimentally reasonable parameters. In panel (a), the short dynamics are illustrated. The coherent oscillations with ω_0, as well as the exponential decrease of the amplitude are visible. The panels 2.14(b)-(d) focus on the long time dynamics. Since the decay rates in the experiments are much smaller than the decay rates used in the previous sections, we need to calculate a longer time interval, which results in a higher number of needed discretization steps N. However, the curves show a similar development, such as, the exponentially decreasing amplitude. The magnon occupation $u(t)$ in shown in Fig. 2.14(c). It increases on a time scale of $1/\gamma$ and then decays exponentially due to the relaxation caused by γ_r. Note that the absolute value of $u(t)$ is small compared to $|\delta L|$. Furthermore, the magnon occupation and consequently also δL vanish completely for $t \to \infty$ because we include a relaxation into the equations.

While panels 2.14(a)-(c) shows results for $\kappa = 0.01$, panel (d) depicts the change of the sublattice magnetization for a large driving amplitude $\kappa = 0.06$. The contribution of the magnon occupation is plotted as magenta line. In contrast to the parameter sets considered before, we can clearly see that the magnon occupation has now a significant impact on δL. Because of the quadratic dependence of κ on $u(t)$, the magnon occupation becomes only clearly visible for larger κ.

Modulating other exchange parameters

In the previous sections, we assumed that the Heisenberg coupling J_3 acquires a time-dependent contribution, which is reasonable due to the indirect coupling between the Mn ions via a Te ion. Nevertheless, J_1 and J_2 can in principle also be modulated by optical phonons [23].

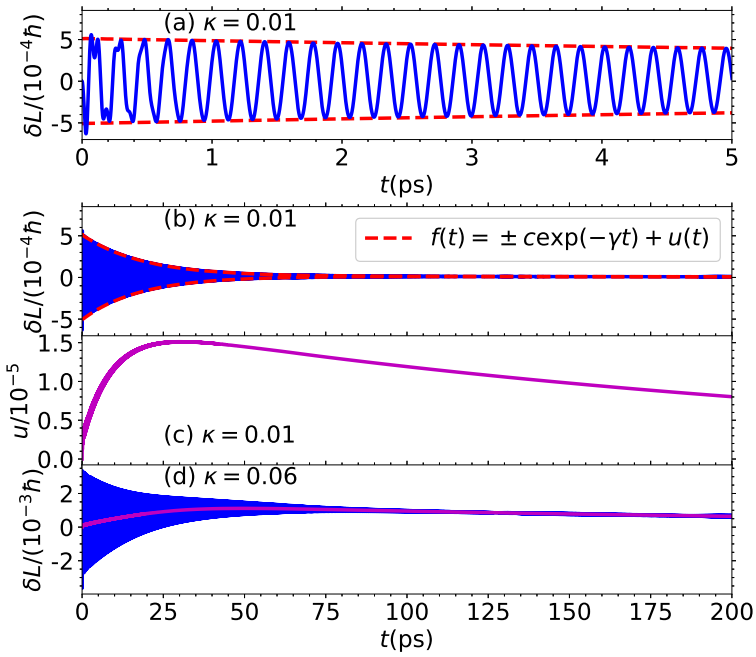

Figure 2.14: The change of the sublattice magnetization for experimental parameters. Panel (a) focuses on the short time dynamics while panels (b)-(d) show a longer time interval. In addition to the change of the sublattice magnetization (blue solid lines) and its envelope (red dash lines), panels (c) and (d) also depict the magnon occupation part as magenta solid lines. Panels (a)-(c) show results for $\kappa = 0.1$, while panel (d) considers a larger driving with $\kappa = 0.06$. Parameters: $\omega_0 = 33.6\,\mathrm{ps}^{-1}, \gamma = 0.055\,\mathrm{ps}^{-1}, \gamma_r = 3.9 \times 10^{-3}\,\mathrm{ps}^{-1}, M = 2200$. Figure taken from Ref. [36].

The general structure of the differential equations remains unchanged while the concrete values of $\alpha_{\vec{k}}$ and $\beta_{\vec{k}}$ in the expansion of $X(t)$ in the magnon operators (Eq. (2.20)) need to be adapted. If we assume a driving via $\delta J_1(t)$, we obtain

$$\alpha_{\vec{k}} = \frac{A_{\vec{k}}}{\omega_{\vec{k}}} \left(2 - 2\frac{B_{\vec{k}}}{A_{\vec{k}}} \cos(k_3)\right) \tag{2.80a}$$

$$\beta_{\vec{k}} = \frac{A_{\vec{k}}}{\omega_{\vec{k}}} \left(-2\frac{B_{\vec{k}}}{A_{\vec{k}}} + 2\cos(k_3)\right), \tag{2.80b}$$

and

$$\alpha_{\vec{k}} = \frac{A_{\vec{k}}}{\omega_{\vec{k}}} \left(6 - 2\frac{B_{\vec{k}}}{A_{\vec{k}}} \gamma_\Delta(\vec{k}) \right) \tag{2.81a}$$

$$\beta_{\vec{k}} = \frac{A_{\vec{k}}}{\omega_{\vec{k}}} \left(-6\frac{B_{\vec{k}}}{A_{\vec{k}}} + 2\gamma_\Delta(\vec{k}) \right). \tag{2.81b}$$

when we consider a time-dependent $\delta J_2(t)$.

Figure 2.15 shows an overview of the change of the sublattice magnetization for time-dependent (a) $J_1(t)$, (b) $J_2(t)$, and (c) $J_3(t)$, all with a relative driving amplitude of $\kappa_i = 0.01$. All curves show coherent oscillations with the driving frequency $\omega_0 = 30\,\mathrm{ps}^{-1}$. We chose a damping of $\gamma = 1.0\,\mathrm{ps}^{-1}$ and neglected relaxation ($\gamma_r = 0$).

Note the different scales of the y axes. The amplitudes of curves in panel 2.15(a) and (c) are similar while curve of panel (b) has a significantly smaller amplitude. Two effects explain this observation. Firstly, the relative change $\kappa_i = \max|\delta J_i|/|J_i^{(0)}|$ is equal in the three cases. As a result, the absolute value of the change δJ_i depends on the coupling in equilibrium $J_i^{(0)}$. Secondly, the number of neighbors coupling by J_i enters into the overall driving strength. Taking into account both effects, the effective driving via $\delta J_3(t)$ is comparable strong as via $\delta J_1(t)$, although $J_1^{(0)}$ is more the seven times larger than $J_1^{(0)}$ because the number of neighbors coupling via J_3 is six times larger. In contrast, $J_2^{(0)}$ is the smallest coupling considered, which cannot be compensated by the number of belonging neighbors.

Furthermore, the sign of the curve in Fig. 2.15(a) has an opposite sign than the curves in panel 2.15(b) and (c). The product $\beta_{\vec{k}} B_{\vec{k}}$ determines this global sign in Eq. (2.31). For the considered parameter set, this yields to positve sign for δJ_1 and negative sign for δJ_2 and δJ_3.

To this end, the sublattice magnetizations are very similar because of the same analytic structure. As a result, the qualitative effects of the driving parameters onto the sublattice magnetization should be also the same if we consider a time-dependent J_1 or J_2 instead of J_3. Therefore, the investigation presented in previous sections covers the essential physical behaviour of the change of the sublattice magnetization.

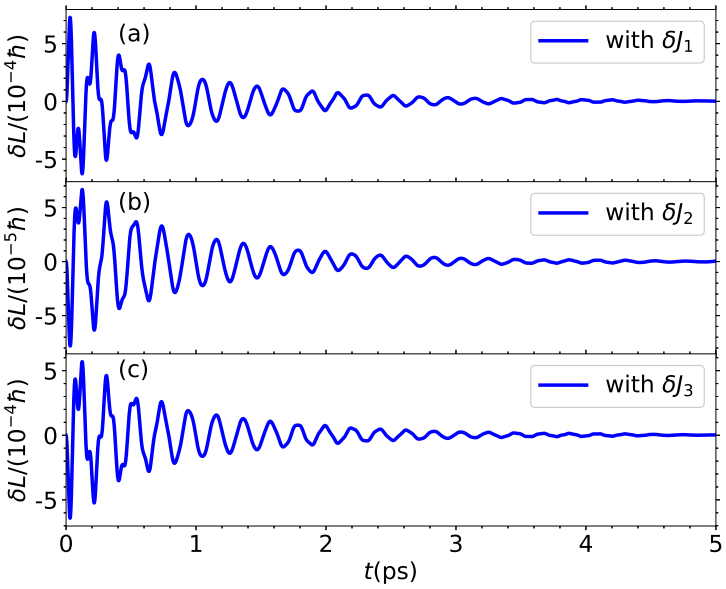

Figure 2.15: The change of the sublattice magnetization shows quantitatively the same behavior no matter which Heisenberg coupling is time-dependent. Panel (a) depicts a modulated J_1 while panel (b) shows it for J_2, and panel (c) for J_3. In each case, the relative change of the amplitude is $\kappa_i = 0.01$. Parameters: $M = 200, \omega_0 = 30\,\mathrm{ps}^{-1}, \gamma = 1.0\,\mathrm{ps}^{-1}, \gamma_r = 0$. Figure taken from Ref. [36].

2.5 Summary

We investigated the magnon excitations induced by a time-dependent Heisenberg coupling modeling the magnetic structure of α-MnTe with a Heisenberg Hamiltonian subject to an external driving field. Focussing on a single mode, we understand the dynamics within our analytical approximations. It depends on the strength of driving, the driving frequency, the damping, and the eigenfrequency of the $\vec{k}$ point.

The sublattice magnetization compromises a sum over all $\vec{k}$ modes. It increases with increasing driving strengths, and its envelope decreases exponentially with the damping parameter of the driving. We understand the relation between the driving frequency and the eigenfrequencies of the $\vec{k}$ modes by comparing with the magnon density of states. The amplitude of the sublattice magnetization is proportional to the magnon density of states $\rho(\omega_0/2)$. The factor of 2 is due to the resonance condition $\omega_0 = 2\omega_{\vec{k}}$.

To describe relaxation, which is not included in a microscopic way in our model, we added a phenomenological relaxation term. As a result, the sublattice magnetization vanishes for large times and exhibits two different exponential decays. If the damping and the phenomenological decay parameters act on different time scales, their effects can be seen in different time intervals.

We were able to calculate the change of the sublattice magnetization for realistic parameters. Because of the small damping, the effect of an increasing magnon occupation is more pronounced than in previous calculations. However, the absolute contribution to the change of the sublattice magnetization depends a lot on the strength of driving.

We also included the influence of the change of the other Heisenberg couplings J_1 and J_2 in our analysis. The general effect on the sublattice magnetization is the same as for time-dependent J_3. Only the absolute values change since we consider always relative changes and the equilibrium values of the coupling parameters as well as the belonging number of nearest neighbors differ. Due to the similar form of differential equations and the resulting sublattice magnetizations, we focussed on the time-dependent Heisenberg coupling J_3 since it is the most likely to be changed by phonon oscillations because J_3 is mediated by the electron hopping process across a Te ion, whose relative distance to the Mn ions oscillates with the laser induced lattice vibrations.

Chapter 3

Electronic structure of α-MnTe

The electronic structure of α-MnTe has been already studied in the past (see for example Refs. [43–46]). The aim of this chapter is to give an overview over the main features and to provide a minimal tight-binding model that captures these essential electronic properties. This is the starting point for treating the $3d$ electrons as strongly correlated within a dynamical mean field theory approach.

The electronic configurations of atomic manganese and tellure are:

$$\text{Mn: } [\text{Ar}]3d^5\ 4s^2, \quad \text{Te: } [\text{Kr}]4d^{10}5s^2 5p^4. \tag{3.1}$$

The atomic manganese has in addition to the argon configuration partially filled $3d$ orbitals and a fully occupied $4s$ orbital. A tellure atom has completely filled $4d$ and $5s$ orbitals as well as partially occupied $5p$ orbitals in addition to the krypton configuration. In α-MnTe, the elements appear as ions: Mn^{2+} and Te^{2-}. In this case, in contrast to the atomic configuration, the $4s$ orbitals of Mn^{2+} are unoccupied, and the $5p$ orbitals of Te^{2-} are completely filled. This ignores hybridization effects and band formation which will be taken into account below.

For our investigations, the band structure near to the Fermi energy, which implies the valence and the conduction band, is most important. For the valence band, the fully occupied Te $5p$ orbitals are a promising candidate. To form a conduction band, orbitals have to be unoccupied or only partially filled, which applies to the Mn $3d$ and $4s$ orbitals.

To model α-MnTe with a tight-binding Hamiltonian, we have to determine the hopping parameters between the considered orbitals. After introducing the general form of a multi-orbital tight-binding Hamiltonian in Sec. 3.1, we consider the density functional theory in Sec. 3.2 to determine the model's parameters.

3.1 Tight-binding Hamiltonian

The tight-binding approach, which is explained in many solid state textbooks, such as [47, 48], considers hopping between sites,

$$H = \sum_{\langle i,j \rangle} (t_{ij} c_i^\dagger c_j + \text{h. c.}), \tag{3.2}$$

where $\langle ij \rangle$ indicating that the sites are neighboring. This Hamiltonian is diagonalized by applying the Fourier transformation

$$c_m = \frac{1}{N} \sum_{\vec{k}} \exp(-i\vec{k}\vec{l}_m) c_{\vec{k}} \tag{3.3}$$

with the position $\vec{l}_m$ of site m. The sum runs over the whole first Brillouin zone. We obtain

$$H = \sum_{\vec{k}} \epsilon(\vec{k}) c_{\vec{k}}^\dagger c_{\vec{k}}. \tag{3.4}$$

The dispersion $\epsilon(\vec{k})$ describes the energy of an electron in dependence of $\vec{k}$. The concrete form of $\epsilon(\vec{k})$ is determined by the hoppings t_{ij} in real-space and the crystal structure, which enters in the positions $\vec{l}_m$.

3.1.1 Multi-orbital tight-binding Hamiltonian

In general, a unit cell can consist of several atoms, and these atoms can have several orbitals that should be taken into account. In this case, we need to extend the previous Hamiltonian. To understand the extension, we first consider both cases seperately and second bring them together.

Unit cell with several atoms

If a basis contains more than one atom, we need to distinguish on which atom the operator act: for example, the operator $c_{A,}^\dagger$ creates an electron on atom A while c_B annhilates an electron at atom B. The creation and annihaltion operators for a unit cell consisting of N atoms are summarized in the vectors:

$$\vec{c}_i{}^\dagger = (c_{A,i}^\dagger, c_{B,i}^\dagger, ..., c_{N,i}^\dagger)^T, \tag{3.5a}$$

$$\vec{c}_j = (c_{A,j}, c_{B,j}, ..., c_{N,j})^T. \tag{3.5b}$$

The hopping parameter t_{ij} becomes a matrix, and we can write the Hamiltonian as follows:

$$H = \sum_{\langle i,j \rangle} \big((\vec{c}_i^{\,\dagger})^T \, \underline{\underline{t}} \, \vec{c}_j + \text{ h. c.} \big). \tag{3.6}$$

If electrons can only hopp to atoms of other kind, e.g. from atom A to B, but not from one A atom to another A atom, the diagonal matrix elements are the on-site energies $t_{LL} = \epsilon_L$ of atom L. In contrast, the off-diagonal elements describe the actual hopping.

The Hamiltonian is again transformed into $\vec{k}$ space. The Fourier transformation (3.3) leads to terms that include the position of the atoms. By combining these terms with the corresponding hopping element in real-space, the transformed hopping elements obtain an exponential factor $\exp(i\vec{k}(\vec{l}_m - \vec{l}_n))$ containing the difference of the atoms' positions $\vec{l}_m$ and $\vec{l}_n$. If the positions are the same, the exponential term is 1, which means that the hopping is $\vec{k}$ independent and describes the on-site energy.

Atoms with several orbitals

Similar to the tight-binding Hamiltonian in a system with several atoms per unit cell, including several orbitals leads to a matrix formulation. Assuming one atom per unit cell with n orbitals enables us to define the vector

$$\vec{c}_i^{\,\dagger} = (c_{a,i}^\dagger, c_{b,i}^\dagger, ..., c_{n,i}^\dagger)^T. \tag{3.7}$$

with operators acting on the orbitals $a, b, ..., n$ and a Hamiltonian equivalent to Eq. (3.6). The diagonal elements describe the orbital energy $t_{ll} = \epsilon_l$ of the orbital l.

Basis with several atoms possessing multiple orbitals

The Hamiltonian for a basis with more than one atom is very similar to the Hamiltonian of a one-atom basis with several orbitals. The general form of the Hamiltonian (3.6) does not change. Only the definition of the vector $\vec{c}_{\vec{k}}$ and the entries of $\underline{\underline{t}}$ change. Combining both approaches leads to a vector

$$\vec{c}_i^{\,\dagger} = (c_{Aa_A,i}^\dagger, c_{Ab_A,i}^\dagger, ..., c_{An_A,i}^\dagger, c_{Ba_B,i}^\dagger, ..., c_{Nn_N,i}^\dagger)^T. \tag{3.8}$$

The basis has N atoms: $A, B, ..., N$, and the L-th atom has n_L orbitals: $a_L, b_L, ..., n_L$. The length of the vector is consequently:

$$\lambda = \sum_{L=1}^{N} \sum_{l=1}^{n_L} 1 \tag{3.9}$$

with $L = 1$ considering atom A, as well as $l = 2$ referring to orbital b, and so on. The matrix $\underline{\underline{t}}$ has the dimension $\lambda \times \lambda$, which leads to λ bands.

The diagonal elements $t_{Ll,Ll} = \epsilon_{Ll}$ describe the orbital energy of orbital l at atom L. Note that one atom can possess different orbital energies. Typically orbitals of different kinds $(s, p, d, ...)$ differ in their energies. In addition, orbitals of the same kind can be split for example by a crystal field. To this end, we arrive at the bilinear form:

$$H = \sum_{\vec{k}} \vec{c}^{\dagger}_{\vec{k}} \underline{\underline{t}}(\vec{k}) \vec{c}_{\vec{k}}. \tag{3.10}$$

Multi-orbital tight-binding Hamiltonian for α-MnTe

After we have established the generic form of a multi-orbital tight-binding Hamiltonian, we have to adjust it to the considered material α-MnTe. Therefore, we have to ask two questions: How many atoms are in the unit cell? Which orbitals do we have to take into account? While the first question is easy to answer, the second one is more challenging.

The unit cell for the magnetically ordered phase of α-MnTe consists of two Mn and two Te ion. We have two take into account in total these four atoms.

A naive approach answering the second questions would be to include all orbitals. As a result, we would not miss any important effects. But a lot of the orbitals lie very low in energy – far below the Fermi energy – and are therefore not relevant for the physics we are interested in. Additionally, dealing with a large Hamilton matrix would require an enormous numerical effort.

In consequence, we have to choose an appropriate set of orbitals. It should be as small as possible, but has to describe the relevant features of α-MnTe. Concerning the electronic structure, it must be sufficient to obtain a band gap as characteristic of a semiconductor. Therefore, we need a valence and a conduction band.

Considering the approach of Masek et al., for quantitatively good results, the $5s$,p valence orbitals of Te and the $4s$,p and $3d$ orbitals of Mn have to be included [44].

In a next step, we have to specify the matrix elements of $\underline{\underline{t}}$. For this purpose, we use the wanniernization of density functional theory results in Sec. 3.2.

3.1.2 Calculating the band structure

The electronic band structure is calculated by diagonalization of $\underline{\underline{t}}(\vec{k})$: The ith eigenvalue determines $\epsilon_{\vec{k},i}$ of the ith band, and the eigenvectors the mixing of the different orbitals in this band at the vector $\vec{k}$.

For plotting the results, we have to choose a path through the Brillouin zone. For each type of Brillouin zone, there is one path or a few common paths that cover the most important points in the zone. For the hexagonal structure of α-MnTe, we will use the path

$$\Gamma \to M \to K \to \Gamma \to A \to L \to H \to A. \tag{3.11}$$

While the Γ point lies in the middle of the Wigner-Seitz cell ($\vec{k} = (0,0,0)^T$), the other points lie on different points on the edge of the cell. Between the points, we define a certain amount of equidistant $\vec{k}$ points.

For example, to illustrate the bands that have Mn $3d$ character, we need to sum over all projections on Mn $3d$ orbitals and to plot the dispersion while encoding the total overlap as color of the line. In the following, a large overlap is always displayed with red and a vanishing overlap with blue.

3.1.3 Calculating the density of states

The total density of states is given by

$$\rho(\epsilon) = \lim_{\delta \to 0} \frac{1}{\pi} \mathrm{Im} \frac{1}{N_k} \sum_{\vec{k}i} G_{\vec{k},i}(\epsilon - i\delta) \tag{3.12}$$

with the Green's function $G_{\vec{k},i}(z)$. The sum has to cover the whole Brillouin zone, and the index i ensures that all eigenenergies are included, which is essential if we consider more than one band. To normalize the sum, we divide it by the number $N_{\vec{k}}$ of $\vec{k}$ points.

For a free particle with

$$G_{\vec{k},i}(z) = \frac{1}{z - \epsilon_{\vec{k}i}}, \tag{3.13}$$

the density of states is

$$\rho(\epsilon) = \frac{1}{N_k} \sum_{\vec{k}i} \delta(\epsilon_{\vec{k}i} - \epsilon). \tag{3.14}$$

Equation (3.14) can be implemented numerically straightforwardly [49]. The $\vec{k}$ point component can be distributed equidistant in each $\vec{k}$ direction. Note that the area should be chosen such that the Γ point lies in the middle [49]. The resulting energies need to be histogramed. The number of bins, or respectively the width of the bins, has to be adapted to the number of $\vec{k}$ points in order to obtain a reasonable result.

Starting with Eq. (3.12), it is also possible to calculate the density of states directly via the Green's function:

$$\rho(\epsilon) = \lim_{\delta \to 0} \frac{1}{\pi} \mathrm{Im} \frac{1}{N_k} \sum_{\vec{k}i} \frac{1}{\epsilon - \epsilon_{\vec{k}i} - i\delta}. \tag{3.15}$$

For energies equal to the eigenenergies, the denominator almost vanishes. Only the infinitesimal shift into the complex planes regularizes the fraction.

While both Eqs. (3.14) and (3.15) lead to the same results in the simple cases, only Eq. (3.12) is able to include a complex selfenergy, which can be useful in further calculations.

3.2 Density functional theory

The density functional theory (DFT) is an approach to calculate the ground state properties of a system. Although all obtained values, such as energies and states, are only approximations, the method allows us a deeper insight in many materials, which was honored with the Nobel prize in chemistry for Walter Kohn in 1998 [50]. In this section, we follow Ref. [51] to outline the method.

We start with the many-body Hamiltonian

$$H = \sum_{i=1}^{N} \frac{\vec{p}_i^2}{2m} + \frac{e^2}{2} \sum_{i \neq j} \frac{1}{|\vec{r}_i - \vec{r}_j|} + \sum_{i=1}^{N} V(\vec{r}_i). \tag{3.16}$$

The first term describes the kinetic energy of the electrons with momentum $\vec{p}_i$ and mass m. The Coulomb interaction between the electrons at position $\vec{r}_i$ and

$\vec{r}_j$ is captured in the second term. The potential $V(\vec{r}_i)$ of the third term includes interactions with the nuclei:

$$V(\vec{r}) = -\sum_I \frac{e^2 Z_I}{|\vec{r}_{\mathrm{nuc},I} - \vec{r}|} \tag{3.17}$$

with the position $\vec{r}_{\mathrm{nuc},I}$ of the nuclei and the nuclear charge numbers Z_I. Due to the Born-Oppenheimer approximation, the kinetic energy of the nuclei is not included in the Hamilitonian.

Defining the many-body Hamiltonian is straightforward, but solving this Hamilitonian exactly for a large number of electrons is generally not feasible. The DFT focuses on the ground state:

$$E_{\mathrm{GS}} = \min_\psi E[\psi] \text{ with } E[\psi] = \langle\psi|H|\psi\rangle \text{ and } \langle\psi|\psi\rangle = 1 \tag{3.18}$$

with the wavefunction $\psi(\vec{r}_1, \vec{r}_2, ..., \vec{r}_N)$.

The theorem of Hohenberg and Kohn [52] states that the ground state energy can be written as a functional of the electron density n:

$$E_{\mathrm{GS}} = \min_\psi E[\psi] \xrightarrow{\mathrm{DFT}} E_{\mathrm{GS}} = \min_n E[n] \tag{3.19}$$

with the constraint that the integral over the density is the total number of particles

$$N = \int n(\vec{r}) d^3r. \tag{3.20}$$

The Lagrangian

$$\Omega[n, \mu] = E[n] + \mu(N - \int n(\vec{r}) d^3r) \tag{3.21}$$

with the Lagrange multiplier μ is introduced to find the minimal energy under the given constraint concerning the particle number. This problem is simpler than solving the original Hamilitonian.

Writing the many-body Hamiltonian (3.16) as energy functional leads to:

$$E[n(\vec{r})] = \underbrace{\langle\psi|\sum_{i=1}^{N} \frac{\vec{p}_i^2}{2m}|\psi\rangle}_{T[n(\vec{r})]} + \underbrace{\langle\psi|\frac{e^2}{2}\sum_{i\neq j}\frac{1}{|\vec{r}_i - \vec{r}_j|}|\psi\rangle}_{U[n(\vec{r})]} + \underbrace{\langle\psi|\sum_{i=1}^{N} V(\vec{r}_i)|\psi\rangle}_{V[n(\vec{r})]}. \tag{3.22}$$

While the part including the ionic potential can be easily written with the charge density:

$$V[n(\vec{r})] = \int V(\vec{r})n(\vec{r})d\vec{r}, \tag{3.23}$$

a similar description for the kinetic contribution and the electron-electron interactions is more difficult to find. Both parts can be summarized as universal Hohenberg and Kohn functional:

$$F_{\mathrm{HK}} = E_{\mathrm{GS}}[\rho] - \int V(\vec{r})n(\vec{r})d\vec{r}. \tag{3.24}$$

In contrast to the ionic potentials, this functional does not depend on the specific system, which explains its universality. Finding suitable functionals for the electron-electron interaction and the kinetic energy turned out to be difficult. There are several approaches for the kinetic energy, for example assuming a non-interacting homogeneous electron gas or starting with the hydrogen atom. Although both attempts are correct in their specific case, they differ significantly, which means that neither of them is universally applicable.

Kohn and Sham suggest a different approach [53] to avoid finding a functional for the kinetic energy. The idea is that electronic states can be determined by one-body orbitals $\{\phi_i(\vec{r})\}$ with energies $\{\epsilon_i\}$ leading to the kinetic energy

$$T_0 = -\frac{1}{2}\sum_i \int \phi_i^*(\vec{r})\nabla^2\phi_i(\vec{r}) \text{ and } n(\vec{r}) = \sum_i |\phi_i(\vec{r})|^2. \tag{3.25}$$

The idea is to construct a system of a non-interacting electron gas in an effective external field V_{eff} such that it has the same charge density as the actual interacting system. In consquence, their Euler-Lagrange equations have to be equal:

$$\frac{\partial F_{\mathrm{HK}}[n]}{\partial n(\vec{r})} + V(\vec{r}) = \frac{\partial T_0}{\partial n(\vec{r})} + V_{\mathrm{eff}}(\vec{r}), \tag{3.26}$$

which determines the effective potential

$$V_{\mathrm{eff}}(\vec{r}) = V(\vec{r}) + \frac{\partial(F_{\mathrm{HK}}[n] - T_0)}{\partial n(\vec{r})}. \tag{3.27}$$

It can be rewritten

$$V_{\mathrm{eff}}(\vec{r}) = V(\vec{r}) + V_H(\vec{r}) + \frac{\partial E_{\mathrm{XC}}[n]}{\partial n(\vec{r})} \tag{3.28}$$

by defining a classical Hartree electron-electron interaction potential

$$V_H(\vec{r}) = \frac{\partial J[n]}{n(\vec{r})} = \int \frac{n(\vec{r}')}{|\vec{r} - \vec{r}'|}d\vec{r}' \tag{3.29}$$

with

$$J[n] = \frac{1}{2} \int \frac{n(\vec{r})n(\vec{r}')}{|\vec{r} - \vec{r}'|} d\vec{r} d\vec{r}' \tag{3.30}$$

and the exchange-correlation energy

$$E_{\mathrm{XC}} = T[n] - T_0[n] + E_{ee}[n] - J[n] \tag{3.31}$$

with the electron-electron interaction energy E_{ee}. The terms $T[n]$ and $E_{ee}[n]$ are still not exactly determined, but in practice, approximating E_{XC} with a suitable functional was more succesful than approximating the kinetic energy. Different approaches were developed, such that the local density approximation [52] or the generalized gradient approximations with better average accuracy [54].

There are several commercial and non-commercial implementations of the density functional theory – for example FLEUR [55] or VASP [56] – that share the basic idea, but have differences in details. For this thesis, Quantum Espresso [57, 58] was used. The pseudopotentials for Mn and Te were taken from [59] based on Ref. [60] choosing the PBEsol exchange functional [61, 62], which is a kind of generalized gradient approximation. The input files were generated with help of two tools of the Materials Cloud [63]: the "Quantum ESPRESSO input generator and structure visualizer" [64] based on [65] and "SeeK-path: the k-path finder and visualizer" [66] based on [67] with the software spglib [68] and the parser pymatgen [69].

3.2.1 Wannier functions

In order to obtain hopping matrix elements that we can use in the tight-binding model, we have to find a description of the electronic band structure based on Wannier orbitals. The program WANNIER90 [70] offers this functionality. We give a short overview over Wannier orbitals that is close to Ref. [71].

Due to the lattice structure of crystals, the Hamiltonian has a discrete translational invariance. This symmetry yields to periodic eigenstates – the Bloch states –

$$\psi_{n\vec{k}} = u_{n\vec{k}}(\vec{r}) \exp(i\vec{k} \cdot \vec{r}), \tag{3.32}$$

while $u_{n\vec{k}}$ fulfils the symmetry of the Hamiltonian. These Bloch functions solve the Hamiltonian, but a localized representation would be beneficial. Therefore, unitary transformations are applied to obtain a localized set of functions that are still eigenstates of the Hamiltonian. The new functions are superpositions of Bloch states. The simplest approach would be to include all $\vec{k}$ of the Brillouin zone and to consider equal amplitudes of the contributions:

$$w_{0\vec{r}} = \frac{V}{(2\pi)^3} \int_{\mathrm{BZ}} \psi_{n\vec{k}} d\vec{k} \tag{3.33}$$

with the volume V of the real-space unit cell. This first function, Eq. (3.33), describes the atom localized in the origin (at $\vec{R} = 0$). To calculate other Wannier functions, the amplitudes are modified by the factor $\exp(-i\vec{k}\vec{R})$. In the following, the states are given in the Dirac notation: the state $|\vec{R}n\rangle$ belongs to the wave functions $w_{n\vec{R}}$ in unit cell at real-space lattice vector $\vec{R}$ and band n. Reference [72] shows that the state can be construrcted as

$$|\vec{R}n\rangle = \frac{V}{(2\pi)^3} \int_{\mathrm{BZ}} \exp(-i\vec{k}\vec{R}) |\psi_{n\vec{k}}\rangle d\vec{k}. \tag{3.34}$$

The $|\vec{R}n\rangle$ form an orthonormal basis. The inverse transformation

$$|\psi_{n\vec{k}}\rangle = \sum_{\vec{R}} \exp(i\vec{k}\vec{R}) |\vec{R}n\rangle \tag{3.35}$$

builds the original Bloch states starting from the Wannier states.

In general, the Bloch and the Wannier functions are equally good to describe the system since they are different sets of eigenfunctions for the same eigenenergies. One set can be obtained by a unitary transformation of the other one. Since we aim at a tight-binding modeling, the Wannier functions fit better to our targeted description because they are localized.

The approach for one band is extended to λ bands:

$$|\tilde{\psi}_{n\vec{k}}\rangle = \sum_{j=1}^{\lambda} U_{jn}^{(\vec{k})} |\psi_{n\vec{k}}\rangle. \tag{3.36}$$

The matrix $U_{jn}^{(\vec{k})}$ has the dimension λ, and is periodic in $\vec{k}$. Note that these new states are not longer eigenstates of the Hamiltonian and that the index n does not refer to a band index in the usual way.

3.2.2 Hopping between different types of orbitals

The wanniernization of the DFT results gives us the hopping parameters between different types of and distances between the orbitals. Due to the large size of our unit cell and the large number of neighboring unit that we include, the easiest way to obtain an overview of the hopping is to look at the resulting Hamiltonian in a visualized way. In Fig 3.1, we see the real part of the matrix elements illustrated with colors for $\vec{k} = \vec{0}$. Since the diagonal elements contain mainly the orbital energy, which can be shifted by the Fermi energy, the values of these elements are not displayed.

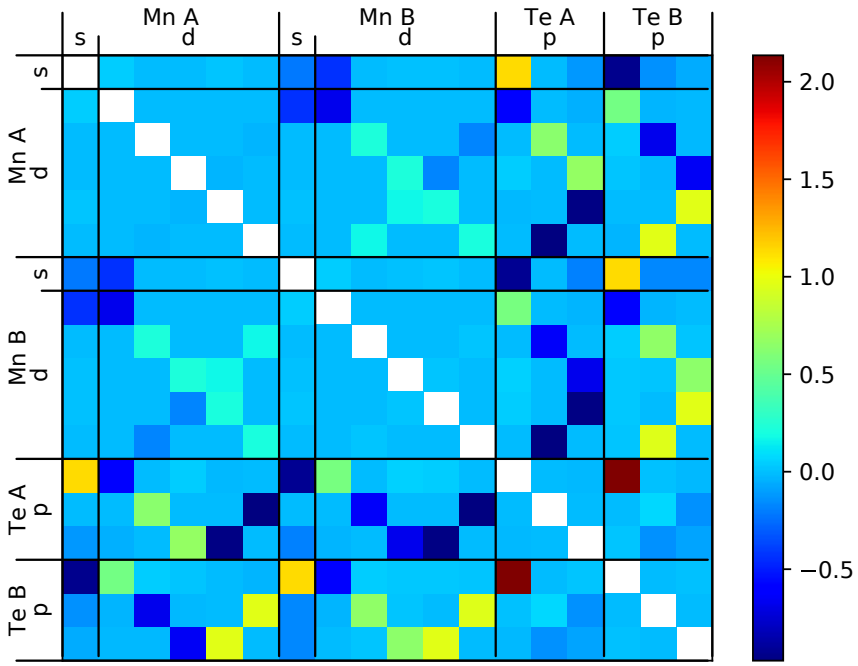

Figure 3.1: Illustration of the Hamiltonian matrix for $\vec{k} = 0$. Each square represents a hopping matrix element. On the left side and at the top, it is defined which kind of orbitals belong to the matrix elements. The value of the hopping is color-coded. The diagonal matrix elements are not shown since their absolute value can be shifted by an arbitrary energy (for example by the Fermi energy). While orbitals at the same atom do not couple strongly, which is reasonable since they are orthogonal in the ideal case, there is hopping between orbitals of different ions in the unit cell. The wanniernization [70] of the Quantum Espresso [57, 58] results was used to obtain these hopping parameters.

The Hamilton matrix differs for each $\vec{k}$ point, however, we get a rough idea which orbitals interact. Orbitals at the same atom do hardly interact, which is shown as light blue entries for examples for (Mn A 3d)–(Mn A 3d) or (Te B 5p)–(Te B 5p). The vanishing hopping is understandable since the atomic wavefunctions should be orthogonal. However, the hopping between orbitals of the same kind on different sites, such as (Mn A 3d)–(Mn B 3d), does not vanish. We see that hopping between d orbitals of different sites is rather small, while two specific Te 5p orbitals show the largest hopping parameter. Each Mn 4s orbital couples to one d orbital of the other Mn-site and one of each Te orbitals. Depending on the Te site, the hopping

parameter is positive or negative.

Note that each entry includes not only hopping between the considered orbitals in one unit cell, but also between neighboring unit cells. We included also next-nearest unit cells. For $\vec{k} = 0$, they sum up in a simple way. For arbitrary $\vec{k}$, each matrix element has a phase factor $\exp(i\vec{k}\Delta\vec{R})$ including the distance $\Delta\vec{R}$ between the orbitals. Next-nearest neighbor unit cells should therefore contribute less then the original unit cell or neighboring unit cells. Due to the decreasing impact when considering unit cells at large distances, we are able to neglect unit cells that are far away from the original one.

The orbital energies obtained by the wanniernization are displayed in Tab. 3.1. They are given relatively to the Fermi energy. Since the DFT results were obtained for a paramagnetic case without correlations, the orbital energies are equal for both Mn or Te atoms. The Te $5p$ orbital energy lie at approximately $-2\,\text{eV}$ clearly under the Fermi energy while the Mn $4s$ orbital energy lies at approximately $1.8\,\text{eV}$ and therefore, significantly above the Fermi energy. The Mn $3d$ orbital energies lie near, but slightly under the Fermi energy with values between $-0.363\,\text{eV}$ and $-0.180\,\text{eV}$. In contrast to the assumption of a splitting in two e_g and three t_{2g} states, only one energy differs from the other four energies.

Table 3.1: Orbital energies in relation to the Fermi energy measured in eV obtained by the wanniernization of the DFT bands.

ϵ_p (Te)	−2.106 995	−1.809 514	−1.809 787		
ϵ_s (Mn)	1.818 969				
ϵ_d (Mn)	−0.362 550	−0.181 645	−0.180 132	−0.180 131	−0.180 166

3.2.3 Dispersion and density of states

Figure 3.2 shows the resulting dispersion obtained by DFT (Quantum Espresso) method as blue lines. All bands are shifted by the Fermi energy $E_F = 7.9511\,\text{eV}$. By applying the wanniernization method for Mn $3d$, $4s$, and Te $5p$ bands, we obtain hopping parameters that we use to build a tight-binding model. We diagonalize it with a solver of the C++ library Armadillo [73, 74]. These results are depicted as red dashed lines. While Fig. 3.2(a) includes a large energy window, Fig. 3.2(b) focuses on the bands around the Fermi energy.

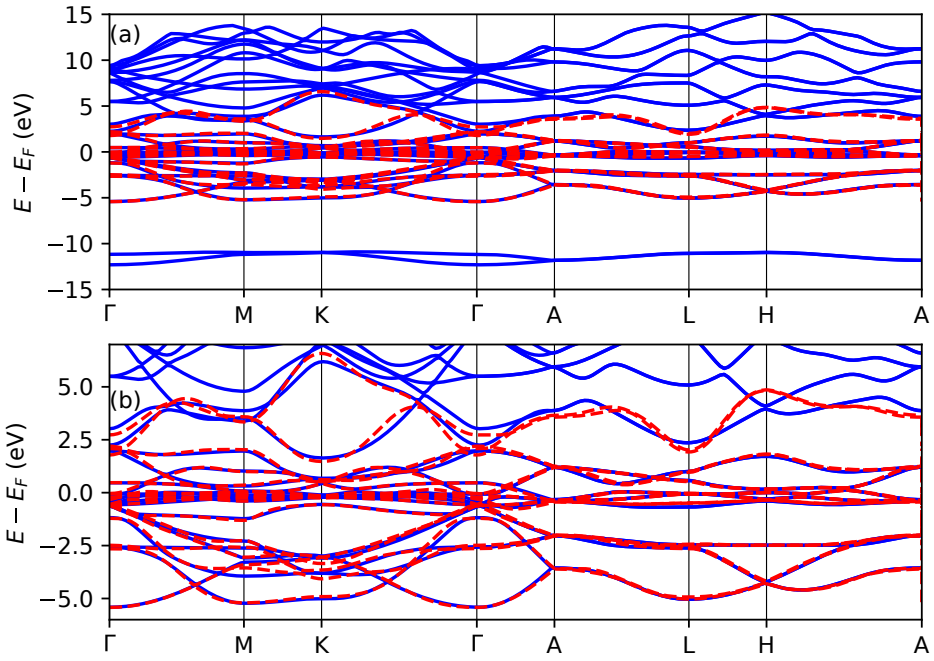

Figure 3.2: Panel (a) shows a part of the dispersion obtained with Quantum Espresso [57, 58] as blue line. In addition, it depicts the calculated dispersion using the hopping parameters gained by Wannernization [70] including Mn $3d$, $4s$, and Te $5p$ orbitals. To focus on the part covered by the wanniernization, we provide a zoom-in in panel (b). Although there are differences to the dispersion calculated by the DFT, the tight-binding model reproduces the dispersion well enough.

All in all, the Wannernization captures very well the targeted bands. The inaccuracy is larger for higher lying bands probably because of neglecting the Mn $4p$ orbitals. Although our tight-binding model shows several deviations, it reproduces the band structure mostly accurately.

The resulting dispersion belongs to a metal as there is no band gap at the Fermi energy since the Mott physics is not captured in the DFT calculations. In a mean field theory, the spins will be aligned alternatively. We mimic this effect by applying

a Hartree shift to the orbital energies in the tight-binding approach:

$$\epsilon_{d,A} \to \epsilon_{d,A} + \frac{U}{2} \tag{3.37a}$$

$$\epsilon_{d,B} \to \epsilon_{d,B} - \frac{U}{2}. \tag{3.37b}$$

For $U = 5\,\mathrm{eV}$, we obtain the dispersion depicted in Fig. 3.3, which has indeed a band gap.

For better understanding, we illustrate the overlap with the orbitals in Fig. 3.3. The color indicates the character of the bands: red means high overlap and blue low overlap with the orginal atomic orbitals. The overlap with the Te $5p$ orbitals is shown in panel 3.3(a), the overlap with Mn $3d$ orbital in panel 3.3(b), and the overlap with Mn $4s$ orbitals in panel 3.3(c). The valence band of our model has mainly Te $5p$ character while the upper Mn $3d$ band forms together with the Mn $4s$ band the conduction band. Especially, at the K point, we see the necessity of including the Mn $4s$ bands.

The density of states show very well the appearence of the band gap when applying the Hartree shift (3.37b). In Fig. 3.4, the blue line shows the density of states in the metallic case while the red curve depicts the insulator case. For the calculation, we use Eq. (3.15) with $\delta = 1 \times 10^{-4}$, and we consider $100 \times 100 \times 100$ $\vec{k}$ points and 150 ω bins. The resulting indirect band gap measures approximately 0.6 eV, which is smaller than the experimental value of $E_g = (1.27 - 1.46)\,\mathrm{eV}$ [33].

The density of states is shifted by the Fermi energy of the paramagnetic calculation. Note that the Fermi energy of the system including the Hartree shift should actually be larger since it should lie in the band gap.

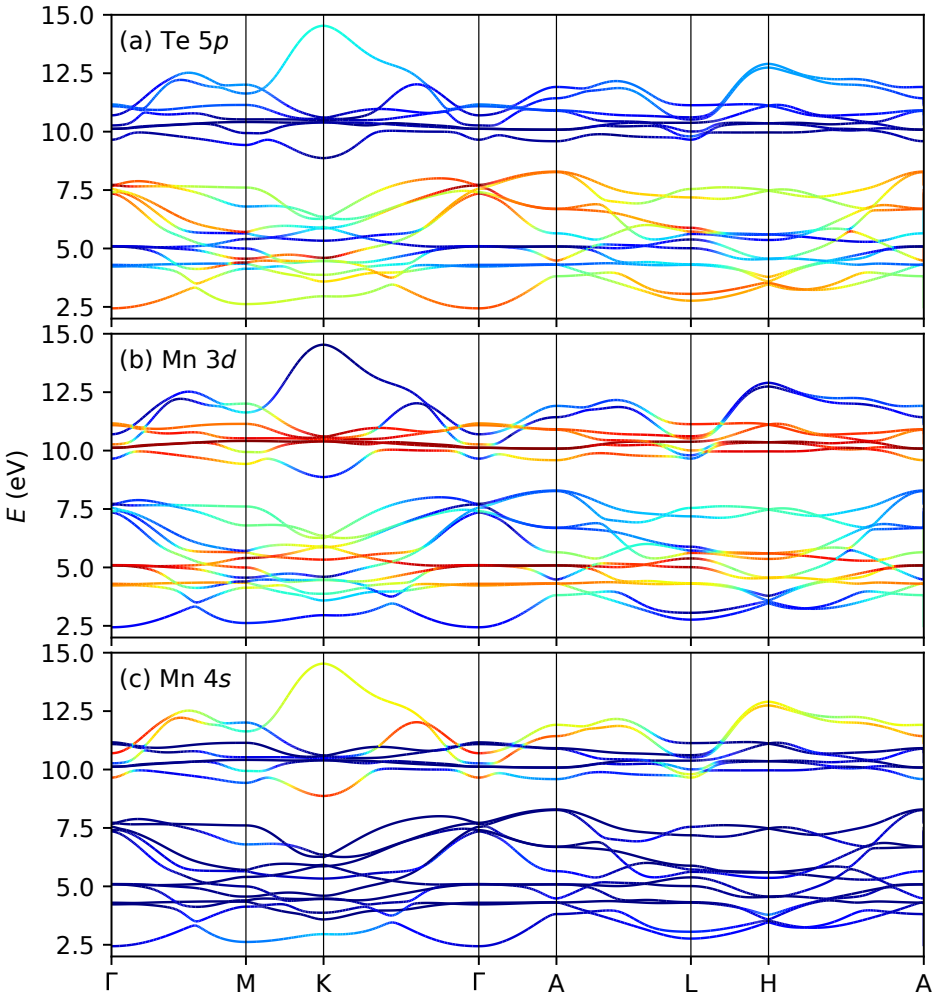

Figure 3.3: The projections on the original atomic orbitals offer us insight in the character of the bands. Panel (a) shows the overlap with Te $5p$ while panel (b) focuses on the Mn $3d$ and panel (c) on Mn $4s$. In addition to the hopping gained from the wanniernization, we include a Hartree shift of 5 eV which splits the Mn $3d$ bands and provides a band gap.

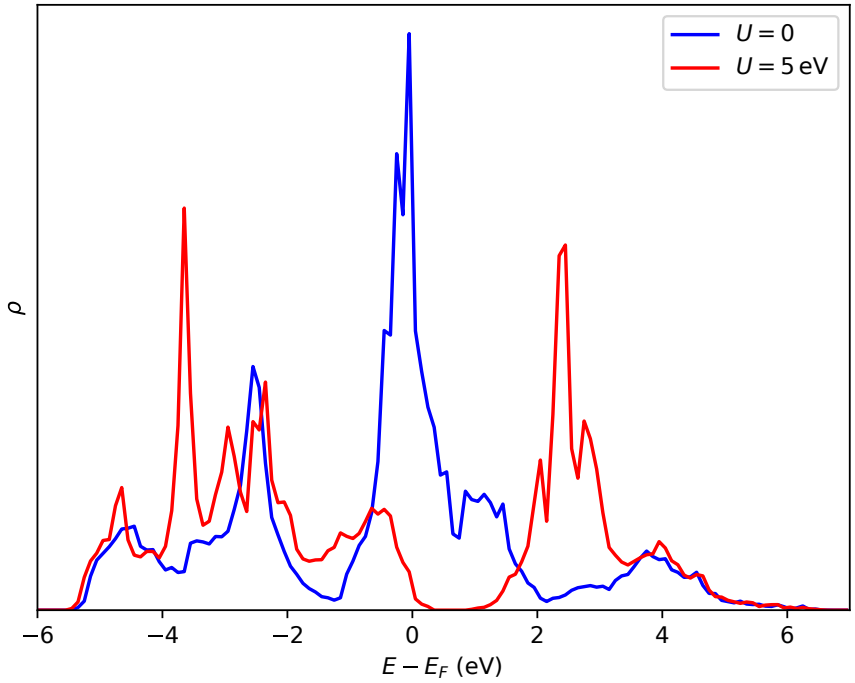

Figure 3.4: The density of states based on the tight-binding model using the hopping parameter obtained by the wanniernization of the DFT results (blue line) shows no band gap at the Fermi energy. When a Hartree shift (3.37b) of $U = 5\,\mathrm{eV}$ is included (red line), a gap appears. Note that both curves are shifted by the Fermi energy in the case without Hartree shift. The actual Fermi energy of the case with Hartree shift should lie in the band gap.

3.3 Summary

We built multi-orbital tight-binding models to describe the electronic structure of α-MnTe. Very important is the choice of included orbitals. Near the Fermi energy are Mn $4s, p$, $3d$, and Te $5p$ bands. Lower in energy, we find Te $5s$ bands, which do not hybridize with the other bands, and therefore, can be neglected.

We calculated the band structure with the density functional theory including the Mn $4s, p$, $3d$, and Te $5p$ orbitals. By performing a wanniernization of density functional theory results, we obtained the hopping parameters between all atoms including up to next-nearest neighboring unit cells. The resulting dispersions are very similar to the DFT calculations. By neglecting correlations, the material is metallic. We do not see a band gap at the Fermi energy because the d bands must be significantly lower in energy compared to the DFT prediction, and the Mott physics must be included.

However, since the main feature of a semiconductor is its band gap, we had to extend the model. We inculded a splitting between the Mn $3d$ bands. In a one-band model, the value of this Hartree shift is the Coulomb interaction. In multi-band model, its value depends also on the Hund's coupling between the spins. We chose a shift of 5 eV, which reproduces the known band structure well enough. We obtained a band gap of 0.6 eV that is smaller than the experimentally measured value of $E_g = (1.27 - 1.46)\,\text{eV}$ [24]. This underestimation is typical for DFT calculations and well known. The dispersion reveals that the Te $5p$ bands form the valence band, while the Mn $3d$ and $4s$ orbitals build the conduction band. Our model is a suggestion for a minimal tight-binding model that captures the main electronic properties of α-MnTe.

Chapter 4

The magnetic shift of the band gap

In this chapter, our objective is to combine the electronic and magnetic properties of α-MnTe in order to calculate the magnetic shift of the band gap observed in experiments [24] and theoretical models [26, 27]. Our approach utilizes a dynamical mean field method in $\vec{k}$ space, which we introduce in Sec. 4.1. The impurity problem is solved using the numerical renormalization group approach, explained in Sec. 4.2. Due to this choice of impurity solver, in contrast to Ref. [26, 27], we are able to calculate continuous spectra, which are more similar to experimental measurable data than discrete spectra. Finally, we perform the numerical calculations in Sec. 4.3 to acquire the spin expectation values and the Green's functions of the Mn $3d$ electrons. The magnetic blue shift of the Mott gap is measured with an appropriate criterion. Furthermore, we insert the resulting self-energy into a multi-orbital tight-binding model to analyze the band gap.

4.1 Dynamical mean-field theory

The dynamical mean-field theory (DMFT) allows the calculation of the electronic structure of strongly correlated materials [75]. For a comprehensive understanding, Ref. [76] provides a good overview.

The primary objective of mean-field theories is to reduce a complex many-body problem into an effective one-body problem. Figure 4.1 provides an illustration of this concept. Solving the resulting equation requires self-consistency, which is comparatively easier than solving the original problem exactly, which is often not possible at all.

The first and very prominent application of the mean-field approach was carried out by Weiss [77]. He calculated the magnetic field of a ferromagnet by defining an

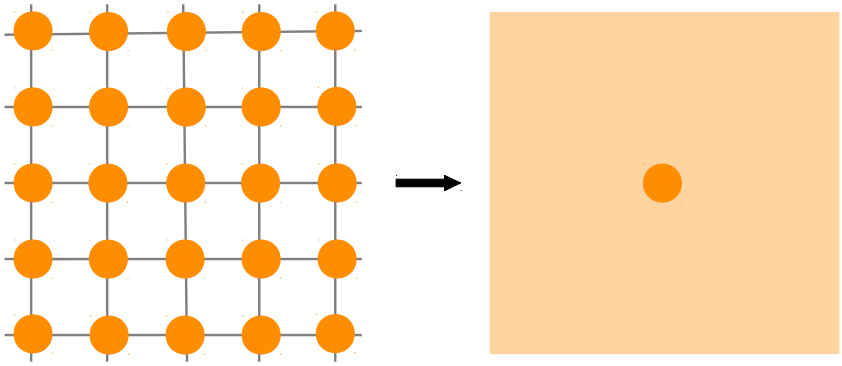

Figure 4.1: Mapping a many-body problem on a one-body problem is the concept of the mean-field theories. While one particle is taken representatively, the effect of the others is described effectively, for example as a field acting on the particle.

effective magnetic field – the Weiss field – that summarizes the impact of all other spins on a single spin:

$$\sum_{ij} J_{ij}\vec{S}_i\vec{S}_j \rightarrow \sum_j \vec{B}_{\mathrm{eff},j}\vec{S}_j \tag{4.1}$$

with the effective field $\vec{B}_{\mathrm{eff},j} = \sum_i J_{ij}\langle\vec{S}_i\rangle$. Equivalently, the Coulomb interaction can be transformed in an effective one-particle term:

$$Un_\uparrow n_\downarrow \rightarrow U\big(n_\uparrow\langle n_\downarrow\rangle + \langle n_\uparrow\rangle n_\downarrow\big). \tag{4.2}$$

A detailed description of the antiferromagnetic Heisenberg model in mean-field approximation can be found in Sec. 4.3.2.

The dynamical mean-field theory extends the original mean-field approach by including the local dynamics. The many-body lattice problem is mapped on a many-body local problem embedded in an effective medium. While this mapping is exact in infinite dimensions, the approximation which is made in the DMFT is assuming that the self-energy is local and $\vec{k}$ independent. In contrast to the conventional mean-field theory, the effective field is time-dependent. The calculation is done iteratively in DMFT loops until the solution has converged.

4.1.1 The DMFT loop

For each iteration, the effective impurity model needs to be solved. In general, different impurity solvers are available, for example, Quantum Monte Carlo methods [78, 79] or exact diagonalization [80]. Here, we will use the numerical renormalization group method (NRG) [81]. An approach for an antiferromagnetic one-band Hubbard model solved by DMFT and NRG is described in Ref. [82]. The steps are:

1. buildung quantum impurity model, guessing an inital self-energy, and choosing initial hybridization functions
2. calculating local Green's function

$$G_\sigma^{\text{imp}} = \frac{1}{z - \epsilon_{d\sigma} + \Sigma_\sigma(z) - \Delta_\sigma(z)} \tag{4.3}$$

   and impurity self-energy with NRG
3. calculating bath Green's function

$$G_\sigma^{\text{lattice}}(z) = \frac{1}{N} \sum_{\vec{k}} \frac{1}{z - \epsilon_{\vec{k}\sigma} - \Sigma_\sigma(z)} = \int \frac{\rho_\sigma(\omega)}{z - \omega - \Sigma_\sigma(z)} d\omega \tag{4.4}$$

4. demanding that

$$G_\sigma^{\text{lattice}} = G_\sigma^{\text{imp}}, \tag{4.5}$$

   the complex, energy dependent media $\Delta_\sigma(z)$ are calculated

$$\Delta_\sigma(z) = -(G_\sigma^{\text{lattice}})^{-1} + \Sigma_\sigma(z) - z \tag{4.6}$$

Steps 2.–4. need to be repeated until the Green's functions and the media $\Delta_\sigma(z)$ do not change any more significantly. In practice, this is checked by calculating the maximum of the absolute deviations of the medium of the current and the previous DMFT iteration. In addition, the same criterion is also applied to the lattice Green's functions. If both deviations are smaller than 1×10^{-3}, we assume that the calculations have converged.

The characteristic approximation of the DMFT – assuming a local self-energy – becomes clear in Eq. (4.4). The equation would be exact if the $\vec{k}$ dependence entered in the self-energy $\Sigma_\sigma(z)$.

Note that there are different approaches to calculate the density of states ρ_σ entering in the lattice Green's function as well as there are different techniques solving an impurity problem besides the NRG method.

4.1.2 Hubbard-Kondo lattice model

To model the five occupied $3d$ orbitals with parallely aligned spins due to Hund's coupling, we consider the Hubbard-Kondo lattice Hamiltonian proposed in Ref. [26][1]. It treats four of these five Mn $3d$ spins localized while one spin $s = 1/2$ remains itinerant:

$$H = -\sum_{ij,\sigma} t_{ij}(c^\dagger_{j\sigma}c_{i\sigma} + h.c.) + U\sum_i n_{i\downarrow}n_{i,\uparrow} - J_H\sum_i \vec{S}_i\vec{s}_i + \sum_{ij} J_{ij}(\vec{S}_i\vec{s}_j + \vec{S}_j\vec{s}_i + \vec{S}_i\vec{S}_j). \tag{4.7}$$

We replace the last term by the mean field Hamiltonian

$$H_{\mathrm{MF}} = -\sum_i (\vec{B}^{\mathrm{loc}}_{\mathrm{eff},i}\vec{S}_i + \vec{B}^{\mathrm{iti}}_{\mathrm{eff},i}\vec{s}_i) \tag{4.8}$$

with the effective magnetic fields

$$\vec{B}^{\mathrm{loc}}_{\mathrm{eff},i} = \sum_i J_i\langle\vec{S}_i + \vec{s}_i\rangle \tag{4.9a}$$

$$\vec{B}^{\mathrm{iti}}_{\mathrm{eff},i} = \sum_i J_i\langle\vec{S}_i\rangle, \tag{4.9b}$$

which leads to the Hamiltonian:

$$H = -\sum_{ij,\sigma} t_{ij}(c^\dagger_{j\sigma}c_{i\sigma} + h.c.) + U\sum_i n_{i\downarrow}n_{i,\uparrow} - J_H\sum_i \vec{S}_i\vec{s}_i + H_{\mathrm{MF}}. \tag{4.10}$$

The effective magnetic fields defined in Eqs. (4.9a) and (4.9b) need to be determined self-consistently. Augmented with a selfconsistency condition for the electronic DOS and the effective Weis fields, we obtain an effective impurity problem which can be solved with DMFT.

Different sets of coupling parameters J_{ij} can be found in the literature (e.g. in Ref. [40] and [41]). If the coupling J_{ij} is antiferromagnetic, there is a relation between J_{ij} and the hopping parameter t_{ij}:

$$J_{ij} = \frac{4t^2_{ij}}{\Delta_U} \tag{4.11}$$

with the bare charge gap $\Delta_U = U + 2J_H$.

[1] Note that our definition of J_H differs by a factor of 2 compared to Ref. [26].

4.1.3 DMFT on a bipartite lattice

In general, the self-energies of different sublattices are different ($\Sigma_\sigma^A \neq \Sigma_\sigma^B$), and two impurity problems should be solved. The Green's function can be written as matrix:

$$G_{\vec{k}\sigma}(z) = \begin{pmatrix} \zeta_\sigma^A - \epsilon_{\vec{k}}^{AA} & -\epsilon_{\vec{k}}^{AB} \\ -\epsilon_{\vec{k}}^{AB} & \zeta_\sigma^B - \epsilon_{\vec{k}}^{BB} \end{pmatrix}^{-1} \tag{4.12a}$$

$$= \frac{1}{(\zeta_\sigma^A - \epsilon_{\vec{k}}^{AA})(\zeta_\sigma^B - \epsilon_{\vec{k}}^{BB}) - (\epsilon_{\vec{k}}^{AB})^2} \begin{pmatrix} \zeta_\sigma^B - \epsilon_{\vec{k}}^{BB} & \epsilon_{\vec{k}}^{AB} \\ \epsilon_{\vec{k}}^{AB} & \zeta_\sigma^A - \epsilon_{\vec{k}}^{AA} \end{pmatrix} \tag{4.12b}$$

with $\zeta_\sigma^{A/B} = z - \Sigma_\sigma^{A/B}$. However, in the Néel state, the properties of sublattice A and spin σ are equal to the properties of sublattice B and the opposite spin $\bar{\sigma}$. In particular, that means: $\zeta_\sigma^A = \zeta_{\bar{\sigma}}^B = \zeta_\sigma$. Therefore, it is sufficient to solve only one effective impurity problem:

$$G_{\mathrm{loc}}^A(z) = G_{ii,\sigma}^{AA}(z) = \frac{1}{N} \sum_{\vec{k}} \frac{\zeta_{\bar{\sigma}} - \epsilon_{\vec{k}}^{BB}}{(\zeta_\sigma - \epsilon_{\vec{k}}^{AA})(\zeta_{\bar{\sigma}} - \epsilon_{\vec{k}}^{BB}) - (\epsilon_{\vec{k}}^{AB})^2}. \tag{4.13}$$

The dispersions $\epsilon_{\vec{k}}^{AA} = \epsilon_{\vec{k}}^{BB}$ and $\epsilon_{\vec{k}}^{AB}$ for α-MnTe include contributions of four different types of nearest-neighbors and can be calculated in the tight-binding formalism:

$$\epsilon_{\vec{k}}^{AB} = -t_1 \cos\left(\frac{c}{2}k_z\right) - t_3\gamma_{\vec{k}} \cos\left(\frac{c}{2}k_z\right) = -(t_1 + t_3\gamma_{\vec{k}}) \cos\left(\frac{c}{2}k_z\right) \tag{4.14a}$$

$$\epsilon_{\vec{k}}^{AA} = \epsilon_{\vec{k}}^{BB} = -t_2\gamma_{\vec{k}} - t_4 \cos(ck_z) \tag{4.14b}$$

$$\text{with } \gamma_{\vec{k}} = \cos(ak_x) + \cos\left(\frac{a}{2}k_x + \frac{\sqrt{3}a}{2}k_y\right) + \cos\left(-\frac{a}{2}k_x + \frac{\sqrt{3}a}{2}k_y\right). \tag{4.14c}$$

For a simple cubic lattice with lattice including only nearest neighbors, there is no hopping between sites of the same sublattice ($\epsilon_{\vec{k}}^{AA} = \epsilon_{\vec{k}}^{BB} = 0$). Equation (4.13) could be written with $\epsilon^{AB} = \epsilon$ as

$$G_{ii,\sigma}(z) = \zeta_{\bar{\sigma}} \int_{-\infty}^{\infty} \frac{\rho(\epsilon)}{\zeta_\uparrow\zeta_\downarrow - \epsilon^2} d\epsilon \tag{4.15}$$

$$= \zeta_{\bar{\sigma}} \int_{-\infty}^{\infty} d\epsilon \frac{\rho(\epsilon)}{2\sqrt{\zeta_\uparrow\zeta_\downarrow}} \left[\frac{1}{\sqrt{\zeta_\uparrow\zeta_\downarrow} - \epsilon} + \frac{1}{\sqrt{\zeta_\uparrow\zeta_\downarrow} + \epsilon}\right], \tag{4.16}$$

which is derived and evaluated in Ref. [82].

Although in α-MnTe, the contributions $\epsilon_{\vec{k}}^{AA}$ and $\epsilon_{\vec{k}}^{BB}$ do not vanish in general, we will follow this simplified approach to gain an understanding of the problem. We will extend the calculations of Ref. [82] by considering a large U and including local spins in our model. Applying Eq. (4.16) to our system requires addionally an approximation of the density of states of α-MnTe. However, it offers already a very good starting point of investigation.

In the paramagnetic case, the sublattices A and B are identical, and the corresponding Green's function is:

$$G(z) = \sum_{\vec{k}} \frac{1}{\zeta - \epsilon_{\vec{k}}} = \int_{-\infty}^{\infty} \frac{\rho(\epsilon)}{\zeta - \epsilon} d\epsilon \tag{4.17}$$

with the density of states

$$\rho(\epsilon) = \frac{1}{N} \sum_{\vec{k};|k_i|\leq\pi} \delta(\epsilon - \epsilon_{\vec{k}}) \tag{4.18}$$

with absorbing the lattice constant in $\vec{k}$. To obtain the same result from two identical sublattices, we start with Eq. (4.16) and take into account that we do not distinguish between $\uparrow$ and $\downarrow$ ($\zeta_\uparrow = \zeta_\downarrow$):

$$\begin{aligned} G_{ii}(z) &= \zeta \int_{-\infty}^{\infty} \frac{\rho^{\text{bip}}(\epsilon)}{2\zeta} \left[\frac{1}{\zeta - \epsilon} + \frac{1}{\zeta + \epsilon} \right] d\epsilon \\ &= \frac{1}{2} \int_{-\infty}^{\infty} \rho^{\text{bip}}(\epsilon) \left[\frac{1}{\zeta - \epsilon} + \frac{1}{\zeta + \epsilon} \right] d\epsilon \end{aligned} \tag{4.19}$$

The Brillouin zone of the doubled unit cell is only half as large, which affects the $\vec{k}$-summation:

$$\rho^{\text{bip}}(\epsilon) = \frac{1}{N} \sum_{\vec{k};|k_i|\leq\pi/2} \delta(\epsilon - \epsilon_{\vec{k}}) \tag{4.20}$$

and the dispersion. In contrast to the single atom per unit cell calculation, we obtain two bands. The representations are equivalent since folding the band of the single atom into the smaller Brillouin zone would exactly yield the second band. In consequence, the resulting density of states $\rho(\epsilon)$ are identical even though the definitions differ. In summary, the calculations assuming a bipartite lattice are equivalent to the calculations of a simple lattice when the material is not magnetically ordered, and therefore, the two sites of the bipartite lattice are equivalent. In the formalism, this is ensured by taking into account the different sizes of the Brillouin zones and the different numbers of bands.

4.1.4 Dealing with five $3d$ bands

Since a multi-orbital calculation is numerically expensive, we need simplifications to treat the five $3d$-bands. We use in our work a one-band Hamiltonian and a Gaussian density of states to model the electronic DOS for a Mn $3d$ band.

A similar, but more accurate way would be to average over all five d-bands to obtain one effective band (and one effective density of states). In a more elaborate model, conceptually, also all five bands could be included. In addition, the crystal field splitting would induce the splitting of the e_g and t_{2g}. However, not more than three bands are feasible numerically with the NRG at the moment.

4.2 Numerical renormalization group method

The numerical renormalization group (NRG) method is a targets quantum impurity problems. The approach was developed by G. Kenneth Wilson [81], who was honored with the Nobel prize in physics in 1982 [83]. The introduction given in this section follows the detailed description of the NRG review by Bulla et al. [84].

A quantum impurity is defined by a few local degrees of freedom coupled to a fermionic or bosonic bath with a typically continious excitation spectrum. In consequence, the general Hamiltonian contains three parts:

$$H = H_{\text{imp}} + H_{\text{bath}} + H_{\text{imp-bath}} \tag{4.21}$$

with the Hamiltonian of the impurity H_{imp}, the Hamiltonian of the bath H_{bath}, and the Hamiltonian $H_{\text{imp-bath}}$ describing the interaction between these subsystems.

It is possible to treat for example strong Coulomb interactions, such as in the single impurity Anderson model (SIAM) for one orbital:

$$H_{\text{imp}} = \sum_{\sigma} \epsilon_d d_\sigma^\dagger d_\sigma + U n_\uparrow n_\downarrow \tag{4.22}$$

with the creation (annihaltion) operator $d_\sigma^\dagger$ (d_σ) that creates (annhilates) an electron with energy ϵ_d. To include both spin orientations, we need to sum over the spin σ. Two electrons on the same site – measured with the occupation operators $n_\sigma = d_\sigma^\dagger d_\sigma$ – increase the energy by U due to Coulomb repulsion.

The bath is represented by a gas of non-interacting fermions (or bosons):

$$H_{\text{bath}} = \sum_{\vec{k},\sigma} \epsilon_{\vec{k},\sigma} c_{\vec{k},\sigma}^\dagger c_{\vec{k},\sigma}. \tag{4.23}$$

The operator $c^{\dagger}_{\vec{k}}$ creates a particle in the bath while $c_{\vec{k}}$ annhilates one. The impact of the bath onto the impurity is captured in the bath spectral function

$$\Gamma_{\sigma}(\omega) = \mathrm{Im}\Delta_{\sigma}(\omega - i\delta) = \pi \sum_{\vec{k}} V^2_{\vec{k}} \delta(\omega - \epsilon_{\vec{k},\sigma}). \tag{4.24}$$

The spatial dimension of the bath does not enter into the dynamic function $\Delta(\omega)$. The bandwidth D is defined by the interval, in which $\Delta(\omega)$ lies: $[-D, D]$ with $D > 0$. When choosing $D = 1$, we can interpret it as energy unit.

The interaction between the impurity and the bath is described by the hybridization $V_{\vec{k}}$:

$$H_{\text{imp-bath}} = \sum_{\vec{k},\sigma} V_{\vec{k}} (d^{\dagger}_{\sigma} c_{\vec{k},\sigma} + c^{\dagger}_{\vec{k},\sigma} d_{\sigma}). \tag{4.25}$$

The Hamiltonian can be reformulated as

$$H = H_{\text{imp}} + \sum_{\sigma} \int_{-1}^{1} g(\epsilon) a^{\dagger}_{\epsilon\sigma} a_{\epsilon\sigma} d\epsilon + \sum_{\sigma} \int_{-1}^{1} h(\epsilon)(d^{\dagger}_{\sigma} a_{\epsilon\sigma} + a^{\dagger}_{\epsilon\sigma} d_{\sigma}). \tag{4.26}$$

This formulation enables a one-dimensional representation of the conduction band in the intervall $[-1, 1]$. The dispersion is given by $g(\epsilon)$ and the hybridization by $h(\epsilon)$. The new band operators obey the Fermi statistics : $[a^{\dagger}_{\epsilon\sigma}, a_{\epsilon\sigma}] = \delta(\epsilon - \epsilon') d_{\sigma\sigma'}$.

The functions $g(\epsilon)$ and $h(\epsilon)$ are related to Γ [85]:

$$\Gamma(\omega) = \pi \frac{d\epsilon(\omega)}{d\omega} h([\epsilon(\omega)]^2) \tag{4.27}$$

with $g(\epsilon)$ being the inverse function to $\epsilon(\omega)$.

To provide a general overview of the method, we list the steps of the method:

a) Division of the bath spectral function $\Gamma(\omega)$ into a set of logarithmic intervals

b) Reducing of the continuous spectrum to a discrete set of states

c) Mapping of the discretized model onto a semi-infinite chain

d) Iterative diagonalization of this chain

e) Further analysis of the many-particle energies and matrix elements

4.2.1 Logarithmic discretization

To discretize the Hamiltonian of Eq. (4.26), the discretization points

$$x_n = \pm\Lambda^n \text{ with } \Lambda \in \mathbb{N}_0 \tag{4.28}$$

are used, where Λ parametrizes the location and width

$$d_n = \Lambda^{-n}(1 - \lambda^{-1}) \tag{4.29}$$

of the intervals. The part of the spectrum belonging to a discretization point is approximated as single state. In consequence, for a discretization parameter $\Lambda \to 1$, the method would be exact.

In each interval, an orthonormal basis is defined:

$$\psi^{\pm}_{n,p}(\epsilon) \begin{cases} \frac{1}{\sqrt{d_n}} \exp(\pm i\omega_n p_\epsilon), & \text{for } x_{n+1} < \pm\epsilon < x_n, \\ 0 & \text{outside the interval} \end{cases} \tag{4.30}$$

with the fundamental frequencies $\omega_n = 2\pi/d_n$. The index p covers all integer values between $-\infty$ and ∞.

Next, the conduction band electrons are expanded in this basis:

$$a_{\epsilon\sigma} = \sum_{np} [a_{np\sigma}\psi^{+}_{np}(\epsilon) + b_{np\sigma}\psi^{-}_{np}(\epsilon)]. \tag{4.31}$$

The structure of the expansion is equivalent to a Fourier transform on each interval. The inverse transformation is given by

$$a_{np\sigma} = \int_{-1}^{1} [\psi^{+}_{np}(\epsilon)]^* a_{\epsilon,\sigma} d\epsilon, \tag{4.32a}$$

$$b_{np\sigma} = \int_{-1}^{1} [\psi^{-}_{np}(\epsilon)]^* a_{\epsilon,\sigma} d\epsilon. \tag{4.32b}$$

The Hamiltonian is now in a discretized form, while $a^{(\dagger)}_{np\sigma}$ and $b^{(\dagger)}_{np\sigma}$ obey the fermionic anticommutator relation.

The discretized form of the hybridization reads

$$\int_{-1}^{1} h(\epsilon) d^\dagger_\sigma a_{\epsilon\sigma} d\epsilon = d^\dagger_\sigma \sum_{np} \left[a_{np\sigma} \int^{+,n} h(\epsilon)\psi^{+}_{np}(\epsilon) d\epsilon + b_{np\sigma} \int^{-,n} h(\epsilon)\psi^{-}_{np}(\epsilon) d\epsilon \right] \tag{4.33}$$

with the abbreviated notation

$$\int^{+,n} d\epsilon \equiv \int_{x_{n+1}}^{x_n} d\epsilon, \quad \int^{-,n} d\epsilon \equiv \int_{-x_n}^{-x_{n+1}} d\epsilon. \tag{4.34}$$

For the special case $h(\epsilon) = h = \text{const.}$, only the $p = 0$ contribution of Eq. (4.33) contributes, which leads to

$$\int^{\pm,n} d\epsilon h \psi^{\pm}_{np}(\epsilon) = \sqrt{d_n} h \delta_{p,0}. \tag{4.35}$$

To assume a constant hybridization function in each interval was important for Wilson's original argumentation. To deal with non-constant hybridization functions, a step function is defined. This function is constant in each interval, but can have different values in different intervals:

$$h(\epsilon) = h_n^{\pm}, \quad x_{n+1} < \pm\epsilon < x_n. \tag{4.36}$$

The value $h_n^{\pm}$ is defined by the average of the hybridization function in the corresponding interval:

$$h_n^{\pm 2} = \frac{1}{d_n} \int^{\pm,n} \frac{1}{\pi} \Gamma(\epsilon) d\epsilon \tag{4.37}$$

with $\gamma_n^{\pm 2} = \int^{\pm,n} \Gamma(\epsilon)$.

As a result, the hybridization part of the Hamiltonian reads

$$\int_{-1}^{1} h(\epsilon) d_\sigma^\dagger a_{\epsilon\sigma} d\epsilon = \frac{1}{\sqrt{\pi}} d_\sigma^\dagger \sum_n (\gamma_n^+ a_{n0\sigma} + \gamma_n^- b_{n0\sigma}). \tag{4.38}$$

The term describing the conduction band electrons also has to be discretized. We obtain

$$\begin{aligned} \int_{-1}^{1} g(\epsilon) a_{\epsilon\sigma}^\dagger a_{\epsilon\sigma} d\epsilon = & \sum_{np} (\xi_n^+ a_{np\sigma}^\dagger a_{np\sigma} + \xi_n^- b_{np\sigma}^\dagger b_{np\sigma}) \\ & + \sum_{n, p \neq p'} [\alpha_n^+(p,p') a_{np\sigma}^\dagger a_{np'\sigma} - \alpha_n^-(p,p') b_{np\sigma}^\dagger b_{np'\sigma}] \end{aligned} \tag{4.39}$$

with

$$\xi_n^{\pm} = \frac{\int^{\pm,n} \epsilon \Gamma(\epsilon) d\epsilon}{\int^{\pm,n} \Gamma(\epsilon) d\epsilon} = \frac{1}{2} \Lambda^{-n} (1 + \Lambda^{-1}) \tag{4.40}$$

for the first term, which contains only contributions diagonal in p. In contrast, the second term covers all off-diagonal elements. A linear dispersion $g(\epsilon) = \epsilon$ yields

$$\alpha_n^{\pm}(p,p') = \frac{1 - \Lambda^{-1}}{2\pi i} \frac{\Lambda^{-n}}{p' - p} \exp\left(\frac{2\pi i (p' - p)}{1 - \Lambda^{-1}} \right). \tag{4.41}$$

Neglecting all $p \neq 0$ contributions and relabeling (index p is omitted) leads to

$$\begin{aligned} H = H_{\text{imp}} + \sum_{n\sigma} (\xi_n^+ a_{n\sigma}^\dagger a_{n\sigma} + \xi_n^- b_{n\sigma}^\dagger b_{n\sigma}) + \frac{1}{\sqrt{n}} \sum_\sigma d_\sigma^\dagger \sum_n (\gamma_n^+ a_{n\sigma} + \gamma_n^- b_{n\sigma}) \\ + \frac{1}{\sqrt{n}} \sum_\sigma \Big(\sum_n (\gamma_n^+ a_{n\sigma}^\dagger + \gamma_n^- b_{n\sigma}^\dagger) \Big) d_\sigma. \end{aligned} \tag{4.42}$$

In order to improve the numerical results, it is possible to apply the z-averaging [86–88]. In this case, the calculation is done several times with modified discretization points. They are varied slightly via the value z in the exponent of Λ

$$x_n = \begin{cases} 1, & n = 0, \\ \Lambda^{-n+z}, & n \geq 1, \end{cases} \tag{4.43}$$

and finally, an average over all results is considered.

To overcome the systematic underestimation of the hybridization function [89], a correction can be introduced. For the constant hybridization, the correction is given by

$$A_\Lambda = \frac{1}{2} \frac{\Lambda + 1}{\Lambda - 1} \ln(\Lambda). \tag{4.44}$$

4.2.2 Mapping on a semi-infinite chain

Next, the discretized Hamiltonian is mapped on a semi-infinite chain with first site of the chain being the impurity. The hopping between the sites decreases exponentially with distance to the first site due to the logarithmic discretization: $t_n \propto \Lambda^{-n/2}$. Each iteration corresponds to a specific energy scale.

The hybridization can be reformulated as

$$\frac{1}{\sqrt{\pi}} d_\sigma^\dagger \sum_n (\gamma_n^+ a_{n\sigma}^\dagger + \gamma_n^+ b_{n\sigma}) = \sqrt{\frac{\xi_0}{\pi}} d_\sigma^\dagger c_{0\sigma} \tag{4.45}$$

by using the definition

$$c_{0\sigma} = \frac{1}{\sqrt{\xi_0}} \sum_n (\gamma_n^+ a_{n\sigma} + \gamma_n^- b_{n\sigma}) \tag{4.46}$$

with the renormalization factor

$$\xi_0 = \sum_n \left[(\gamma_n^+)^2 + (\gamma_n^-)^2 \right] = \int_{-1}^{1} \Gamma(\epsilon) d\epsilon. \tag{4.47}$$

The Hamiltonian can be tranformed to a semi-infinite chain form:

$$\begin{aligned} H = H_{\text{imp}} + \sqrt{\frac{\xi_0}{\pi}} \sum_{\sigma} (d_\sigma^\dagger c_{0\sigma} + c_{0\sigma}^\dagger d_\sigma) \\ + \sum_{\sigma,n=0}^{\infty} [\epsilon_n c_{n\sigma}^\dagger c_{n\sigma} + t_n (c_{n\sigma}^\dagger c_{n+1,\sigma} + c_{n+1,\sigma}^\dagger c_{n,\sigma})]. \end{aligned} \tag{4.48}$$

The operator $c_n^\dagger$ (c_n) creates (annihilates) a fermion on the nth site of the chain. The previous operators a_n, b_n are related by an orthogonal transformation:

$$a_{n\sigma} = \sum_{m=0}^{\infty} u_{mn} c_{m\sigma}, \quad b_{n\sigma} = \sum_{m=0}^{\infty} v_{mn} c_{m\sigma}, \tag{4.49a}$$

$$c_{n\sigma} = \sum_{m=0}^{\infty} (u_{nm} a_{m\sigma} + v_{nm} b_{m\sigma}). \tag{4.49b}$$

The coefficients of the first sum are obtained by the definition of $c_{0\sigma}$ in Eq.(4.46):

$$u_{0m} = \frac{\gamma_m^+}{\sqrt{\xi_0}}, \quad v_{0m} = \frac{\gamma_m^-}{\sqrt{\xi_0}}. \tag{4.50}$$

The other coefficients, gained by exploiting the equivalence of the free conduction electron parts electron

$$\begin{aligned} \sum_{n\sigma} (\xi_n^+ a_{n\sigma}^\dagger a_{n\sigma} + \xi_n^- b_{n\sigma}^\dagger b_{n\sigma}) \\ = \sum_{\sigma,n=0}^{\infty} [\epsilon_n c_{n\sigma}^\dagger c_{n\sigma} + t_n (c_{n\sigma}^\dagger c_{n+1,\sigma} + c_{n+1,\sigma}^\dagger c_{n,\sigma})], \end{aligned} \tag{4.51}$$

are given by

$$\epsilon_n = \sum_m (\xi_m^+ u_{nm}^2 + \xi_m^- v_{nm}^2), \tag{4.52a}$$

$$t_n^2 = \sum_m [(\xi_m^+)^2 u_{nm}^2 + (\xi_m^-)^2 v_{nm}^2] - t_{n-1}^2 - \epsilon_n^2, \tag{4.52b}$$

$$u_{n+1,m} = \frac{1}{t_n} [(\xi_m^+ - \epsilon_n) u_{nm} - t_{n-1} u_{n-1,m}], \tag{4.52c}$$

$$v_{n+1,m} = \frac{1}{t_n} [(\xi_m^- - \epsilon_n) v_{nm} - t_{n-1} v_{n-1,m}] \tag{4.52d}$$

for $n \geq 1$. The initial relations are

$$\epsilon_0 = \frac{1}{\xi_0} \int_{-1}^{1} \Gamma(\epsilon) \epsilon d\epsilon, \tag{4.53a}$$

$$t_0^2 = \frac{1}{\xi_0} \sum_m [(\xi_m^+ - \epsilon_0)^2 (\gamma_m^+)^2 + (\xi_m^- - \epsilon_0)^2 (\gamma_m^-)^2], \tag{4.53b}$$

$$u_{1m} = \frac{1}{t_0} (\xi_m^+ - \epsilon_0) u_{0m}, \tag{4.53c}$$

$$v_{1m} = \frac{1}{t_0} (\xi_m^- - \epsilon_0) v_{0m}. \tag{4.53d}$$

While the recursion needs to be solved numerically for arbitary hybridizations, analytical solutions were found for special cases. Considering a Kondo model with constant hybridization function in the interval $[-1, 1]$ leads to

$$t_n = \frac{(1 + \Lambda^{-1})(1 - \Lambda^{-n-1})}{2\sqrt{1 - \Lambda^{-2n-1}}\sqrt{1 - \Lambda^{-2n-3}}} \Lambda^{-n/2} \tag{4.54}$$

for example [81]. For large n, the equation simplifies to

$$t_n \to \frac{1}{2}(1 + \Lambda^{-1}) \Lambda^{-n/2}. \tag{4.55}$$

We see that the the hopping t_n decreases exponentially. The sites of the chain can be interpreted as shells around the impurity.

4.2.3 Iterative diagonalization

The resulting Hamiltonian is solved iteratively. This means that in each step one site of the chain is added and enlarges therefore the Hilbert space. When a given maximum number of states N in the Hilbert space is reached, the first N lowest-lying states are kept while the $N + 1$st state and all following are discarded. By applying this procedure, the size of the Hilbert space is constant for all following iterations.

The Hamiltonian (4.48) can interpreted as a series of Hamiltonians, which approaches the original Hamiltonian in the limit $N \to \infty, \lambda \to 1^+$:

$$H = \lim_{\Lambda \to 1^+} \lim_{N \to \infty} \Lambda^{-(N-1)/2} H_N(\Lambda) \tag{4.56}$$

with

$$H_N = \Lambda^{(N-1)/2}\Big(H_{\rm imp} + \sqrt{\frac{\xi_0}{\pi}}\sum_\sigma (d_\sigma^\dagger c_{0\sigma} + c_{0\sigma}^\dagger d_\sigma) + \sum_{\sigma,n=0}^{N} \epsilon_n c_{n\sigma}^\dagger c_{n\sigma} + \sum_{\sigma,n=0}^{N-1} t_n (c_{n\sigma}^\dagger c_{n+1,\sigma} + (c_{n+1,\sigma}^\dagger c_{n\sigma})\Big). \tag{4.57}$$

The following Hamiltonian H_{N+1} is connected to H_N via

$$H_{N+1} = \sqrt{\Lambda} H_N + \Lambda^{N/2}\sum_\sigma \epsilon_{N+1} c_{N+1,\sigma}^\dagger c_{N+1,\sigma} + \Lambda^{N/2}\sum_\sigma t_N (c_{N\sigma}^\dagger c_{N+1,\sigma} + c_{N+1,\sigma}^\dagger c_{N,\sigma}), \tag{4.58}$$

with the first Hamiltonian H_0 of this sequence is given by

$$H_0 = \Lambda^{-1/2}\Big(H_{\rm imp} + \sum_\sigma \epsilon_0 c_{0\sigma}^\dagger c_{0\sigma} + \sqrt{\frac{\xi_0}{\pi}}\sum_\sigma (d_\sigma^\dagger c_{0\sigma} + c_{0\sigma}^\dagger d_\sigma)\Big). \tag{4.59}$$

The recursion to obtain the next Hamiltonian H_{N+1} can be interpreted as a renormalization group transformation R:

$$H_{N+1} = R(H_N). \tag{4.60}$$

In the NRG scheme, we define the Hamiltonian H_N directly by the many-particle eigenenergies E_N

$$H_N |r\rangle_N = E_N(r)|r\rangle_N, \quad r = 1, ..., N_s \tag{4.61}$$

with the eigenstates $|r\rangle_N$ and the dimension N_s of the Hamiltonian.

Starting from the eigenstates of Eq. (4.61), the basis of the next Hamiltonian H_{N+1} is constructed:

$$|r; s\rangle_{N+1} = |r\rangle_N \otimes |s(N+1)\rangle. \tag{4.62}$$

These states are a product state of the basis of H_N with a basis for the added site $|s(N+1)\rangle$.

For a system, with conserved total charge Q and the component S_z of the total spin, the new basis is

$$|Q, S_z, r; 1\rangle_{N+1} = |Q+1, S_z, r\rangle_N, \tag{4.63a}$$

$$|Q, S_z, r; 2\rangle_{N+1} = c_{N+1,\uparrow}^\dagger |Q, S_z - \frac{1}{2}, r\rangle_N, \tag{4.63b}$$

$$|Q, S_z, r; 3\rangle_{N+1} = c_{N+1,\downarrow}^\dagger |Q, S_z + \frac{1}{2}, r\rangle_N, \tag{4.63c}$$

$$|Q, S_z, r; 4\rangle_{N+1} = c_{N+1,\uparrow}^\dagger c_{N+1,\downarrow}^\dagger |Q-1, S_z, r\rangle_N. \tag{4.63d}$$

Conservation numbers reduce the size of the calculated matrices, which is favorable for the numerical run time and in some cases for the feasibility.

With a new basis $|r,s\rangle_{N+1}$, the Hamiltonian matrix is

$$H_{N+1}(r,s,r',s') =_{N+1} \langle r,s|H_{N+1}|r',s'\rangle_{N+1}. \tag{4.64}$$

For further processing, the new Hamiltonian is divided into three parts:

$$H_{N+1} = \sqrt{\Lambda} H_N + \hat{X}_{N,N+1} + \hat{Y}_{N+1}. \tag{4.65}$$

Besides the rescaled Hamiltonian H_N and the operator $\hat{Y}_{N+1}$ describing the new site, the interaction $\hat{X}_{N,N+1}$ between both is included. Diagonalizing the new Hamiltonian leads to the new eigenenergies and eigenstaates. The later is related via a unitary transformation to the old eigenstates:

$$|w\rangle_{N+1} = \sum_{rs} U(w,rs)|r;s\rangle_{N+1}. \tag{4.66}$$

The number of eigenenergies grows exponentially in each step. The spectrum is shifted such that the lowest energy is 0. Furthermore, due to numerical limitations, the energy spectrum is truncated, and only the lowest N_s states are kept, and the computation time only grows linearly with the number of sites. The truncation is based on the idea that high energies do not affect the properties of the system at low energies. The exponential decrease of the hopping between the site of the chain underlines this argument. Since the coupling to an additional bath orbital is of the order of t, it is a minor correction for the energy that is significantly larger than t. For the following sites of the chain, these corrections have usually no relevant effects. However, it is not guaranteed that the effect of the high energy excitations in neglectable for an arbitary application. In addition, the number of kept states has to be chosen large enough to capture all necessary excitations.

4.2.4 Calculation of physical properties

The various physical properties of a system depend on the density operator $\hat{\varrho}$, which describes the quantum states of the system. Assuming to know the many-body eigenstates $|r\rangle$ and the corresponding eigenvalues E_r, the density matrix $\varrho(T)$ and the partition function $Z(T)$ are

$$\varrho(T) = \frac{1}{Z(T)} \sum_r \exp(-\beta E_r)|r\rangle\langle r|, \tag{4.67}$$

$$Z(T) = \sum_r \exp(-\beta E_r) \tag{4.68}$$

with the inverse temperature $\beta = 1/(k_B T)$.

The chain length N determines the inverse temperature:

$$\beta_N \Lambda^{-(N-1)/2} =: \bar{\beta}. \tag{4.69}$$

with the factor $\bar{\beta}$. The concrete value of $\bar{\beta}$ has to be chosen for calculations, appropriate values are of the order of 1. By changing $\bar{\beta}$ by a small value, it is possible to calculate the physical properties for a slightly different temperature T_N.

Local properties

While some static properties, such as the entropy, the specific heat, and the susceptibility can be determined directly from the spectra of the Hamiltonian, for other static properties, such as the local occupancy, the local matrix elements have to be calculated.

The expectation values for the occupancy $n_\sigma = d_\sigma^\dagger d_\sigma$ is approximated by

$$\begin{aligned} n_\sigma(T) \approx \frac{1}{Z^{(N)}(T)} \sum_{Q,S_z} \sum_r \exp(-\beta E_N(Q,S_z,r)) \\ \cdot {}_N\langle Q,S_z,r|d_\sigma^\dagger d_\sigma|Q,S_z,r'\rangle_N. \end{aligned} \tag{4.70}$$

The matrix elements ${}_N\langle Q,S_z,r|d_\sigma^\dagger d_\sigma|Q,S_z,r'\rangle_N$ of step N are calculated by transforming the matrix elements of step $N-1$ with Eq. (4.66).

Dynamic properties

In this thesis, we also aim to calculate dynamical properties of the system: the Green's functions

$$G_\sigma(\omega,T) = \int_{-\infty}^{\infty} d(t-t') \exp(i\omega(t-t')) G_\sigma(t-t'), \tag{4.71}$$

$$G_\sigma(t-t') = -i\theta(t-t')\langle d_\sigma(t), d_\sigma^\dagger(t')\rangle_\varrho \tag{4.72}$$

with the density matrix ϱ.

The spectral function

$$A_\sigma(\omega,T) = \frac{1}{\pi} \mathrm{Im} G_\sigma(\omega + i\delta, T) \tag{4.73}$$

can be written in the Lehmann representation:

$$A_\sigma(\omega,T) = \frac{1}{Z(T)}\sum_{rr'}|M_{rr'}|^2\Big(\exp\Big(-\frac{E_r}{k_BT}\Big)+\exp\Big(-\frac{E_{r'}}{k_BT}\Big)\Big) \cdot\delta(\omega-(E_{r'}-E_r)) \tag{4.74}$$

with the many-body matrix element $M_{rr'} = \langle r|d_\sigma|r'\rangle$.

For $T = 0$, the spectral function is

$$\begin{aligned} A_\sigma(\omega,T=0) =& \frac{1}{Z(0)}\sum_{rg}|M_{r,g}|^2\delta(\omega+(E_r-E_0)) \\ &+\frac{1}{Z(0)}\sum_{rg}|M_{g,r'}|^2\delta(\omega-(E_{r'}-E_0)) \end{aligned} \tag{4.75}$$

with the ground state energy E_0 and g being one state of the ground state manifold. In the framework of the NRG, $T = 0$ implies that we have reached the stable low temperature fixed point of the system. A fixed point (FP) is invariant under a renormalization transformation

$$H^*(\mathrm{FP}) = R^2[H^*]. \tag{4.76}$$

Note that the renormalization transformation has to be applied twice for fermions [84].

Since the energies are always shifted such that $E_0 = 0$, we write Eq.(4.75) as

$$\begin{aligned} A^N_\sigma(\omega,T=0) =& \frac{1}{Z_N(0)}\sum_{r}|M^N_{r,0}|^2\delta(\omega+E^N_r) \\ &+\frac{1}{Z_N(0)}\sum_{r}|M^N_{0,r'}|^2\delta(\omega-E^N_{r'}) \end{aligned} \tag{4.77}$$

with N iterations.

Considering finite temperatures $T > 0$, the spectral function is similar to Eq. (4.74). The temperature is determined by the number of iterations n and Boltzmann factors have to be included:

$$\begin{aligned} A_\sigma(\omega,T) &\approx A^n_\sigma(\omega,T) \\ &= \frac{1}{Z_n(T)}\sum_{r}|M^n_{rr'}|^2\Big(\exp\Big(-\frac{E^n_r}{k_BT}\Big)+\exp\Big(-\frac{E^n_{r'}}{k_BT}\Big)\Big) \\ &\cdot\delta(\omega-(E^n_{r'}-E^n_r)) \end{aligned} \tag{4.78}$$

Its calculation is more difficult since excitations of arbitary energies enter.

4.2.5 Broadening of discrete spectra

A true continuum model has continious spectra while the NRG provides discrete spectra. To compare experiemental and numerical data, the resulting delta peaks $\delta(\omega \pm E_r^N)$ are broadened according to distributions $P(\omega \pm E_r^N)$. There are different choices for P, such as a Gaussian broadening distribution

$$P_G(\omega \pm E_r^N) = \frac{1}{\eta_N \sqrt{pi}} \exp(-[(\omega \pm E_r^N)/\eta_N]^2) \tag{4.79}$$

with the width η_N or the logarithmic broadening distribution

$$P_{\mathrm{LG}}(\omega \pm E_r^N) = \frac{e^{-b^2/4}}{bE_r^N \sqrt{\pi}} \exp(-[(\ln(|\omega|/E_r^N))/b]^2). \tag{4.80}$$

with the broadening parameter b. The advantage of the logarithmic broadening is that the distribution preserves the sign of the excitation frequency. However, in practice, both approaches usually differ only very little. For our application, we chose the logarithmic broadening, although we expect no spectrum around $\omega = 0$, which leads to the assumption that the Gaussian broadening should not change the sign either.

4.2.6 Choice of parameters

We have to choose the parameters Λ and N_s carefully since they determine the precision of our calculations. If Λ is too large, the intervals summerized to one state are so large that the approximation is not valid. If we keep not enough states, we discard states that are still important for the next iterations. Furthermore, to obtain the same precision if we want to decrease Λ, we have to keep more states in the truncation scheme. At the end, we need a reasonable set of parameters that ensures physical results as well as has acceptable numerical costs. In the following calculations, we set $\Lambda = 1.8$ and $N_s = 2000$ for a single band calculation.

In addition, meshes on which the physical values are calculated are defined during the numerical procedure. To capture all excitations, they have to be dense enough in the intervals where excitations appear. Furthermore, they should be fine enough to depict for example the peaks of the Green's functions appropiately.

We always choose $\epsilon_d = -U/2$. That ensures particle-hole symmetry for the paramagnetic phase when $\Delta(\omega) = \Delta(-\omega)$, and a Mott phase is enforced for large U.

As broadening, we choose $b = 0.8$ if not stated differently. Since the main effect of the increasing band gap for lower temperatures is the narrowing of bands, the broadening of the bands has a major effect on the results and should be chosen carefully.

4.3 Numerical results

By solving the Hubbard-Kondo model similar to Ref. [26] with the dynamical mean field theory and the numerical renormalization group method as impurity solver, we can calculate different physical quantities. The most important ones are the spectral functions, the self-energy, and the spin expectation values.

After a successful termination of the DMFT loop, the local Green's function equals the lattice Green's function except of small numerical errors depending on the chosen accuracy. In the following, we will focus on the imaginary parts of the Green's functions since they are connected to the spectral functions (c. f. Eq. (4.73)). The spectral functions contain information about the occupation of the spin channels. When the spectral functions of $\uparrow$ and $\downarrow$ are equal and symmetric,

$$A_\uparrow(\omega) = A_\downarrow(\omega), \quad A_\sigma(\omega) = A_\sigma(-\omega), \tag{4.81}$$

we are in the paramagnetic phase, since the order parameter is zero.

In the magnetically ordered phase, one spectral function has more spectral weight below $\omega = 0$ and the other one above $\omega = 0$. There is still a symmetry between the spins $A_\uparrow(\omega) = A_\downarrow(-\omega)$, which results in the fact that their sum is still particle-hole symmetric:

$$A_\uparrow(\omega) + A_\downarrow(\omega) = A_\uparrow(-\omega) + A_\downarrow(-\omega). \tag{4.82}$$

For $T = 0$ and $U \to \infty$, one spectral function has only spectral weight for $\omega < 0$ and the other for $\omega > 0$, which means that the system is fully polarized.

The self-energy describes corrections to the bare energy of an orbital in the NRG method. It is calculated via two Green's functions using the approach of Ref.[90]

$$\Sigma_\sigma(z) = U\frac{F_\sigma(z)}{G_\sigma(z)} \tag{4.83a}$$

$$\text{with } F_\sigma(z) = \langle d_\sigma d^\dagger_{-\sigma} d_{-\sigma} | d^\dagger_\sigma \rangle(z) \tag{4.83b}$$

$$G_\sigma(z) = \langle d_\sigma | d^\dagger_\sigma \rangle(z), \tag{4.83c}$$

to reduce the broadening dependency. While the imaginary part induces a lifetime of the quasi-particles, the real part contains information about an energy shift. For

$T \to 0$, this shift is independent of ω and therefore equal to a Hartree shift, while the imaginary part vanishes. However, for higher temperatures, the self energy has a more complex structure.

We calculate the spin expectation values of the itinerant electron $\langle \vec{s}_{z,\mathrm{iti}} \rangle$ as well as of the local spin $\langle \vec{S}_{z,\mathrm{loc}} \rangle$ by calculating the occupation and multiplying with the spin length. In addition, the spin polarization of the itinerant spin is also accessible by calculating the occupation of the majority and minority band via integrating the spectral function, determining the difference, and multiplying with 1/2. The result becomes even more accurate if the spectral functions are normalized after the DMFT+NRG procedure. Both methods lead to very similar results. For consistency reasons, we use the direct expectation values since we can gain the local spin expectation value only with this method.

The sum of these expectation values $\langle \vec{s}_{z,\mathrm{iti}} \rangle + \langle \vec{S}_{z,\mathrm{loc}} \rangle$ is the sublattice magnetization per site – the order parameter of an antiferromagnetic system, determining whether the system is in the paramagnetic or antiferromagnetic phase by analyzing the spin expectation values.

Generally, $\langle \vec{s}_{z,\mathrm{iti}} \rangle + \langle \vec{S}_{z,\mathrm{loc}} \rangle = 0$ implies the absence of the magnetic order. However, due to numerical inaccurancies the calculated order parameter can show even above T_N small finite values, which makes the determination of T_N less precise.

4.3.1 Effective description with a Gaussian density of states

We consider a one-band Hubbard model with a Gaussian density of states in this thesis. This simplified approach offers already interesting qualitative insights into the physics of α-MnTe. We focus only on the Mn $3d$ subsystem and do not differentiate between the different d states. Although, we are aware that the real density of states deviates from a Gaussian, the main results for the magnetization and the band gap should be similar. Instead of using the hopping term stated in the first term of Eq.(4.10), our model uses only the density of states. The Gaussian density of states is obtained in the limit of infinite dimensions ($d \to \infty$) for a cubic lattice

$$\epsilon_{\vec{k}} = -2t \sum_{i}^{d} \cos(k_i) \tag{4.84}$$

with absorbing the lattice constant into k_i [91]:

$$\rho(\epsilon) = \frac{1}{2t\sqrt{\pi d}} \exp\Big(- \frac{\epsilon}{2t\sqrt{d}} \Big). \tag{4.85}$$

A finite kinetic energy is obtained by rescaling the hopping parameter

$$t = \frac{t^*}{2\sqrt{d}}, \tag{4.86}$$

which leads to

$$\rho(\epsilon) = \frac{1}{\sqrt{\pi}} \exp\left[\left(-\frac{\epsilon^2}{(t^*)^2}\right)^2\right]. \tag{4.87}$$

The parameter t^* determines the unit of energy.

We determine the width of the effective Gaussian density of states with the Heisenberg couplings J_i, the Coulomb parameter U, and the Hund's coupling J_H. For the Heisenberg coulpings, we use the same parameter set as Ref. [26], which has used four different types of Heisenberg couplings of Ref. [41]:

$$J_1 = 3.072\,\text{meV} \tag{4.88a}$$
$$J_2 = 0.0272\,\text{meV} \tag{4.88b}$$
$$J_3 = 0.4\,\text{meV} \tag{4.88c}$$
$$J_4 = 0.16\,\text{meV}. \tag{4.88d}$$

With a given Coulomb parameter U and Hund's coupling J_H, the corresponding hopping parameters can be calculated:

$$J_n = \frac{4t_n^2}{U + 2J_H}. \tag{4.89}$$

Reference [26] has calculated the change of the Mott gap for different sets of $\{U, J_H\}$, which led all to a similar value. We focus on

$$U = 5.5\,\text{eV} \text{ and } J_H = 1.6\,\text{eV}, \tag{4.90}$$

which turned out to match well the experimental blue shift in Ref. [26].

We follow the idea that a Gaussian density of states can be adjusted to match approximately the width of the densities of states obtained by including $\{J_1, J_2, J_3, J_4\}$ and the actual crystal structure. Therefore, the effective hopping t_{eff} [26] has to be calculated:

$$t_{\text{eff}} = \frac{1}{2}\sqrt{J_{\text{eff}}\Delta_U} \tag{4.91}$$
$$\text{with} \quad J_{\text{eff}} = \sum_i \sigma_i Z_i J_i \tag{4.92}$$

with the number of nearest neighbors Z and a sign $\sigma_i = +1$ for antiparallel alignment und $\sigma_i = -1$ for antiparallel alignment of the spins, which leads to

$$J_{\text{eff}} = 2J_1 - 6J_2 + 12J_3 - 2J_4 \tag{4.93}$$

for the considered system.

4.3.2 Comparison to a Heisenberg model

In the limit of large U/t and J_H/t, the Hubbard-Kondo model can be mapped onto a Heisenberg model after eliminating the charge fluctuations. In order to compare our results to the simpler Heisenberg description, we focus briefly on the Heisenberg model in mean-field approximation as presented in Ref. [47].

The mean field solution of a Heisenberg model

$$H = -\sum_{\langle i,j \rangle} J\vec{S}_i\vec{S}_j \tag{4.94}$$

is well known in the ferromagnetic and antiferromagnetic case. Both are very similar, but for convienience, let us concentrate on antiferromagnetic coupling in the following to relate to the magnetic order in MnTe.

In the mean field approximation, we focus on a local spin and consider the effect of the other spins as effective magnetic field:

$$H_{\text{eff}} = \sum_i \vec{B}_{\text{eff}}\vec{S}_i \tag{4.95}$$

with the effective field

$$\vec{B}_{\text{eff}} = \sum_j J\langle\vec{S}_j\rangle = ZJ\langle\vec{S}_j\rangle \tag{4.96}$$

with the number of neighbors Z belonging to the coupling J. The magnetization per site is the expectation value of the spin:

$$m = \langle\vec{S}_i\rangle. \tag{4.97}$$

This expectation value can be calculated

$$m = B_S(x) \tag{4.98}$$

with the Brillouin function

$$B_S(x) = \frac{2S+1}{2S}\coth\left(\frac{2S+1}{2S}x\right) - \frac{1}{2S}\coth\left(\frac{1}{2S}x\right) \tag{4.99}$$

and

$$x = S\frac{-ZJm}{T} \tag{4.100}$$

while S stands for the spin length.

As a result, we obtain the self-consistent equation (4.98), which has always the solution $m = 0$. There is no analytic solution for this equation, but we are able to solve it numerically or graphically.

The graphical method offers an intuitive comprehension of the possible solutions. Below the Néel temperature, the Brillouin function and the linear function $f(m) = m$ cross twice: at $m = 0$ and at a finite m which means that the self-consistent equation (4.98) has two solutions. Above T_N, there is only one solution: $m = 0$. As a result, the Brillouin function and the linear function have the same gradient at $m = 0$ only for exactly T_N. By evaluating Eq. (4.98) with the expansion of the Brillouin function in first order of x, we obtain

$$T_N = -ZJ\frac{S(S+1)}{3}. \tag{4.101}$$

The approximation $x \ll 1$ is valid because the magnetization m is small at $T = T_N$. Note that the resulting temperature is positive since J is negative in the considered antiferromagnetic case.

If we consider in addition spins that are aligned parallely due to the crystal structure, for example Z' next-nearest neighbors coupling via J', only the sign would change, and the critical temperature is a sum of both contributions: $T_N = \frac{S(S+1)}{3}(-ZJ + Z'J')$.

Figure 4.2 shows the magnetization of the Hubbard model on a bipartite lattice with the Gaussian density of states and realistic parameters as red crosses. In addition, the spin polarizations for $\{U = 7\,\mathrm{eV}, J_H = 2\,\mathrm{eV}\}$ and $\{U = 3\,\mathrm{eV}, J_H = 0.5\,\}$ are plotted. The grey line depicts the mean field Heisenberg solution with $S = 5/2$. Overall, the agreement between the numerical DMFT results for the Hubbard-Kondo model and the mean field Heisenberg model is good. We will use the Heisenberg solution can predict the Néel temperature.

Only near the Heisenberg Néel temperature, the numerical data tends to have a smaller magnetization indicating that the actual Néel temperature is slightly smaller than the analytical prediction. Furthermore, the magnetization for temperatures slightly above the Néel temperature is larger than 0. Fitting the Heisenberg solution to our data would be an alternative ansatz. But first, the numerical results tend to have systematic errors near to the phase transition, which make the fit procedure less precise at the Néel temperature. Second, the implementation of the fitting is not straightforward since there is no closed analytic solution.

Extended Heisenberg model

Although, the Hubbard model behaves as a simple Heisenberg model in the limit of large U, a more elaborate Heisenberg description is imaginable. In our DMFT calculations, we consider one itinerant 1/2-spin $\vec{s}_i$ and one local 2-spin $\vec{S}_i$ per site to model the spin of 5/2 formed in the Mn $3d$ orbitals. The itinerant and the local spin are coupled via the Hund's rule coupling J_H. In consequence, the simple Heisenberg model (HM) is not perfectly suitable to describe our results. An extended, effective description yields the Hamiltonian

$$H_{\text{eff}} = \sum_{\langle i,j \rangle} J(\vec{S}_i + \vec{s}_i)(\vec{S}_j + \vec{s}_j) - \sum_i J_H \vec{S}_i \vec{s}_i \tag{4.102}$$

$$= \underbrace{\sum_{\langle i,j \rangle} J\vec{S}_i\vec{S}_j}_{\text{HM with } \vec{S}} + \underbrace{\sum_{\langle i,j \rangle} J\vec{S}_i\vec{s}_j + \sum_{\langle i,j \rangle} J\vec{s}_i\vec{S}_j}_{\text{HMs with different spin lenghts}} + \underbrace{\sum_{\langle i,j \rangle} J\vec{s}_i\vec{s}_j}_{\text{HM with } \vec{s}} \underbrace{- \sum_i J_H \vec{S}_i\vec{s}_i}_{\text{energy reduction}} . \tag{4.103}$$

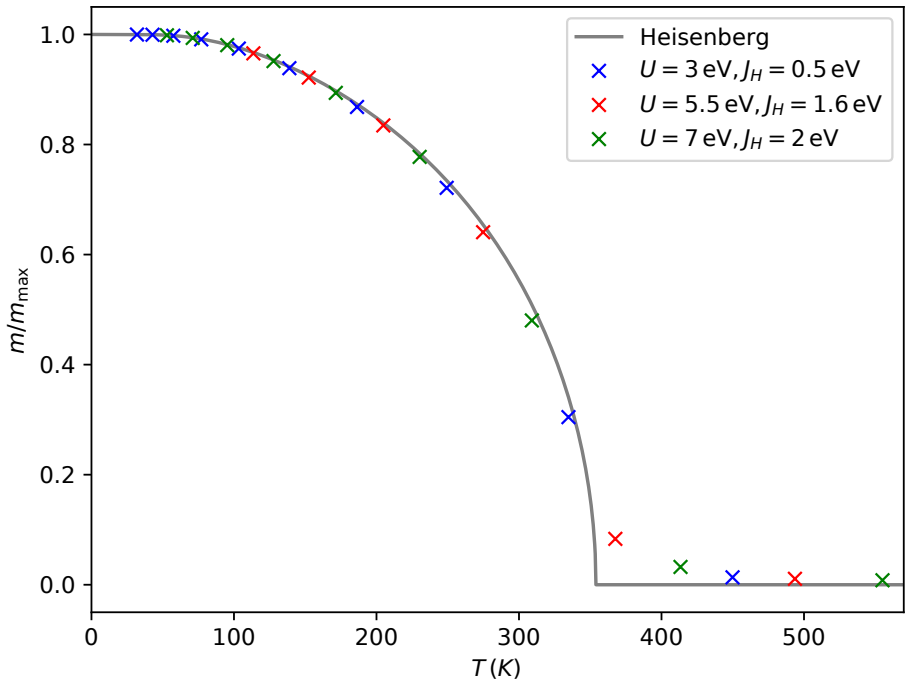

Figure 4.2: The magnetization follows with good agreement the Heisenberg solution for $S = 5/2$.

This effective description contains two well known Heisenberg terms with equal spins $\vec{S}$ and $\vec{s}$, two Heisenberg terms that couple spins of different lengths, and a term describing the energy reduction gained by aligning the itinerant and the local spin on one site.

Calculating the exact solution of the sums of Heisenberg terms with different spin lengths becomes more difficult. In general, we have to consider also configurations with antiparallel $\vec{S}_i$ and $\vec{s}_i$. We do not follow this approach further since the agreement of the magnetization and the mean field Heisenberg solution ist already very good. However, without further calculations, one main effect is already evident: there is an energy shift due to the Hund's coupling.

4.3.3 Measuring the band gap via the spectral functions

One of the major goals is to determine the band gap in α-MnTe. In this section, we will focus on the Mott gap of the Mn $3d$ bands. It is important to note that the presented results of Δ_g do not display the actual band gap in which we are interested. The band structure suggests mainly that the Te $5p$ bands form the valence band, and the upper Mn $4s$ and $3d$ bands are the conduction band. We follow Ref. [26]: the actual magnetic blue shift is therefore given by half of the total shift in our model since only the change of one $3d$ band influences the actual gap.

We need to find a suitable criterion since the spectral functions depending on the chosen density of states have a pseudo gap.

One approach to calculate the band gap makes use of the Green's functions. Examplarily, the Green's functions for the two different spin channels are shown below and above the Néel temperature in Fig. 4.3. In the paramagnetic phase, the spectral functions for both spin channels lie on top of each other. In the antiferromagnetic phase, the Green's functions differ significantly from each other. Additionally, the antiferromagnetic Green's functions are narrower than the paramagntic ones.

To calculate the higher band edge, we can determine the energy $\Delta_g/2$ at which a certain high percentage c of the spectral weight of the occupied part of the electron spectral function $A(\omega)$ is covered:

$$cA_{\mathrm{tot}} = \int_{\Delta_g/2}^{\infty} A(\omega)d\omega \tag{4.104}$$

with

$$A_{\mathrm{tot}} = \frac{1}{2}\int_{-\infty}^{\infty} A(\omega)d\omega. \tag{4.105}$$

Due to the symmetry, the value of the lower band gap is the same while the sign

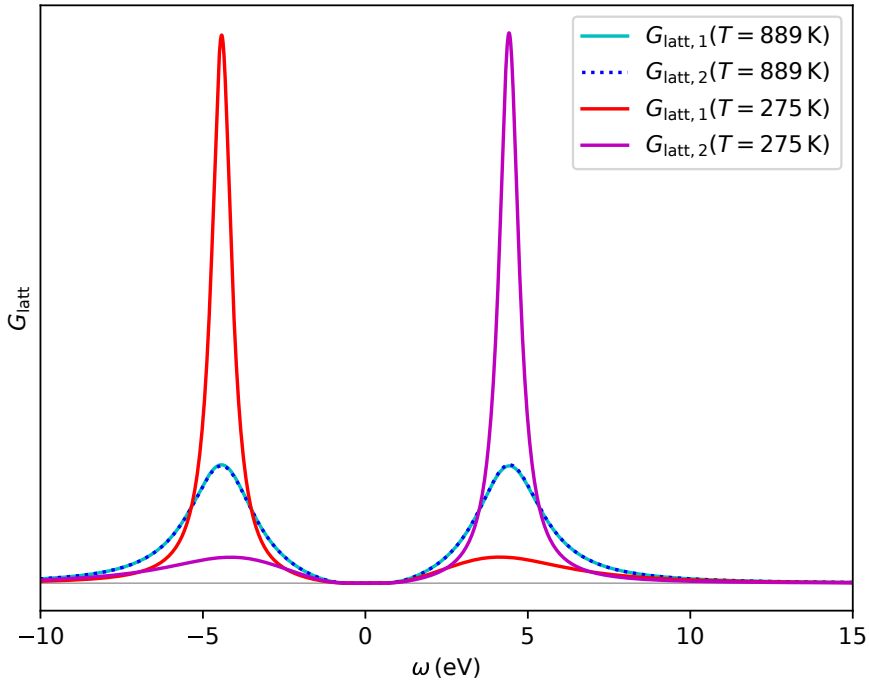

Figure 4.3: Exemplarily, the Green's functions in the paramagnetic ($T \approx 889\,\text{K}$) and in the antiferromagnetic phase ($T \approx 275\,\text{K}$). While above the Néel temperature, the Green's functions for the different spin channels coincide, they show significant differences in the magnetically ordered phase.

changes. The spectral function $A(\omega)$ is the average of the majority and minority band:

$$A(\omega) = A_1(\omega) + A_2(\omega). \tag{4.106}$$

In the antiferromagnetic case, A_1 and A_2 differ significantly while A_1 and A_2 are identical in the paramagnetic phase and therefore coincident with $2 \cdot A$. Consequently, the terms majority and minority spin do not fit in the magnetically unordered case. However, the method itself is suitable in both cases. The paramagnetic spectral functions evolve to spin polarized functions when decreasing the temperature.

Ideally, we would choose $c = 1$. However, since the functions have only a pseudogap, which means that the spectral weight becomes very small for small $|\omega|$, but is always finite. Consequently, the calculated band gap would always lie at $\omega = 0$. To overcome this numerical artifact, we consider a slightly smaller cut-off $c < 1$ to

obtain more reasonable band gaps, which depend on the temperature.

An illustration of the integral criterion is shown in Fig 4.4. In panel (a), the spectral functions $A_1(\omega)$ and $A_2(\omega)$ are depicted. Their average $A(\omega)$ is integrated up to a cut-off c, which determines $\Delta_g/2$ as illustrated in panel (b). For better visibility of the concept, the cut-off $c = 0.9$ is chosen for this figure. This cut-off is rather small; we will consider larger cut-offs in general.

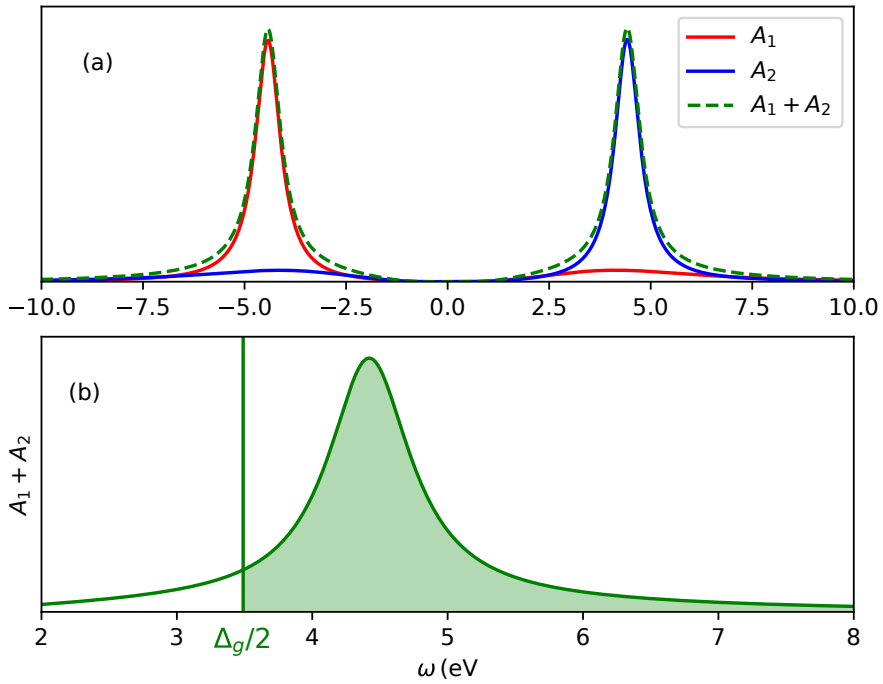

Figure 4.4: Schematic description of the integral criterion. Panel (a) shows the spectral functions A_1 and A_2 at $T \approx 275\,\mathrm{K}$. To apply the integral criterion, both spectral functions are added and integrated until the integral reaches a certain relative amount c of the total integral. The upper bound of this integral determines the size of the gap $\Delta_g/2$ as shown in panel (b).

We determine $\Delta_g/2$ for the magnetic and the paramagnetic case. The difference between the results is defined as the magnetic blue shift $(\Delta_{g,\mathrm{af}} - \Delta_{g,\mathrm{pm}})/2$ since the gap typically increases in the magnetically ordered phase.

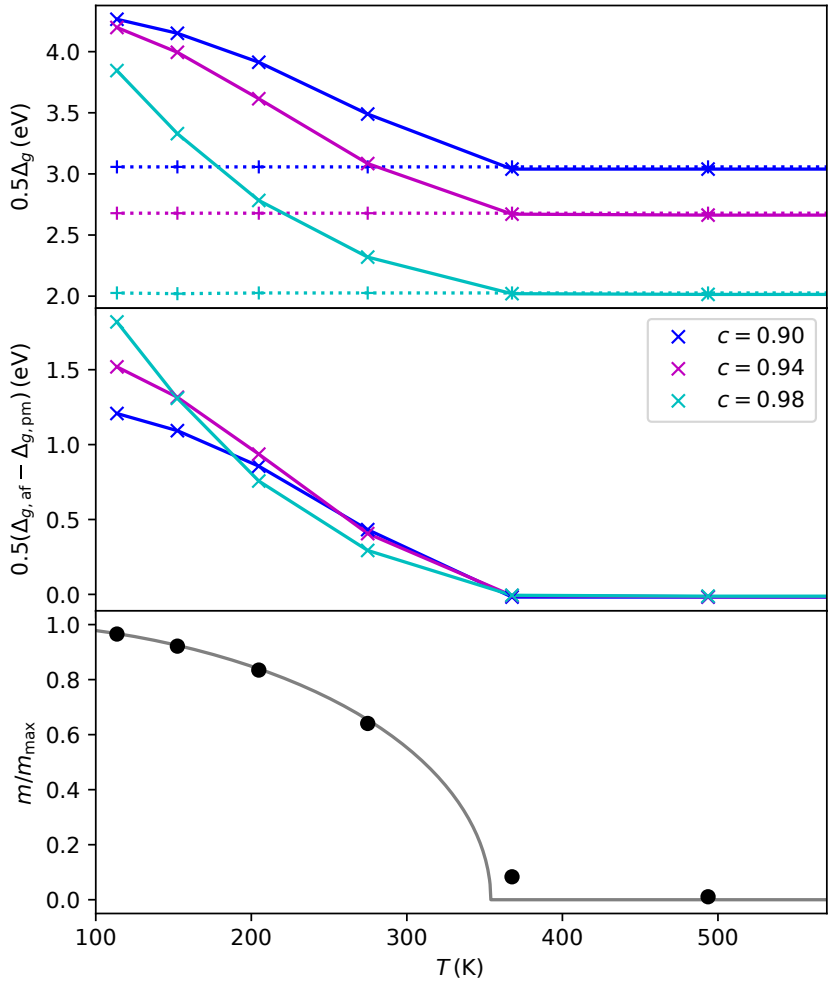

Figure 4.5: The band gaps, the magnetic blue shifts, and the magnetization for an effective Gaussian DOS and the parameters of Eqs. (4.88) and (4.90). Panel (c) shows that the magnetization is finite below the Neél temperature. At the same temperature, the magnetically ordered and the hypothetic paramagnetic solutions begin to differ as depicted in panel (a). The absolute values of the band gap depend on the cut-off c. Especially, the band gap of the paramagnetic phase changes strongly with c. The magnetic blue shift – the difference between the band gap in the antiferromagnetic and hypothetic paramagnetic phase is shown in panel (b).

Even below the Néel temperature, we can model the paramagnetic case by applying an average of the spin channels of the medium. These curves remain constant when we lower the temperature. This approach enables us to measure directly for each temperature the effect of the magnetization.

Figure 4.5(c) depicts the magnetization $m/m_{\max}$ and the mean field Heisenberg solution in order to compare directly the magnetization to the Mott gaps.

The Mott gaps calculated with Eq. (4.104) for the magnetic solution as well as the spin-symmetrized solution for different cut-offs c are shown in Fig. 4.5(a). The Mott gap $\Delta_g/2$ in the spin-symmetrized case is independent of the temperature but differs strongly with the chosen cut-off. The Mott gap of calculations allowing magnetic order coincide with the spin-symmetrized case above T_N and increases below T_N.

The magnetic blue shift for different cut-offs c is shown in Fig. 4.5(b). For the chosen cut-offs, the magnetic blue shift increases when increasing the cut-off.

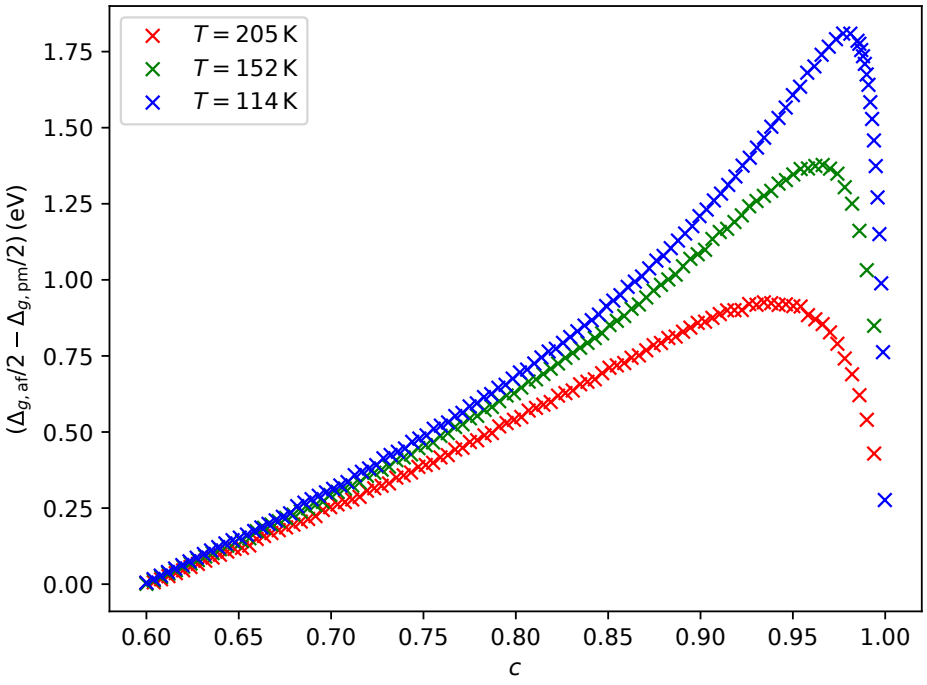

Figure 4.6: The magnetic blue shift $(\Delta_{\mathrm{af}} - \Delta_{\mathrm{pm}})/2$ depends strongly on the chosen cut-off c. While it increases firstly with increasing cut-off, it decreases for cut-offs near to 1.

To focus more on the dependence of the magnetic blue shift on the cut-off, Fig. 4.6 shows the magnetic blue shift for three temperatures below the Néel temperature, $T \approx 114\,\mathrm{K}$, $T \approx 152\,\mathrm{K}$, and $T \approx 205\,\mathrm{K}$, in dependence of the cut-off c. We observe also that there is a dependence between the maximum value of the blue shift and the cut-off.

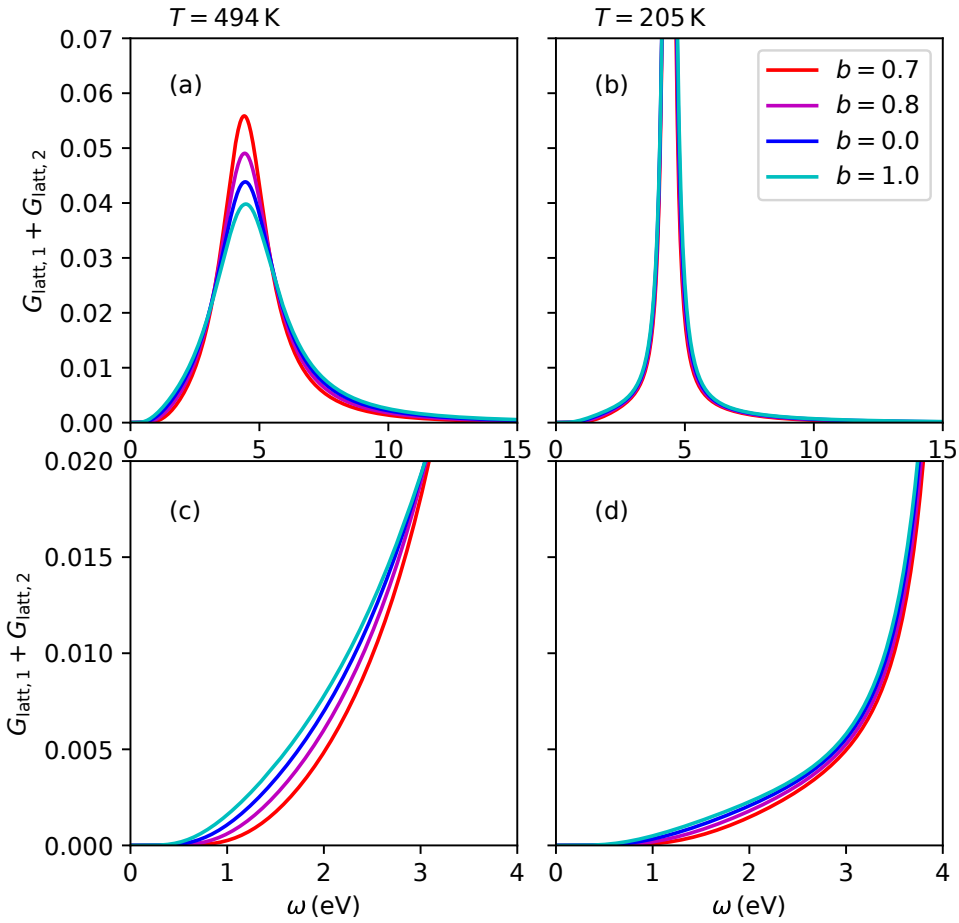

Figure 4.7: The spectral functions for (a) $T \approx 494\,\mathrm{K}$ and (b) $T \approx 205\,\mathrm{K}$ in dependence of the broadening b. Panels (c) and (d) show zoom-ins of (a) and (b) to focus on the tail of the spectral functions.

First the magnetic blue shift increases with increasing cut-off until a cut-off above

0.9. The exact position of this maximum depends on the temperature. Next it drops rapidly. We can understand this by considering two extreme cases. For $c = 0.5$, we cover only half of the spectrum of interest. Because the maxima lie at approximately the same frequency in the paramagnetic and antiferromagnetic case, and only the width of the peak differs, we obtain the same band gap, and hence, there is no magnetic blue shift. For $c = 1$ and Gaussian density of states, we need to integrate to $\omega = 0$ in both cases since the spectra have only a pseudo gap. In consequence, the magnetic blue shift vanishes. Only in the intermediate regime, a blue shift can be measured with this method.

The differences between the considered temperatures can be explained by the width of the belonging Green's function. For smaller temperatures, the Green's functions are very narrow, which explains rather large Mott gaps. Only if we consider very large cut-offs, we need to integrate also the spectral weight lying far away from the maximum in the tail of the function. Since there is only very little spectral weight, the resulting Mott gap drops more drastically than for broader Green's functions at higher temperatures.

For the integral criterion, the width of the spectral functions determines mainly the resulting Mott gap Δ_g. Since the width depends on the broadening b of the NRG method, we need to have a closer look to its effect. Figure 4.7 shows the spectral functions for $T \approx 494\,\mathrm{K}$ (panel (a) and (c)) and $T \approx 205\,\mathrm{K}$ (panel (b) and (d)). The panels (c) and (d) show a zoom-in of panels (a) and (b). For both depicted temperatures, the curves are wider if the broadening is chosen larger. However, the effect is significantly smaller for lower temperatures.

Figure 4.8 quantifies the effect of the broadening by calculating the Mott gap $\Delta_g/2$ for different broadenings between $b = 0.7$ and $b = 1.0$ and the temperatures $T \approx 114\,\mathrm{K}$, $T \approx 204\,\mathrm{K}$ and $T \approx 494\,\mathrm{K}$ for fixed cut-off $b = 0.96$. The Mott gaps become smaller when increasing the broadening. But the smaller the temperature, the smaller the decrease is, since the Green's functions do not change so much depending on the broadening for lower temperatures as shown in Fig. 4.7.

While the magnetic blue shift is well capured qualitatively with this criterion, the absolute value of the Mott gap for $T \to \infty$ is too small compared to experiments, which means that the magnetic blue shift of our model is much larger than the blue shift measured in experiments.

By choosing a smaller broadening, the Mott gap of the paramagnetic phase becomes larger. Unfortunately, it is not possible to choose arbitary small broadenings since the convergence of the DMFT loop only works reliably for broadenings that are not too small. For our case, we chose $b = 0.8$ for all calculations if not stated differently.

The most important advange of the integral criterion is that it can be applied in the magnetic and paramagnetic phase. But unfortunately, the results depend very much on the choice of the cut-off c and the broadening b.

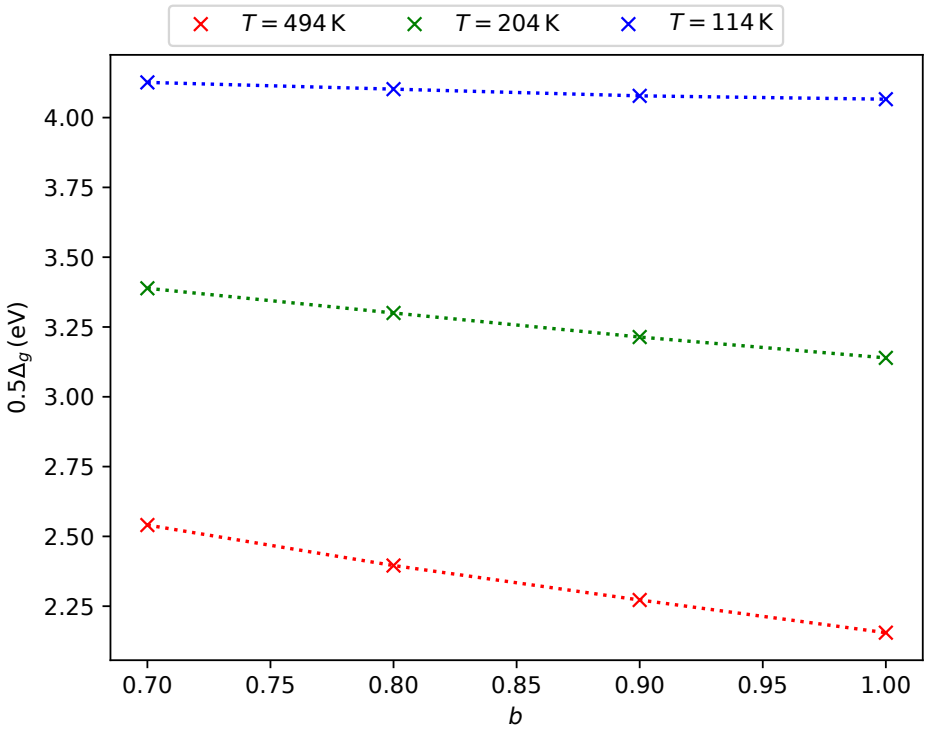

Figure 4.8: The $\Delta_g/2$ vs the broadening b for different temperatures and $c = 0.96$. The effect of a decreasing Mott gap for increasing broadening is stronger for higher temperatures.

4.3.4 Renormalized band structure

We can include the self-energy in the calculation of the band structure using a tight-binding Hamiltonian as in Chap. 3. The real part of the self-energy shifts the oribital energy, while the imaginary part induces a broadening of the bands. This broadening is reciprocally ascociated to the lifetime of particles.

The self-energy of the d electrons contains information about the band gap in the magnetic phase. For very low temperatures, $T \ll T_N$, the real part of the self-energy Σ is nearly independent of ω shown in Fig. 4.9(c). This constant value differs

between the majority and the minority spin. The difference between both can define the band gap.

For higher temperatures which are still below T_N, there is a clear ω-dependence as depicted in Fig. 4.9(b) and (c). The imaginary parts of the spin channels are symmetric, while the real parts are point symmetric around $(0, U/2)$.

For $\omega \to \pm\infty$, a convergent behaviour of the reals part is visible. The finite value of the upper self-energy is smaller if the temperature is larger. For the lower self-energy, the inverse relation holds. As a result, the difference between both limit values increases when decreasing the temperature.

To analyze the effect of the self-energy of the Mn d electrons, we include it into a multi-orbital tight-binding model. We consider the Mn $3d$, the Mn $4s$, and the Te $5p$ as in Chap. 3. The spectral function includes now multiple orbitals, such that the following equation holds:

$$A(\omega, \vec{k}) = -\frac{1}{\pi}\mathrm{Tr}([\omega \mathbb{1} - \underline{\underline{H}}_{\vec{k}} - \underline{\underline{\Sigma}}(\omega)]^{-1}). \tag{4.107}$$

By calculating the trace, we can visualize the band structure similar to our results in Chap. 3.

Equation (4.107) needs to be evaluated numerically for each $(\omega, \vec{k})$ point. We consider 600 equally distributed ω points in the interval $\omega = [-6\,\mathrm{eV}, 7\,\mathrm{eV}]$ and 700 $\vec{k}$ points (100 points per path between two high symmetry points). Due to the imaginary part of Σ, we obtain always finite values. Although, the imaginary part of $\Sigma(\omega)$ does not vanish in general in our calculations, it can be very small. In order to obtain numerically useful results, a small shift of ω into the imaginary plane is used: $\omega \to \omega + i\delta$. We use $\delta = 1 \times 10^{-2}$.

As a starting point, we show in Fig. 4.10 the resulting band structure without including any self-energy. Similar to Fig. 3.2 of Chap. 3, we obtain a metallic band structure.

In the next step, we include the self-energy. Since our DMFT calculations focus on the Mn $3d$ system, $\underline{\underline{\Sigma}}$ has only entries for the d orbitals. Furthermore, the entries are identical for the same spin orientation. That means we are using $\Sigma_1(\omega)$ for d orbitals at one Mn site and $\Sigma_2(\omega)$ for the d orbitals at the other Mn site. Note that $\underline{\underline{\Sigma}}$ has no off-diagonal matrix elements in our modeling.

By adding the self-energy to the orbital energies, we include correlation effects that are partly covered in the DFT calculations. This double counting problem could be solved ideally by substracting the double counting energy [92]. Unfortunately, this energy is not known in general. Therefore, we follow the same approach as

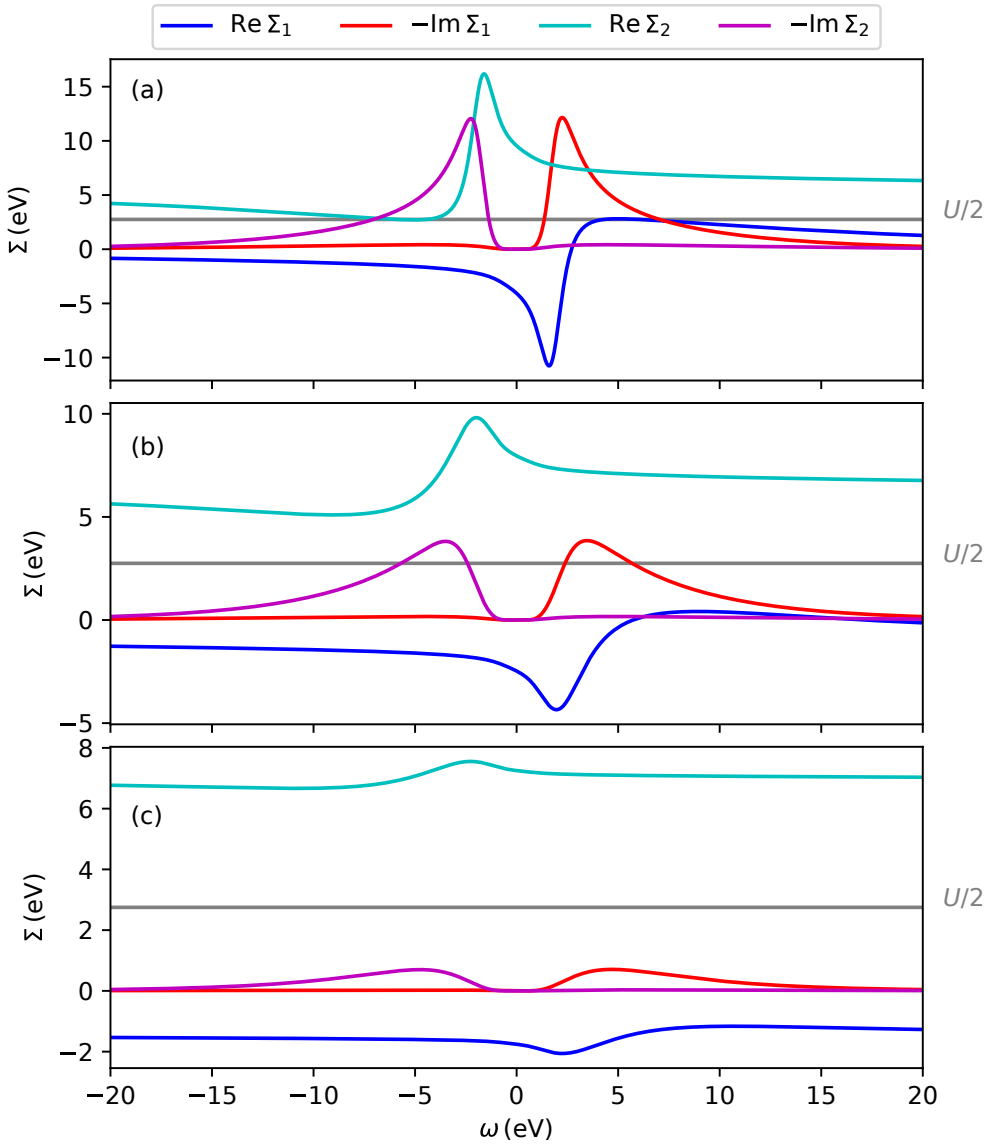

Figure 4.9: The real and imaginary parts of the self-energy for both spin channels for $\{U = 5.5\,\text{eV}, J_H = 1.6\,\text{eV}\}$ at (a) $T \approx 275\,\text{K}$, (b) $T \approx 205\,\text{K}$, and (c) $\approx 114\,\text{K}$. The imaginary part of the self-energy is mirrored comparing the different spin channels. The real part of the spin channels are related by a point symmetry around $(0, U/2)$. The curves become flatter by decreasing the temperature.

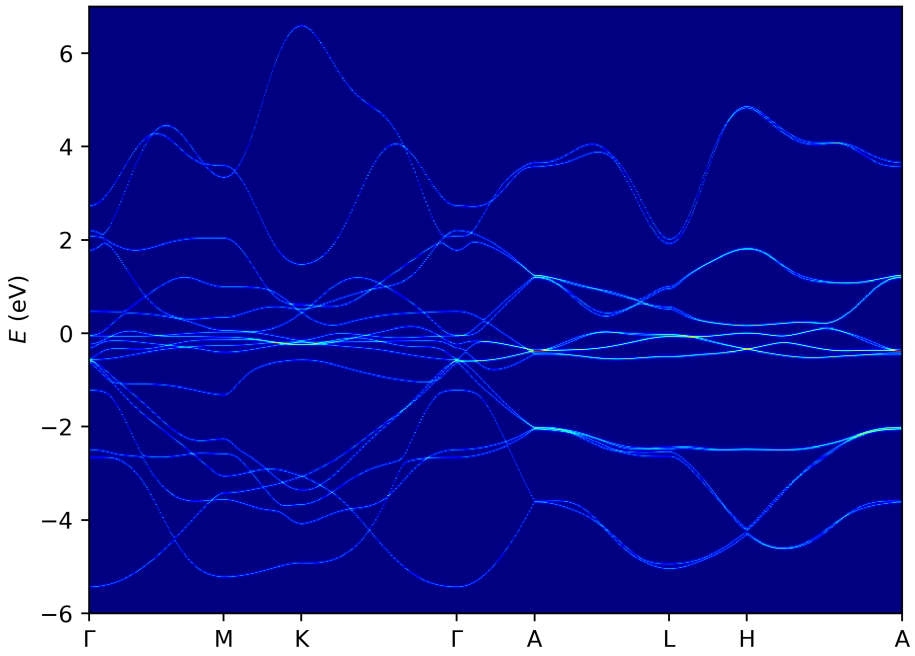

Figure 4.10: The band structure based on the tight-binding model of Chap. 3 and calculated via Eq. (4.107) without including any self-energy is metallic.

we used when we applied a frequency independent Hartree shift in Chap. 3. In this desciption, we split the d orbitals by shifting the orbital energies at one site down and at the other site up by the same absolute value. The absolute difference between the new orbital energies was given by U. Applying the same idea to the self-energies of the NRG calculation means that we consider the self-energies relative to $U/2$: $\tilde{\Sigma}(\omega) = \Sigma(\omega) - U/2$. In the limit of $T \to 0$, the Hartree shift has a similar effect as including the self-energy, and the absolute value of the splitting between the d bands is then approximately given by Δ_U (c. f. Fig. 4.9(c)).

We consider different parameter sets U and J_H. Reference [44] determined $U = 3\,\mathrm{eV}$ and $J_H = 0.5\,\mathrm{eV}$ using a tight-binding approach for a hypothetic cubic crystal structure, while Ref. [26] assumed larger values, from which we use $\{U = 5.5\,\mathrm{eV}, J_H = 1.6\,\mathrm{eV}\}$ and $\{U = 7\,\mathrm{eV}, J_H = 2\,\mathrm{eV}\}$. Except of U and J_H, we use the same parameters for the DMFT+NRG calculations as for the calculations presented above for $\{U = 5.5\,\mathrm{eV}, J_H = 1.6\,\mathrm{eV}\}$.

Figure 4.11 shows the renormalized band structure for $\{U = 5\,\text{eV}, J_H = 1.6\,\text{eV}\}$ at (a) $T \approx 494\,\text{K}$, a temperature well above the Néel temperature, and (b) $T \approx 275\,\text{K}$, a temperature belonging to partial polarization, and (c) $T \approx 114\,\text{K}$, a temperature well below the Néel temperature. Since different values for U and J_H are suggested in previous works, we aim to compare the effect of three different parameter sets on the band structure: Figure 4.12 shows the band structures for $\{U = 7\,\text{eV}, J_H = 2\,\text{eV}\}$ at $T \approx 555\,\text{K}$ and $T \approx 95\,\text{K}$, while Fig. 4.13 depicts it for $\{U = 3\,\text{eV}, J_H = 0.5\,\text{eV}\}$ at $T \approx 450\,\text{K}$ and $T \approx 103\,\text{K}$.

Above and below the Néel temperature, the band structures show band gaps. For very low temperatures $T \ll T_N$, the self-energy is almost constant, which leads us to the already discussed Hartree shift. But also in the magnetically unordered phase ($T > T_N$), the $1/\omega$ dependent self-energy induces a band gap.

A broadening is visible in the frequency interval, where the d bands lie, because of the imaginary part of the self-energy. Since the imaginary parts vanish for $T \to 0$, the band structure is sharper at lower temperatures. If the imaginary part of the self-energy is large, as for temperatures well above the Néel temperature, it is even possible that the bands are broadly smired out.

The exact value of the band gap will be calculated below, but a qualitative look at the band structure already reveales that the conduction band minimum lies at the K point, while the valence band maximum lies at the A point for low temperatures ($T < T_N$), as in found in Refs. [41] and [46], and at the Γ point for high temperatures ($T > T_N$).

Since Ref. [41] and [46] suggest that the upper d bands lie nearer to the Fermi energy than the lower d bands, an additional calculation with the real part of the self-energy shifted by 1 eV to lower energies is shown in Fig. 4.14. The band structure is similar to the structure without additional shift, except of the position of the d bands, which lie lower in energy as expected.

Since the valence band maxima and conduction band minima seem to be relatively sharp and not smired out by the imagninary part of the self-energy, we extract the band gap by finding the maxima of the spectral functions at each $\vec{k}$ point: $\max(A_{\vec{k}}(\omega))$. In the band gap, we do not find any maxima, such that we can determine the value of the band gap in this way. For $\{U = 5.5\,\text{eV}, J_H = 1.6\,\text{eV}\}$, we find $E_g(T \approx 494\,\text{K}) \approx 1.17\,\text{eV}$, $E_g(T \approx 275\,\text{K}) \approx 1.13\,\text{eV}$, $E_g(T \approx 114\,\text{K}) \approx 0.98\,\text{eV}$. The band gap becomes smaller when we consider smaller temperatures. The same effect applies for the other $\{U, J_H\}$ sets: $E_g(T \approx 450\,\text{K}) \approx 1.00\,\text{eV}$, $E_g(T \approx 103\,\text{K}) \approx 0.39\,\text{eV}$ for $\{U = 3\,\text{eV}, J_H = 0.5\,\text{eV}\}$ and $E_g(T \approx 555\,\text{K}) \approx 1.22\,\text{eV}$, $E_g(T \approx 95\,\text{K}) \approx 1.09\,\text{eV}$, for $\{U = 7\,\text{eV}, J_H = 2\,\text{eV}\}$. But we note that the change is less pronounced for larger $\Delta_U = U + 2J_H$. However, in each of the considered

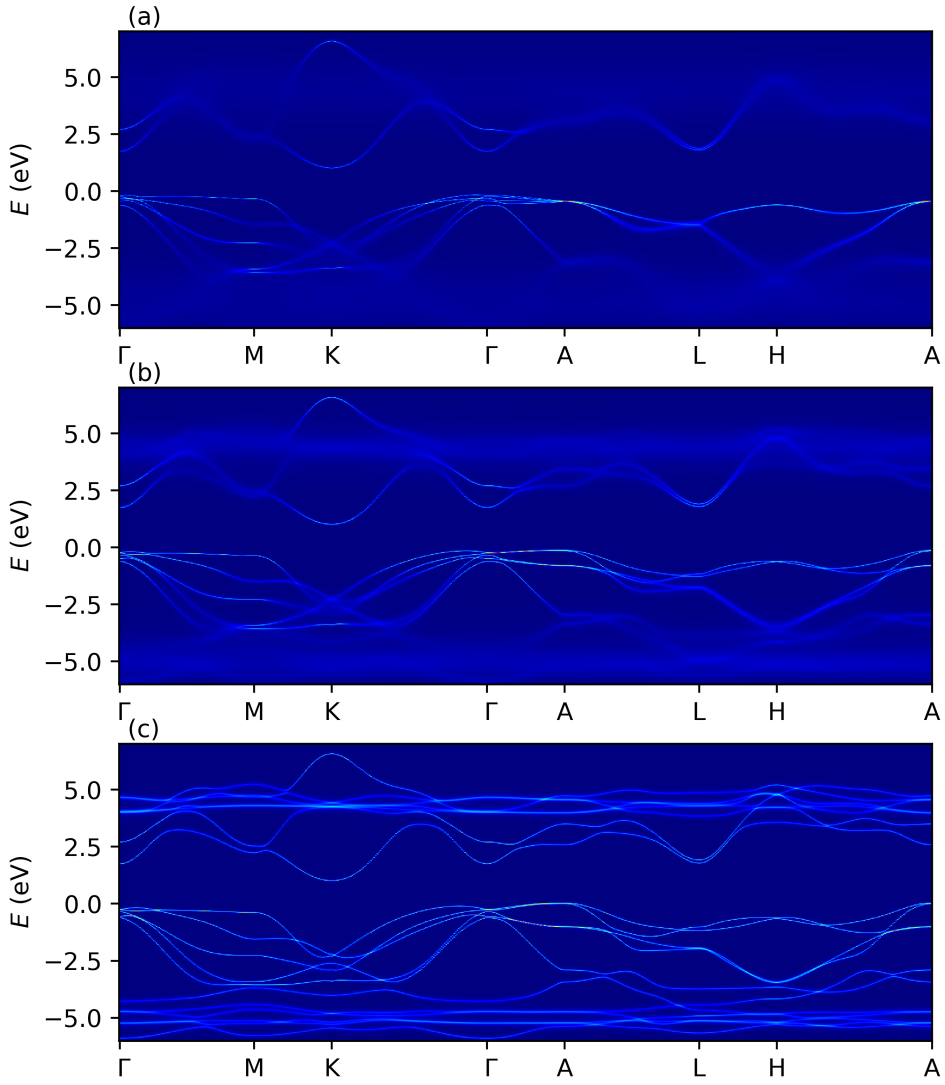

Figure 4.11: The band structure by including the self-energy for $\{U = 5.5\,\text{eV}, J_H = 1.6\,\text{eV}\}$ at (a) $T \approx 494\,\text{K}$, (b) $T \approx 275\,\text{K}$, and (c) $T \approx 114\,\text{K}$.

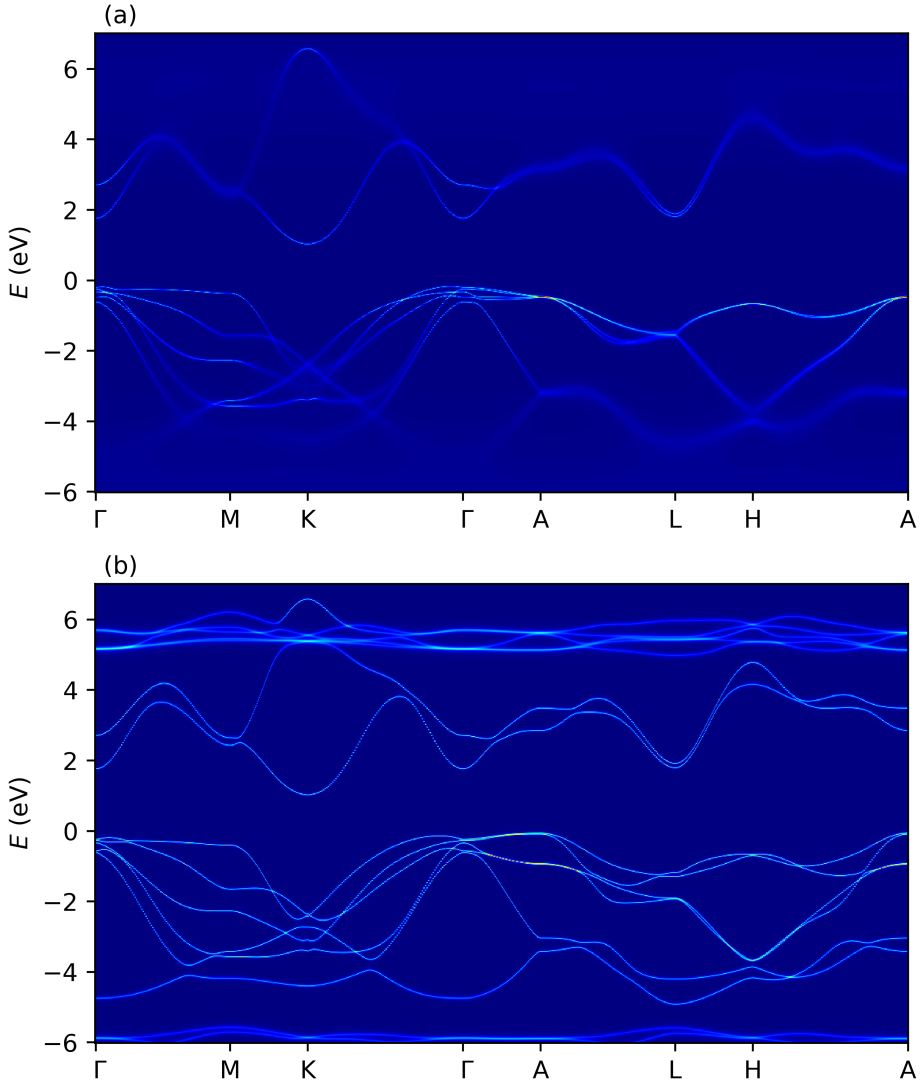

Figure 4.12: The band structure by including the self-energy for $\{U = 7\,\mathrm{eV}, J_H = 2\,\mathrm{eV}\}$ at (a) at (a) $T \approx 555\,\mathrm{K}$ and (b) $T \approx 95\,\mathrm{K}$.

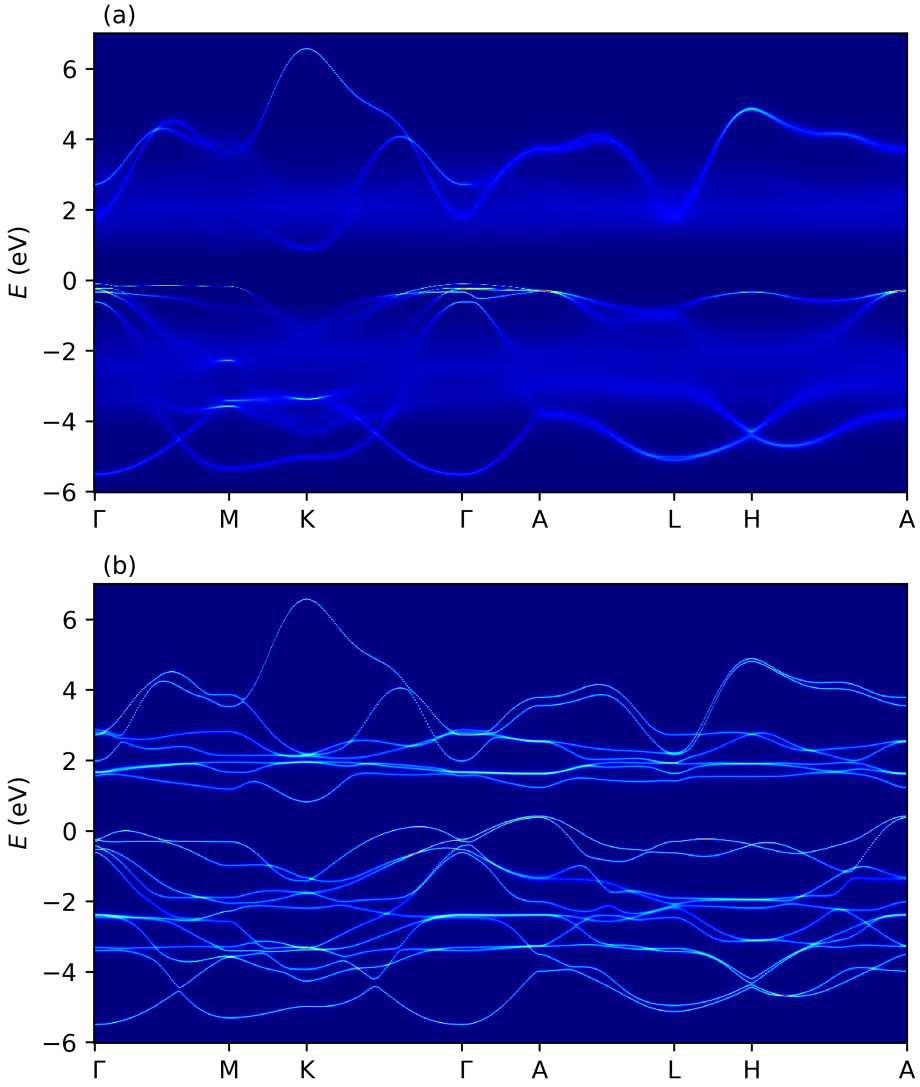

Figure 4.13: The band structure by including the self-energy for $\{U = 3\,\text{eV}, J_H = 0.5\,\text{eV}\}$ at (a) $T \approx 450\,\text{K}$ and (b) $T \approx 103\,\text{K}$.

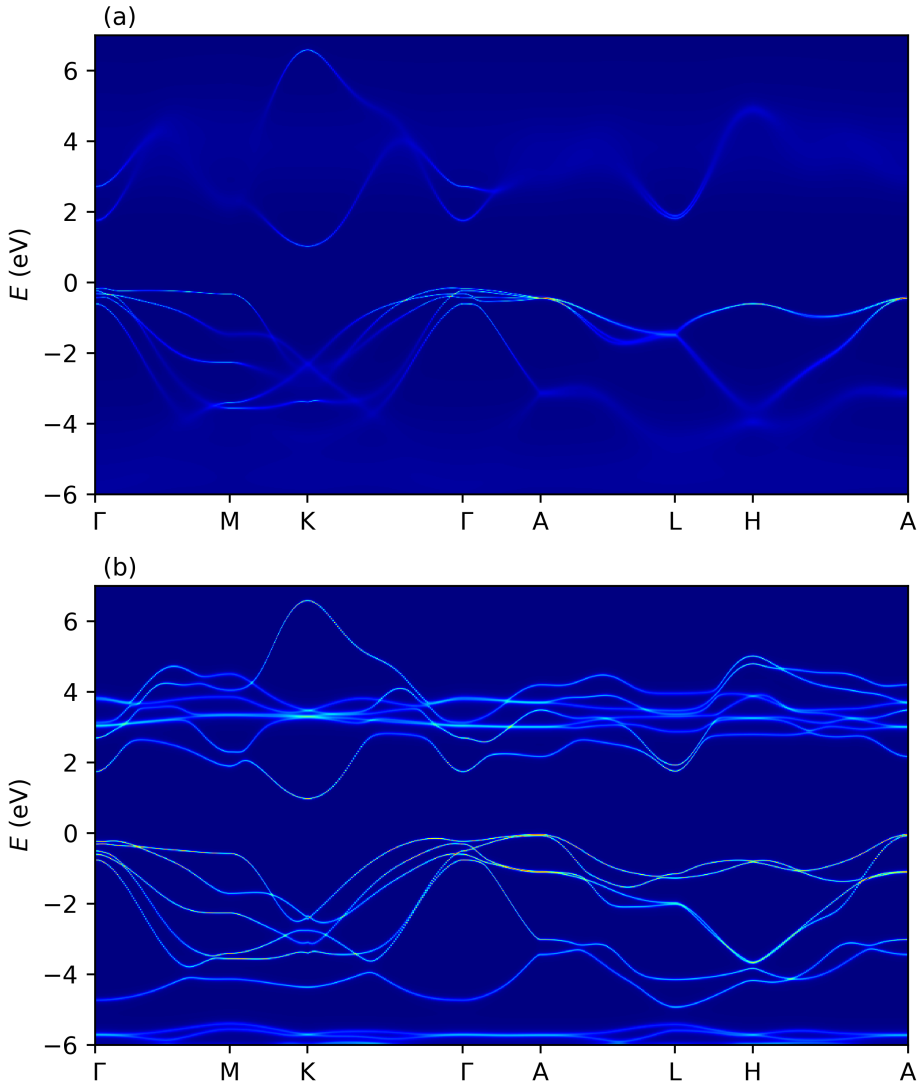

Figure 4.14: The band structure by including the self-energy for $\{U = 5.5\,\mathrm{eV}, J_H = 1.6\,\mathrm{eV}\}$ at (a) $T \approx 494\,\mathrm{K}$ and (b) $T \approx 114\,\mathrm{K}$ with an additional shift of 1 eV of the d bands to lower energies.

parameter sets, we see a decrease of the band gap for lower temperatures in contrast to the experimental results.

Furthermore, this approach – defining the band gap via the maxima of the sprectral functions – needs to be adapted if the bands are not sharp at the valence band maximum and at the conduction band minimum. Already for $\{U = 3\,\mathrm{eV}, J_H = 0.5\,\mathrm{eV}\}$, the band structure at the conduction band minimum looks slightly smired out, which would suggest that the band gap could be even smaller than calculated by only extracting the positions of the maxima of the sprectral functions.

Moreover, we only cosidered specific paths in the Brillouin zone to determine the band gap. Although we expect to find the valence band maximum and the conduction band minimum at high symmetry points, the calculation of the density of states to measure the band gap might be more accurate.

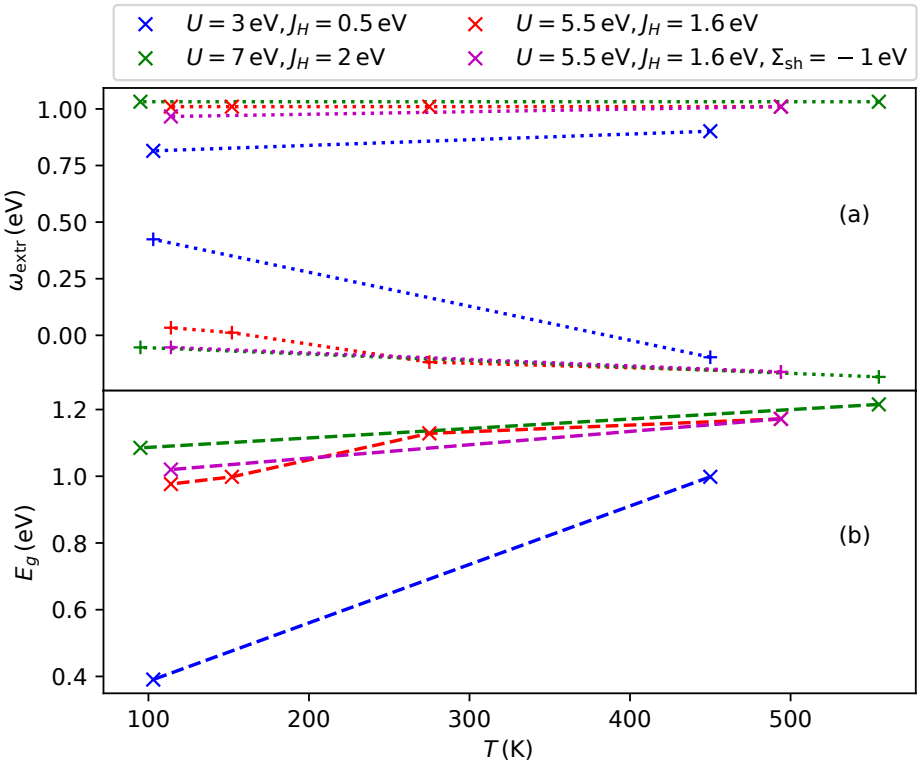

Figure 4.15: Overview of extracted band gaps: (a) the positions of the conduction band minima and maxima and (b) band gaps for different parameter sets.

Figure 4.15 summarizes the band gaps of all shown band structures. In addition, the data points for $\{U = 5.5\,\mathrm{eV}, J_H = 1.6\,\mathrm{eV}\}$ at $T \approx 152\,\mathrm{K}$ are added. Panel

(a) shows the position ω_{extr} of the extrema: the conduction band minima and the valence band maxima. The positions of the minima of the conduction band are very similar for large Δ_U without any shift, and they do not change their position. For $\{U = 3\,\text{eV}, J_H = 0.5\,\text{eV}\}$ and $\{U = 5.5\,\text{eV}, J_H = 1.6\,\text{eV}\}$ with an additional shift, their positions shift to lower energies. The positions for the valence band maxima shift for all considered parameter sets to higher energies. All in all, that leads to the decrease of the band gap as shown in Fig. 4.15(b).

The shift of the valence band minimum and the conduction band maximum can be explained by a highly simplified model. First, we focus only on the shift of the p band representing the valence band. Second, we follow the same idea by calculating the shift of the s band representing the conduction band.

Starting with the bands below the Fermi energy, let us consider one p band and one d band, which leads to the 2×2 Green's function

$$\underline{\underline{G}}(\vec{k}) = \begin{pmatrix} z - \epsilon^p_{\vec{k}} & -\epsilon^{pd}_{\vec{k}} \\ -\epsilon^{pd}_{\vec{k}} & z - \epsilon^d_{\vec{k}} - \Sigma \end{pmatrix} \tag{4.108}$$

with the dispersion $\epsilon^p_{\vec{k}}$ of the p band, the dispersion $\epsilon^d_{\vec{k}}$ of the d band, and the dispersion $\epsilon^{pd}_{\vec{k}}$ describing hopping between the bands. To obtain the bands, we determine

$$(\omega - \epsilon^p_{\vec{k}})(\omega - \epsilon^d_{\vec{k}} - \Sigma) - (\epsilon^{pd}_{\vec{k}})^2 = 0. \tag{4.109}$$

The analytic solution of the upper band

$$\omega_+ = \frac{\epsilon^p_{\vec{k}} + \epsilon^d_{\vec{k}} + \Sigma}{2} + \sqrt{\frac{(\epsilon^p_{\vec{k}} - \epsilon^d_{\vec{k}} - \Sigma)^2}{4} + (\epsilon^{pd}_{\vec{k}})^2}. \tag{4.110}$$

is relevant for the band gap. Although the imaginary part of the self-energy is relevant in general, we consider in this simplified model only a real Σ leading to sharp bands. For this simplified approach, we assume exemplarily $\epsilon^p_{\vec{k}} = -0.2\,\text{eV}, \epsilon^d_{\vec{k}} = 0\,\text{eV}, \epsilon^{pd}_{\vec{k}} = 0.5\,\text{eV}$ because the d band should be at the Fermi level without any correlations, the p band should be near, but below the the Fermi energy, and Fig. 3.1 suggests the order of magnitude for hopping between the orbitals, while the sign is not relevant since only the squared hopping parameter enters. Fig. 4.16(b) shows ω_+ in dependence of $-\Sigma$ since we know that Σ should be negative in this case. The solution ω_+ decreases for increasing $|\Sigma|$ and approaches a limit value for $|\Sigma| \to \infty$. Considering the self-energies obtained in the previous calculations below the Néel temperatures, which do not have a singularity at $\omega = 0$, we see that the absolute value of $\text{Re}\,\Sigma_1(\omega = 0)$ decreases with decreasing temperature. In consequence,

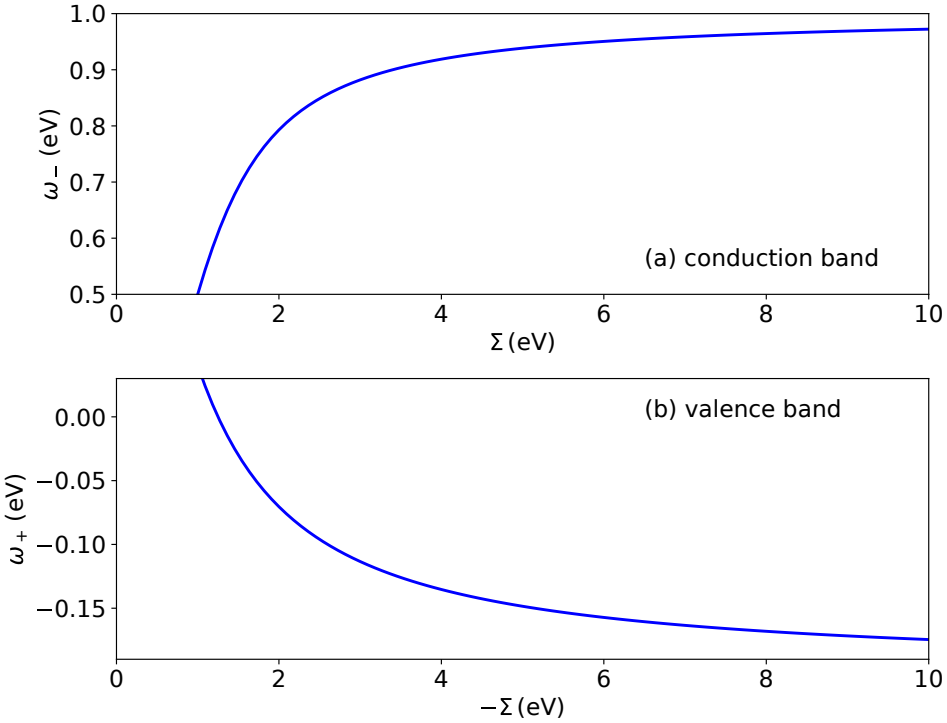

Figure 4.16: Conduction band (a) and valence band (b) in the simplified model. Parameters: (a) $\epsilon^s_{\vec{k}} = 1\,\text{eV}, \epsilon^d_{\vec{k}} = 0\,\text{eV}, \epsilon^{pd}_{\vec{k}} = 0.5\,\text{eV}$ and (b) $\epsilon^p_{\vec{k}} = -0.2\,\text{eV}, \epsilon^d_{\vec{k}} = 0\,\text{eV}, \epsilon^{pd}_{\vec{k}} = 0.5\,\text{eV}$.

this simplified model suggest that the valence band maximum should be at higher energies for lower temperatures as depicted in Fig. 4.15(a).

A very similar simplified model for one s and one d band representing the bands above the Fermi energy can be considered. Here the smaller solution

$$\omega_- = \frac{\epsilon^s_{\vec{k}} + \epsilon^d_{\vec{k}} + \Sigma}{2} - \sqrt{\frac{(\epsilon^s_{\vec{k}} - \epsilon^d_{\vec{k}} - \Sigma)^2}{4} + (\epsilon^{sd}_{\vec{k}})^2} \tag{4.111}$$

is relevant for the band gap. Exemplarily, we set $\epsilon^s_{\vec{k}} = 1\,\text{eV}, \epsilon^d_{\vec{k}} = 0\,\text{eV}, \epsilon^{sd}_{\vec{k}} = 0.5\,\text{eV}$. Here again the d band should lie at the Fermi energy if no correlations are included. The s band lies above the Fermi level; Fig. 4.15(a) shows that $\epsilon^s_{\vec{k}} = 1\,\text{eV}$ is suitable in our case. Concerning Fig. 3.1, the order of magnitude of $\epsilon^{sd}_{\vec{k}} = 0.5\,\text{eV}$ is realistic.

For the conduction band, the self-energy should be always positive. Figure 4.16(a) shows the curve development of ω_- in dependence of Σ. For larger Σ, ω_- is also larger. Again the previous calculations show that in the relevant ω interval, $\mathrm{Re}\,\Sigma_2(T_1) < \mathrm{Re}\,\Sigma_2(T_2)$ for $T_1 < T_2$, which means that the conduction band minimum lies at smaller energies for lower temperatures.

The simplified model suggests that the band gap becomes smaller at lower temperatures, if the absolute value of Σ increases with increasing temperature. Therefore, it explains the shift that we observe in the band structures. However, it depends only on the temperature dependent change of Σ. Future investigation should analyze if a more elaborate calculation of the self-energy can inverse the effect. Furthermore, the actual model is much more complex since it includes multiple orbitals and the full ω dependence of the self-energy.

4.4 Summary

We investigated a one-band Hubbard model with additional local spins and a Gaussian density of states to model a representative Mn $3d$ orbital. We calculated the local Green's function, the lattice Green's function, and the expectation values of the itinerant and the local spins.

The spin expectation values allowed us to distinguish between the paramagnetic phase at high temperatures and the magnetically ordered phase below the critical temperature. We were able to predict well the evolution of the magnetization curve of the analyzed systems, including the Néel temperature, with the results of a Heisenberg Hamiltonian in mean field approximation.

The Mott gap was measured using the integral criterion. Our observations demonstrated a larger band gap in the magnetic phase, consistent with the experimental measurements. We attributed this magnetic blue shift to the d bands becoming narrower. Moreover, while the Green's functions in the paramagnetic phase were identical for $\uparrow$ and $\downarrow$, with two bands exhibiting temperature-independent width, they were distinct in the magnetic phase. In the $T = 0$ and $U \to \infty$ limit, there should be only a single band situated either above or below the Fermi energy, depending on the spin. Moreover, the width of these bands reduces with decreasing temperature in the magnetically ordered phase. Unfortunately, the measurement of the band gap using the integral criterion depends on the chosen cut-off and the broadening. Additionally, the resulting magnetic blue shift of the Mott gap of our model is much larger than in experiments.

We were able to calculate a renormalized band structure by inserting the self-energy into a tight-binding model for hypothetic metallic α-MnTe obtained by DFT calculations. The band structure shows a band gap for temperatures below and above the Néel temperature. Its value (between $E_g \approx 0.39\,\mathrm{eV}$ and $E_g \approx 1.22\,\mathrm{eV}$ depending on the parameter set and the temperature) is in the order of the experimentally measured band gap, but generally smaller. Unfortunately, the band gap is smaller for lower temperatures in our modeling in contrast to the experimentally observed magnetic blue shift. For larger bare charge gaps Δ_U, the band gap is closer to the experimental value, and the temperature dependent shift is less prononced. The concrete value of the band gap depends highly on the parameters U and J_H. Furthermore, a global shift of the bands affects the band gap, even if one band still remains below and the other above the Fermi energy.

Chapter 5

Conclusion

Experiments showed that the band gap of α-MnTe, an antiferromagntic semiconductor, has a blue shift in the magnetic phase. In order to understand this phenomenon, we calculalted the magnetic and the electronic properties of α-MnTe using DMFT calculations to measure the band gap in the paramagnetic and magnetically ordered phase. Moreover, we referred to another experiment showing that laser pulses generates optical phonons in the material. We calculated magnon excitations assuming that the coherent lattice vibrations lead to a time-dependent Heisenberg coupling between the spins.

The magnetic system of α-MnTe comprises the magnetic moments of 5/2 localized at the Mn sites. We modeled this system by a Heisenberg Hamiltonian including three different kinds of nearest neighbors. We assume that laser pulses induce lattice vibrations, which modulate the Heisenberg couplings. Due to the geometry, we assume further that J_3, which couples Mn sites via a Te ion, is time-dependent. It oscillates around an equillibrium value with the optical phonon frequency. The finite duration is captured by an exponential damping, and the amplitude of the change is determined by the strength of driving. Using the linear spin wave theory and the Holstein-Primakoff representation as well as applying the Fourier and Bogliubov transformation, we obtained a set of differential equation that describes the magnon excitations induced by the time dependent coupling. We solved the $\vec{k}$ diagonal differential equations numerically and analyzed the results for a single $\vec{k}$ mode as well as for the complete sublattice magnetization, which is the sum over all $\vec{k}$ modes. We investigated the effect of parameters of driving. Increasing the strength of driving increases the amplitude of the sublattice magnetization. If the effect is linear or quadratic depends mainly on the question whether the driving is resonant. The driving frequency determines not only the frequency of the response but has also a significant effect on the amplitude. If the driving frequency matches the resonance condition $\omega_0 = 2\omega_{\vec{k}}$ for many modes, the amplitude will be large. The duration of the driving influences the decay of the sublattice magnetization. Their envelopes are similar. To capture relaxation, we included a phenomenological decay. As a result, the sublattice magnetization reaches the limit value 0 for large times.

We calculated the sublattice magnetization for realistic parameters. Since the damping of the driving and the relaxation rate act on different timescales, we can see both effects in the results seperately. For large driving strength, the magnon occupation becomes relevant. Unfortunately, it is not possible to detetermine the driving strength experimentally so far. A larger laser intensity should produce a larger driving, but the exact relation is unknown, which leaves us considering the rough estimation that the change of the Heisenberg coupling should be smaller than 10 %.
We investigated also the effect of assuming another Heisenberg coulping to be time-dependent. The resulting sublattice magnetization is qualitatively the same, only the value of the amplitude changes. But since a time dependent J_3 is most likely due to the geometry of the unit cell, we focussed on this case mostly.

Knowing the exact relation between the change of the Heisenberg coupling and the laser intensity could be a goal for future research. Furthermore, the model and the method can be adapted to other antiferromagntic systems easily, which enables the calculation of magnonic excitations in a lot of other materials.

By describing α-MnTe with a tight-binding model, we were able to understand the electronic structure. To calculate the hopping parameters, we used the Wanniernization of a band structure generated with the density functional theory. Starting with a given parameter set, we calculated the electronic dispersion and the corresponding density of states. The resulting band structure is metallic, unless we include a Hartree shift between the Mn $3d$ orbitals. When these bands split symmetrically by 5 eV, a band gap of approximately 0.6 eV occurs. By projecting on the atomic orbitals, we showed that the valence band has Te $5p$ character, while the conduction band can be described with Mn $3d$ and $4s$ contributions.

Our tight-binding modeling could be improved by a more sophisticated method of considering correlations. However, for including the self-energy in the tight-binding calculations, we need a model without these correlations. But we did not include the Mn $4p$ bands in the tight-binding model, although the density functional theory suggests that these bands could hybridize with the Mn $3d$ and $4s$ bands. Future research could build a model considering also the Mn $4p$ orbitals.

To capture magnetic and electronic degrees of freedom, we set up an effective one-band Hubbard-Kondo Hamiltonian, on which we performed DMFT calculations. In this model, we focus on the Mn $3d$ spins. We treated only one of the five spins itinerant and added a local spin of $S = 2$ at each Mn site. The spins induce an effective magnetic field on each other due to Heisenberg coupling. We included four types of nearest neighbors. All interaction strengths are antiferromagnetic. As impurity solver we used the NRG method. We calculated the Green's function as well as the spin expection values.

The sublattice magnetization, which is the sum of the expection values of the itinerant and local spins at one Mn site, follows approximately the solution of a Heisenberg Hamiltonian with $S = 5/2$.
We calculated half of the Mott gap in the paramagnetic as well as in the magnetically ordered phase and observed a magnetic blue shift. However, the absolute value of the shift is larger than in the experiment. The shift occurs due to a narrowing of the Green's functions for smaller temperatures.
Futhermore, we calculated the renormalized band structure by inserting the self-energy obtained in DMFT+NRG calculations into the multi-orbital tight-binding model. The band structures show band gaps for the magnetically ordered and unordered phase. The value of the band gap depends strongly on the chosen parameters U and J_H. It was between $E_g \approx 0.39\,\mathrm{eV}$ and $E_g \approx 1.22\,\mathrm{eV}$ for the parameters considered in this thesis. The values are smaller than the band gap measured in experiment. Moreover, the band gap becomes smaller for lower temperatures in contrast to the experimentally observed magnetic blue shift.

Altough we could explain our shift with a highly simplified model, future research should focus on the deeper understanding on these shifts, especially in a multi-orbital model. Next, it might be possible to adjust the modeling such that it can describe the actual magnetic blue shift.
Since a global shift of the d bands has an impact of the band gap, determining the double counting term to know the exact positions of the d bands would be useful.
Instead of using a Gaussian density of states, a more realistic density could be considered. An average density of states of the d orbitals resulting from the tight-binding model would be more accurate for example. Moreover, the Hubbard-Kondo model could be extended in order to include all five bands directly. However, our implementation of the numerical renormalization group method is designed to handle not more than three bands.
Moreover, another crystal structure of α-MnTe or a different antiferromagnetic semiconductor material with comparable electronic and magnetic structure could be treated similarly as we did for α-MnTe.
Our calculations focussed completely on the bulk material. Experimental methods, such as ARPES [93], can also detect surface effects. To describe these phenomena, our model could be modificated such that the dynamical mean field approach treats a layer. That means that the system would be only translational invariant in two directions.

Finally, we would like to come back to our starting point. Experiments found that there is a magnetic blue shift of the band gap in the magnetically ordered phase of α-MnTe. Another theoretical work [26] showed that in a Hubbard-Kondo model treated with real space dynamical density functional theory and exact diagonalization, this shift is a generic effect induced by the narrowing of the bands. We also found this blue

shift in the d system solved with a DMFT+NRG approach. The advantage of our procedure is that our Green's functions are continous, and, therefore, the narrowing can be seen very illustratively. Calculating the renormalized band structure by inserting the self-energy into the model leads to a band gap in the system. Our calculations suggest that the valence band maximum has Te p character, while the conduction band minimum has Mn s character. Although, the band gap is not equal to the magnetic shift of the Mott gap, the d bands affect the band gap. Unfortunately, we observed in our modeling a decrease of the band gap with decreasing temperature, which is the opposite effect than the experimentally measured magnetic blue shift. Future research should focus on the reasons for the difference to adjust the model such that it captures the experimental results.

Bibliography

[1] A. Kirilyuk, A. V. Kimel, and T. Rasing, *Ultrafast optical manipulation of magnetic order*, Rev. Mod. Phys. **82**, 2731 (2010).

[2] A. Kimel, A. Kirilyuk, P. Usachev, R. Pisarev, A. Balbashov, and T. Rasing, *Ultrafast non-thermal control of magnetization by instantaneous photomagnetic pulses*, Nature **435**, 655 (2005).

[3] E. Beaurepaire, J.-C. Merle, A. Daunois, and J.-Y. Bigot, *Ultrafast Spin Dynamics in Ferromagnetic Nickel*, Phys. Rev. Lett. **76**, 4250 (1996).

[4] A. Stupakiewicz, K. Szerenos, D. Afanasiev, A. Kirilyuk, and A. Kimel, *Ultrafast nonthermal photo-magnetic recording in a transparent medium*, Nature **542**, 71 (2017).

[5] B. Koopmans, G. Malinowski, F. Dalla Longa, D. Steiauf, M. Fähnle, T. Roth, M. Cinchetti, and M. Aeschlimann, *Explaining the paradoxical diversity of ultrafast laser-induced demagnetization*, Nature materials **9**, 259 (2010).

[6] M. Hofherr, S. Häuser, J. K. Dewhurst, P. Tengdin, S. Sakshath, H. T. Nembach, S. T. Weber, J. M. Shaw, T. J. Silva, H. C. Kapteyn, et al., *Ultrafast optically induced spin transfer in ferromagnetic alloys*, Science Advances **6**, `10.1126/sciadv.aay8717` (2020).

[7] S. A. Wolf, D. D. Awschalom, R. A. Buhrman, J. M. Daughton, S. von Molnár, M. L. Roukes, A. Y. Chtchelkanova, and D. M. Treger, *Spintronics: A Spin-Based Electronics Vision for the Future*, Science **294**, 1488 (2001).

[8] I. Žuti ć, J. Fabian, and S. Das Sarma, *Spintronics: Fundamentals and applications*, Rev. Mod. Phys. **76**, 323 (2004).

[9] A. Hirohata, K. Yamada, Y. Nakatani, I.-L. Prejbeanu, B. Diény, P. Pirro, and B. Hillebrands, *Review on spintronics: Principles and device applications*, Journal of Magnetism and Magnetic Materials **509**, 166711 (2020).

[10] S. Bhatti, R. Sbiaa, A. Hirohata, H. Ohno, S. Fukami, and S. Piramanayagam, *Spintronics based random access memory: a review*, Materials Today **20**, 530 (2017).

[11] Z. Guo, J. Yin, Y. Bai, D. Zhu, K. Shi, G. Wang, K. Cao, and W. Zhao, *Spintronics for Energy- Efficient Computing: An Overview and Outlook*, Proceedings of the IEEE **109**, 1398 (2021).

[12] N. Jones, *How to stop data centres from gobbling up the world's electricity*, Nature **561**, 163 (2018).

[13] D. Afanasiev, B. A. Ivanov, A. Kirilyuk, T. Rasing, R. V. Pisarev, and A. V. Kimel, *Control of the Ultrafast Photoinduced Magnetization across the Morin Transition in* $DyFeO_3$, Phys. Rev. Lett. **116**, 097401 (2016).

[14] S. L. Johnson, R. A. de Souza, U. Staub, P. Beaud, E. Möhr-Vorobeva, G. Ingold, A. Caviezel, V. Scagnoli, W. F. Schlotter, J. J. Turner, et al., *Femtosecond Dynamics of the Collinear-to-Spiral Antiferromagnetic Phase Transition in CuO*, Phys. Rev. Lett. **108**, 037203 (2012).

[15] D. Bossini, K. Konishi, S. Toyoda, T. Arima, J. Yumoto, and M. Kuwata-Gonokami, *Femtosecond activation of magnetoelectricity*, Nat. Phys. **14**, 370 (2018).

[16] D. Bossini, S. Dal Conte, Y. Hashimoto, A. Secchi, R. Pisarev, T. Rasing, G. Cerullo, and A. Kimel, *Macrospin dynamics in antiferromagnets triggered by sub-20 femtosecond injection of nanomagnons*, Nature communications **7**, 1 (2016).

[17] D. Bossini, A. M. Kalashnikova, R. V. Pisarev, T. Rasing, and A. V. Kimel, *Controlling coherent and incoherent spin dynamics by steering the photoinduced energy flow*, Phys. Rev. B **89**, 060405 (2014).

[18] T. Satoh, R. Iida, T. Higuchi, M. Fiebig, and T. Shimura, *Writing and reading of an arbitrary optical polarization state in an antiferromagnet*, Nature Photonics **9**, 25 (2015).

[19] M. Först, C. Manzoni, S. Kaiser, Y. Tomioka, Y. Tokura, R. Merlin, and A. Cavalleri, *Nonlinear phononics as an ultrafast route to lattice control*, Nature Physics **7**, 854 (2011).

[20] T. F. Nova, A. Cartella, A. Cantaluppi, M. Först, D. Bossini, R. V. Mikhaylovskiy, A. V. Kimel, R. Merlin, and A. Cavalleri, *An effective magnetic field from optically driven phonons*, Nature Physics **13**, 132 (2017).

[21] Y. Hashimoto, D. Bossini, T. H. Johansen, E. Saitoh, A. Kirilyuk, and T. Rasing, *Frequency and wavenumber selective excitation of spin waves through coherent energy transfer from elastic waves*, Phys. Rev. B **97**, 140404 (2018).

[22] J. Zhang, Q. Lian, Z. Pan, W. Bai, J. Yang, Y. Zhang, X. Tang, and J. Chu, *Spin-phonon coupling and two-magnons scattering behaviors in hexagonal NiAs-type antiferromagnetic MnTe epitaxial films*, Journal of Raman Spectroscopy **51**, 1383 (2020).

[23] D. Bossini, S. Dal Conte, M. Terschanski, G. Springholz, A. Bonanni, K. Deltenre, F. Anders, G. S. Uhrig, G. Cerullo, and M. Cinchetti, *Femtosecond phononic coupling to both spins and charges in a room-temperature antiferromagnetic semiconductor*, Phys. Rev. B **104**, 224424 (2021).

[24] D. Bossini, M. Terschanski, F. Mertens, G. Springholz, A. Bonanni, G. S. Uhrig, and M. Cinchetti, *Exchange-mediated magnetic blue-shift of the band-gap energy in the antiferromagnetic semiconductor MnTe*, New Journal of Physics **22**, 083029 (2020).

[25] Y. Varshni, *Temperature dependence of the energy gap in semiconductors*, Physica **34**, 149 (1967).

[26] M. Hafez-Torbati, D. Bossini, F. B. Anders, and G. S. Uhrig, *Magnetic blue shift of Mott gaps enhanced by double exchange*, Phys. Rev. Res. **3**, 043232 (2021).

[27] M. Hafez-Torbati, F. B. Anders, and G. S. Uhrig, *Simplified approach to the magnetic blue shift of Mott gaps*, Phys. Rev. B **106**, 205117 (2022).

[28] S. R. Mobasser and T. R. Hart, *Raman scattering from phonons and magnons in magnetic semiconductor, MnTe*, Proc. SPIE **0524**, 137 (1985).

[29] R. Minikayev, E. Dynowska, B. Witkowska, A. M. T. Bell, and W. Szuszkiewicz, *Unit-cell dimensions of -MnTe in the 295 K – 1200 K temperature range*, X-Ray Spectrometry **44**, 394 (2015).

[30] S. S. A. Noor, *Magnetic phase transition in Mn0.5Te0.5−xSbx*, Journal of Applied Physics **61**, 3549 (1987).

[31] *Crystallography Open Database, entry 1537607*, `https://www.crystallography.net/cod/1537607.html`.

[32] K. Momma and F. Izumi, *VESTA3 for three-dimensional visualization of crystal, volumetric and morphology data*, Journal of Applied Crystallography **44**, 1272 (2011).

[33] D. Kriegner, K. Výborný, K. Olejník, H. Reichlová, V. Novák, X. Marti, J. Gazquez, V. Saidl, P. Němec, V. V. Volobuev, et al., *Multiple-stable anisotropic magnetoresistance memory in antiferromagnetic MnTe*, Nat Commun **7**, 11623 (2016).

[34] T. Komatsubara, M. Murakami, and E. Hirahara, *Magnetic Properties of Manganese Telluride Single Crystals*, Journal of the Physical Society of Japan **18**, 356 (1963).

[35] N. Kunitomi, Y. Hamaguchi, and S. Anzai, *Neutron diffraction study on manganese telluride*, J. Phys. France **25**, 568 (1964).

[36] K. Deltenre, D. Bossini, F. B. Anders, and G. S. Uhrig, *Lattice-driven femtosecond magnon dynamics in* $\alpha-$MnTe, Phys. Rev. B **104**, 184419 (2021).

[37] T. Holstein and H. Primakoff, *Field Dependence of the Intrinsic Domain Magnetization of a Ferromagnet*, Phys. Rev. **58**, 1098 (1940).

[38] M. Takahashi, *Modified spin-wave theory of a square-lattice antiferromagnet*, Phys. Rev. B **40**, 2494 (1989).

[39] C. J. Hamer, Z. Weihong, and P. Arndt, *Third-order spin-wave theory for the Heisenberg antiferromagnet*, Phys. Rev. B **46**, 6276 (1992).

[40] W. Szuszkiewicz, E. Dynowska, B. Witkowska, and B. Hennion, *Spin-wave measurements on hexagonal* MnTe *of* NiAs*-type structure by inelastic neutron scattering*, Phys. Rev. B **73**, 104403 (2006).

[41] S. Mu, R. P. Hermann, S. Gorsse, H. Zhao, M. E. Manley, R. S. Fishman, and L. Lindsay, *Phonons, magnons, and lattice thermal transport in antiferromagnetic semiconductor MnTe*, Phys. Rev. Materials **3**, 025403 (2019).

[42] T. Hanisch, B. Kleine, A. Ritzl, and E. Müller-Hartmann, *Ferromagnetism in the Hubbard model: instability of the Nagaoka state on the triangular, honeycomb and kagome lattices*, Annalen der Physik **507**, 303 (1995).

[43] M. Podgorny and J. Oleszkiewicz, *Electronic structure of antiferromagnetic MnTe*, Journal of Physics C: Solid State Physics **16**, 2547 (1983).

[44] J. Masek, B. Velicky, and V. Janis, *A tight binding study of the electronic structure of MnTe*, Journal of Physics C: Solid State Physics **20**, 59 (1987).

[45] L. M. Sandratskii, R. F. Egorov, and A. A. Berdyshev, *Energy Band Structure and Electronic Properties of NiAs Type Compounds. I. Ferromagnetic Manganese Arsenide*, physica status solidi (b) **103**, 511 (1981).

[46] T. Linneweber, *Bandstrukturrechnung zu MnTe (internal report)*, 2018.

[47] G. Czycholl, *Theoretische Festkörperphysik* (Springer Berlin, Heidelberg, 2008).

[48] R. Gross and A. Marx, *Festkörperphysik* (De Gruyter, Berlin, Boston, 2018).

[49] H. J. Monkhorst and J. D. Pack, *Special points for Brillouin-zone integrations*, Phys. Rev. B **13**, 5188 (1976).

[50] Nobel Foundation, *All Nobel Prizes in Chemistry*, `https://www.nobelprize.org/prizes/lists/all-nobel-prizes-in-chemistry/` (visited on 10/19/2023).

[51] X. Blase, *Introduction to Density Functional Theory*, in *Many-Body Methods for Real Materials*, edited by E. Pavarini, E. Koch, and S. Zhang (Forschungszentrum Jülich, 2019), pp. 1.1–1.25.

[52] P. Hohenberg and W. Kohn, *Inhomogeneous Electron Gas*, Phys. Rev. **136**, B864 (1964).

[53] W. Kohn and L. J. Sham, *Self-Consistent Equations Including Exchange and Correlation Effects*, Phys. Rev. **140**, A1133 (1965).

[54] J. P. Perdew, J. A. Chevary, S. H. Vosko, K. A. Jackson, M. R. Pederson, D. J. Singh, and C. Fiolhais, *Atoms, molecules, solids, and surfaces: Applications of the generalized gradient approximation for exchange and correlation*, Phys. Rev. B **46**, 6671 (1992).

[55] *The FLEUR project*, `https://www.flapw.de/`.

[56] *VASP*, `https://vasp.at/`.

[57] P. Giannozzi, S. Baroni, N. Bonini, M. Calandra, R. Car, C. Cavazzoni, D. Ceresoli, G. L. Chiarotti, M. Cococcioni, I. Dabo, et al., *QUANTUM ESPRESSO: a modular and open-source software project for quantum simulations of materials*, Journal of Physics: Condensed Matter **21**, 395502 (2009).

[58] P. Giannozzi, O. Andreussi, T. Brumme, O. Bunau, M. B. Nardelli, M. Calandra, R. Car, C. Cavazzoni, D. Ceresoli, M. Cococcioni, et al., *Advanced capabilities for materials modelling with Quantum ESPRESSO*, Journal of Physics: Condensed Matter **29**, 465901 (2017).

[59] K. F. Garrity, J. W. Bennett, K. M. Rabe, and D. Vanderbilt, *GBRV pseudopotential library,* `https://www.physics.rutgers.edu/gbrv/` (visited on 12/01/2023).

[60] K. F. Garrity, J. W. Bennett, K. M. Rabe, and D. Vanderbilt, *Pseudopotentials for high-throughput DFT calculations*, Computational Materials Science **81**, 446 (2014).

[61] J. P. Perdew, A. Ruzsinszky, G. I. Csonka, O. A. Vydrov, G. E. Scuseria, L. A. Constantin, X. Zhou, and K. Burke, *Restoring the Density-Gradient Expansion for Exchange in Solids and Surfaces*, Phys. Rev. Lett. **100**, 136406 (2008).

[62] E. Engel, J. A. Chevary, L. D. Macdonald, and S. H. Vosko, *Asymptotic properties of the exchange energy density and the exchange potential of finite systems: relevance for generalized gradient approximations*, Z Phys D Atoms, Molecules and Clusters **23**, 7 (1992).

[63] L. Talirz, S. Kumbhar, E. Passaro, A. V. Yakutovich, V. Granata, F. Gargiulo, M. Borelli, M. Uhrin, S. P. Huber, S. Zoupanos, et al., *Materials Cloud, a platform for open computational science*, Scientific Data **7**, 299 (2020).

[64] *Quantum ESPRESSO input generator and structure visualizer*, `https://www.materialscloud.org/work/tools/qeinputgenerator` (visited on 12/13/2023).

[65] G. Prandini, A. Marrazzo, I. E. Castelli, N. Mounet, and N. Marzari, *Precision and efficiency in solid-state pseudopotential calculations*, npj Computational Materials **4**, 72 (2018).

[66] *SeeK-path: the k-path finder and visualizer*, `https://www.materialscloud.org/work/tools/seekpath` (visited on 12/13/2023).

[67] Y. Hinuma, G. Pizzi, Y. Kumagai, F. Oba, and I. Tanaka, *Band structure diagram paths based on crystallography*, Computational Materials Science **128**, 140 (2017).

[68] A. Togo and I. Tanaka, *`Spglib`: a software library for crystal symmetry search*, 2018.

[69] S. P. Ong, W. D. Richards, A. Jain, G. Hautier, M. Kocher, S. Cholia, D. Gunter, V. L. Chevrier, K. A. Persson, and G. Ceder, *Python Materials Genomics (pymatgen): A robust, open-source python library for materials analysis*, Computational Materials Science **68**, 314 (2013).

[70] G. Pizzi, V. Vitale, R. Arita, S. Blügel, F. Freimuth, G. Géranton, M. Gibertini, D. Gresch, C. Johnson, T. Koretsune, et al., *Wannier90 as a community code: new features and applications*, Journal of Physics: Condensed Matter **32**, 165902 (2020).

[71] N. Marzari, A. A. Mostofi, J. R. Yates, I. Souza, and D. Vanderbilt, *Maximally localized Wannier functions: Theory and applications*, Rev. Mod. Phys. **84**, 1419 (2012).

[72] G. H. Wannier, *The Structure of Electronic Excitation Levels in Insulating Crystals*, Phys. Rev. **52**, 191 (1937).

[73] C. Sanderson and R. Curtin, *Armadillo: a template-based C++ library for linear algebra*, Journal of Open Source Software **1**, 26 (2016).

[74] C. Sanderson and R. R. Curtin, *A User-Friendly Hybrid Sparse Matrix Class in C++*, Lecture Notes in Computer Science (LNCS) **10931**, 422 (2018).

[75] A. Georges, G. Kotliar, W. Krauth, and M. J. Rozenberg, *Dynamical mean-field theory of strongly correlated fermion systems and the limit of infinite dimensions*, Rev. Mod. Phys. **68**, 13 (1996).

[76] E. Pavarini, *Dynamical Mean-Field Theory for Materials*, in *Many-Body Methods for Real Materials*, edited by E. Pavarini, E. Koch, and S. Zhang (Forschungszentrum Jülich, 2019), pp. 11.1–11.44.

[77] P. Weiss, *L'hypothèse du champ moléculaire et la propriété ferromagnétique*, J. Phys. Theor. Appl., **907,** 661 (1907).

[78] E. Khatami, C. R. Lee, Z. J. Bai, R. T. Scalettar, and M. Jarrell, *Cluster solver for dynamical mean-field theory with linear scaling in inverse temperature*, Phys. Rev. E **81**, 056703 (2010).

[79] D. Rost, F. Assaad, and N. Blümer, *Quasi-continuous-time impurity solver for the dynamical mean-field theory with linear scaling in the inverse temperature*, Phys. Rev. E **87**, 053305 (2013).

[80] Y. Lu and M. W. Haverkort, *Exact diagonalization as an impurity solver in dynamical mean field theory*, Eur. Phys. J. Spec. Top. **226**, 2549 (2017).

[81] K. G. Wilson, *The renormalization group: Critical phenomena and the Kondo problem*, Rev. Mod. Phys. **47**, 773 (1975).

[82] R. Zitzler, *Magnetic Properties of the One-Band Hubbard Model*, PhD thesis (Mathematisch-Naturwissenschaftlichen Fakultät der Universität Augsburg, 2004).

[83] Nobel Foundation, *All Nobel Prizes in Physics*, `https://www.nobelprize.org/prizes/lists/all-nobel-prizes-in-physics/` (visited on 10/29/2023).

[84] R. Bulla, T. A. Costi, and T. Pruschke, *Numerical renormalization group method for quantum impurity systems*, Rev. Mod. Phys. **80**, 395 (2008).

[85] R. Bulla, T. Pruschke, and A. C. Hewson, *Anderson impurity in pseudo-gap Fermi systems*, Journal of Physics: Condensed Matter **9**, 10463 (1997).

[86] H. O. Frota and L. N. Oliveira, *Photoemission spectroscopy for the spin-degenerate Anderson model*, Phys. Rev. B **33**, 7871 (1986).

[87] M. Yoshida, M. A. Whitaker, and L. N. Oliveira, *Renormalization-group calculation of excitation properties for impurity models*, Phys. Rev. B **41**, 9403 (1990).

[88] W. C. Oliveira and L. N. Oliveira, *Generalized numerical renormalization-group method to calculate the thermodynamical properties of impurities in metals*, Phys. Rev. B **49**, 11986 (1994).

[89] V. L. Campo and L. N. Oliveira, *Alternative discretization in the numerical renormalization-group method*, Phys. Rev. B **72**, 104432 (2005).

[90] R. Bulla, A. C. Hewson, and T. Pruschke, *Numerical renormalization group calculations for the self-energy of the impurity Anderson model*, Journal of Physics: Condensed Matter **10**, 8365 (1998).

[91] W. Metzner and D. Vollhardt, *Correlated Lattice Fermions in $d = \infty$ Dimensions*, Phys. Rev. Lett. **62**, 324 (1989).

[92] M. Karolak, G. Ulm, T. Wehling, V. Mazurenko, A. Poteryaev, and A. Lichtenstein, *Double counting in LDA+DMFT—The example of NiO*, Journal of Electron Spectroscopy and Related Phenomena **181**, Proceedings of International Workshop on Strong Correlations and Angle-Resolved Photoemission Spectroscopy 2009, 11 (2010).

[93] J. A. Sobota, Y. He, and Z.-X. Shen, *Angle-resolved photoemission studies of quantum materials*, Rev. Mod. Phys. **93**, 025006 (2021).

Acknowledgements

I thank Prof. Dr. Frithjof B. Anders for being the supervisor and reviewer of my thesis. He offered me a very interesting topic, let me use his NRG code, and was always willing to answer my questions. I am grateful for his support.

I appreciate that Prof. Dr. Götz S. Uhrig agreed to be the second reviewer, and I thank him for his support and collaboration in the magnon project.

Moreover, I am grateful for the discussions with Dr. Davide Bossini about the experiments and the way how to connect them with theoretical approaches.

I also thank Dr. Carsten Nase for his very helpful IT support.

Furthermore, I am very happy about the numerous discussions with group members. Their ideas and advices helped me a lot to complete my work. I appreciate very much that Dr. Fabian Eickhoff helped me to use the NRG method, and I would like to thank Hendrik Trojan and Frederik Vonhoff for their advice concerning the DFT method. I thank Dr. Andriana Tsikritea, Dr. Fabian Eickhoff, and Frederik Vonhoff for proof-reading.

Finally, I thank my family and friends a lot for their support. I am especially grateful that Christian Benedict Smit helped me with coding problems and accompanied me during this time.